

Diss. ETH No. 14965

# **Design and Applications of New MOCVD Precursors for Nitrogen-Containing Zirconium-Based Thin Films**

A dissertation submitted to the

SWISS FEDERAL INSTITUTE OF TECHNOLOGY

For the degree of

DOCTOR OF NATURAL SCIENCES

Presented by

PIER LUIGI FRANCESCHINI

Degree in Industrial Chemistry, University of Rome "La Sapienza"

Born on November 25, 1972

Citizen of Italy

Accepted on the recommendation of

Prof. Dr. N. D. Spencer, examiner

Prof. Dr. H. Berke, co-examiner

Dr. Marcus Morstein, co-examiner

Dr. Stefan Zürcher, co-examiner

Zürich 2002



*This work is dedicated  
to the memory of my friend Patrizia Altamura*

## Acknowledgements

I am in debt to many people who contributed in several ways to this work, and supported me with their friendship. In particular I wish to express my gratitude to

Prof. Dr. H. Berke and Prof. N. D. Spencer for giving me the opportunity to work in their research groups and for supporting during these years.

Dr. M. Morstein, the mind behind this project, for introducing me in this topic, teaching me many things, for his confidence and all the stimulating discussions

Dr. Stefan Zürcher for his unique support in every aspects of the experimental work, from the synthetic part to the CVD, for all the stimulating ideas, all the deep discussions and of course for the time he spent in reviewing this manuscript

Dr. Helmut Schmalle for all the important X-ray diffraction work

Armin Portmann for the SEM measurements

Marc Dusseiller for dedicating a lot of his time for the SEM measurements

All the technical and administrative people at ACI and LSST: Bea, Martina, Brigitta, Barbara, Irene, Heinz, Hans-Peter.

Johan Cugny, who helped me a lot in the lab, but especially was a great fellow during the exploration of the dark sides of Zürich's night life.

Maša, of course

All my family for their constant support

## Abstract

The aim of this work is the development of novel precursors for the deposition of technologically interesting zirconium-based, nitrogen-containing thin films by Metal Organic Chemical Vapor Deposition (MOCVD).

Starting from  $Zr(NR_2)_4$  and (2Z, 4E)-N-methyl-4-(methylimino)pent-2-en-2-amine (abbreviated with HMeNacNac), compounds of the type  $Zr(MeNacNac)_2(NR_2)_2$  (R = Me (**1**), Et (**2**)) were obtained by amide metathesis. Employing the Schiff Base (3Z)-4-(methylamino)pent-3-en-2-one (HMeNacac), it was also possible to prepare the six-coordinate compound  $Zr(MeNacac)_2(NEt_2)_2$  (**3**). Changing the reaction stoichiometry and the steric bulk of the reactants five-coordinate compounds with the general formula  $Zr(\beta\text{-diketiminato})(NRR'_2)_3$  (**4**, **5**) were obtained. When hydrogen-substituted  $\beta$ -diketimines were used, homoleptic tetrakis( $\beta$ -diketiminato)- and tetrakis( $\beta$ -ketoiminato)zirconium compounds **6** and **7** were obtained. All complexes were fully characterized by NMR spectroscopy, mass spectrometry, elemental analysis and when possible, X-ray single crystal structures were obtained.

Another class of bidentate N-donor ligands employed were the guanidates. As in the former case, compounds of the general formula  $Zr(\text{guanidinato})_2(NR_2)_2$  (**12**, **13**) with coordination number six were synthesized and isolated, as well as one five-coordinate compound of the type  $Zr(\text{guanidinato})(NR_2)_3$  (**14**).

The thermal properties and volatility of these compounds were investigated by thermal analysis (TG and DSC). The most volatile compounds are the six-coordinated  $\beta$ -diketiminato-based compounds **1** and **2**. Eight-coordinate compounds are more thermally stable but less volatile. Guanidato-based compounds with coordination number six are less volatile compared to compounds **1** and **2**. All five-coordinate diketiminato- and guanidato-based complexes are non-volatile.

The vapor pressure of compound **1** was measured in the temperature range between 120 and 140 °C, and the enthalpy of sublimation was found to be  $\Delta H_{\text{subl}} = 90.9 \pm 1.2$  KJ/mol.

Complex **1** was tested in CVD experiments using a vertical cold wall reactor. The substrate temperature was varied between 450 and 650 °C. The surface composition of the films was characterized by XPS. Thin films of Zr(C,N) were obtained, with compositions varying with the temperature. A surface oxide/oxynitride layer was formed on top of these films as a result of oxidation upon exposure to the air.

## Riassunto

L'obiettivo di questo lavoro è lo sviluppo di nuovi precursori per la deposizione, tramite *Metal Organic Chemical Vapor Deposition* (MOCVD), di film a base di carbonitruro di zirconio, importanti dal punto di vista tecnologico. Partendo dai composti  $Zr(NR_2)_4$  e (2Z, 4E)-N-metil-4-(metilimmino)pent-2-en-2-ammina (abbreviato con HMeNacNac), attraverso una reazione di metatesi di ammidi sono stati ottenuti composti del tipo  $Zr(MeNacNac)_2(NR_2)_2$  (R = Me (**1**), Et (**2**)). Utilizzando la base di Schiff (3Z)-4-(metilammino)pent-3-en-2-one (HMeNacac), è stato possibile preparare il composto esacoordinato  $Zr(MeNacac)_2(NEt_2)_2$  (**3**). Cambiando la stechiometria della reazione e l'ingombro sterico dei reagenti, sono stati ottenuti composti pentacoordinati aventi la formula generale  $Zr(\beta\text{-dichetiminato})(NRR'_2)_3$  (**4**, **5**). Utilizzando  $\beta$ -dichetimmine sostituite con idrogeno, sono stati preparati composti omosostituiti del tipo tetrakis( $\beta$ -dichetiminato)zirconio (**6**) e tetrakis( $\beta$ -chetoimminato)zirconio (**7**). Questi complessi sono stati completamente caratterizzati tramite spettroscopia NMR, spettrometria di massa, analisi elementare e, quando possibile, tramite diffrazione a raggi X su cristallo singolo.

Un'altra classe utile di leganti a base di azoto sono i guanidinati. Come nel caso precedente, composti di formula generale  $Zr(\text{guanidinato})_2(NR_2)_2$  (**12**, **13**) con numero di coordinazione sei sono stati sintetizzati e isolati, così come un complesso con numero di coordinazione cinque del tipo  $Zr(\text{guanidinato})(NR_2)_3$  (**14**).

Le proprietà termiche e la volatilità di questi composti sono state investigate tramite analisi termica (TG e DSC). I complessi a numero di coordinazione sei **1** e **2**, aventi come sostituenti le  $\beta$ -dichetimmine, sono i più volatili. I composti a numero di coordinazione otto presentano una maggiore stabilità termica, ma sono meno volatili. I complessi esacoordinati sostituiti con guanidinati sono meno volatili in confronto ai corrispondenti sostituiti con  $\beta$ -dichetimmine. Tutti i composti a numero di

coordinazione cinque, sia sostituiti con dichetimmine che con guanidinati, non sono volatili.

La pressione di vapore del composto **1** è stata misurata nell'intervallo di temperatura tra 120 e 140 °C, ed il valore di entalpia di sublimazione trovato è  $\Delta H_{\text{subl}} = 90.9 \pm 1.2$  KJ/mol.

Il complesso **1** è stato testato in esperimenti di CVD utilizzando un reattore verticale a pareti fredde. La temperatura del substrato è stata variata tra 450 e 650 °C. La composizione superficiale del film è stata caratterizzata tramite spettroscopia XPS. Sono stati ottenuti film sottili di Zr(C,N) con composizioni variabili a seconda della temperatura. Uno strato superficiale di ossido/ossonitruro si forma sopra il film per effetto dell'esposizione all'aria.



# Table of contents

<b>1. INTRODUCTION .....</b>	<b>12</b>
1.1 MOTIVATION FOR THIS WORK .....	12
1.2 GENERAL CONCEPTS ON CVD .....	15
1.2.1 Introduction.....	15
1.2.2 Description of the process .....	17
1.2.3 Deposition Kinetics .....	18
1.2.4 Hot- and cold-wall reactors.....	20
1.2.5 Additional CVD terminology.....	21
1.3 MOCVD AND PRECURSOR DESIGN .....	23
1.4 PVD: ADVANTAGES AND DISADVANTAGES COMPARED TO CVD .....	25
<b>2 APPLICATION OF GROUP 4 TRANSITION METAL CARBIDES AND NITRIDES</b> .....	<b>30</b>
2.1 HARD, WEAR RESISTANT, LOW-FRICTION COATINGS: AN OVERVIEW .....	30
2.2 GROUP 4 NITRIDES: GENERAL PROPERTIES.....	33
2.3 NOVEL SUPERHARD COATINGS.....	37
2.4 OTHER APPLICATIONS .....	37
<b>3. LITERATURE OVERVIEW.....</b>	<b>41</b>
3.1 $\beta$ -DIKETIMINATO LIGANDS.....	42
3.2 GUANIDINATE-SUPPORTED ZIRCONIUM COMPLEXES.....	44
3.3 CVD OF ZR-BASED COATINGS .....	46
<b>4. RESULTS AND DISCUSSION: SYNTHESSES AND CHARACTERIZATION .....</b>	<b>51</b>
4.1 CHEMISTRY OF $\beta$ -KETOIMINATO- AND $\beta$ -DIKETIMINATO-BASED PRECURSORS .....	52
4.1.1 Reactions with HMeNacNac.....	52
4.1.2 Reaction of HMeNacac.....	54
4.1.3 Five-coordinate $\beta$ -diketiminato-based compounds.....	56
4.1.4 Reactions with HNacNac and HNacac.....	57

4.1.5 Attempts to use (3Z)-5-imino-2,2,6,6,-tetramethylhept-3-en-3-amine.....	59
4.2 NMR CHARACTERIZATION OF $\beta$ -KETOIMINATO- AND $\beta$ -DIKETIMINATO-BASED PRECURSORS.....	61
4.2.1 Compound 1 and 2.....	61
4.2.2 Compound 3, 4, 5.....	66
4.2.3 Compounds 6, 7, 10,11.....	67
4.3 X-RAY CRYSTALLOGRAPHIC STUDIES OF $\beta$ -DIKETIMINATO-BASED COMPOUNDS .....	67
4.3.1 Structure of $Zr(MeNacNac)_2(NMe_2)_2$ and $Zr(MeNacNac)_2(NEt_2)_2$ (1 and 2). .....	68
4.3.2 Structure of $Zr(MeNacac)_2(NEt_2)_2$ (3). .....	71
4.3.3 Structure of $Zr(NacNac)_4$ (6) and $Zr(Nthd)_4$ (10). .....	73
4.4 GUANIDINATO-BASED COMPOUNDS.....	77
4.4.1 Six-coordinate compounds.....	77
4.4.2 Five-coordinate compounds.....	78
4.4.3 Attempts to obtain imido-bound complexes.....	79
4.5 NMR OF GUANIDINATO-BASED COMPOUNDS.....	83
4.5.1 Six-coordinate compounds.....	83
4.5.2 Five-coordinate compounds.....	86
4.5.3 Compound 15.....	86
4.6 SINGLE-CRYSTAL X-RAY DIFFRACTION STUDIES OF GUANIDINATO SUPPORTED PRECURSORS .....	88
4.7 THERMAL PROPERTIES AND STUCTURE-VOLATILITY CORRELATIONS.....	94
4.7.1 $\beta$ -diketiminato-based compounds.....	94
4.7.2 Thermal properties of guanidinato–based compounds.....	100
4.7.3 Vapor Pressure measurements of compound 1. ....	102
4.8 OUTLOOK.....	105
<b>5. RESULTS AND DISCUSSION: CVD EXPERIMENTS.....</b>	<b>109</b>
5.1 CVD KINETICS .....	111
5.2 FILM COMPOSITION.....	113
5.2.1 General considerations.....	113

5.2.2	<i>Composition as a function of pressure.</i>	115
5.2.3	<i>Composition as a function of temperature.</i>	116
5.2.4	<i>Composition as a function of depth.</i>	117
5.2.5	<i>Influence of the gas mixtures.</i>	129
5.2.6	<i>Morphology.</i>	129
<b>6.</b>	<b>EXPERIMENTAL SECTION</b>	<b>133</b>
6.1	ROUTINE ANALYSIS INSTRUMENTATION	133
6.2	SYNTHESES.	133
6.3	CVD EXPERIMENTS	145
6.3.1	<i>CVD reactor.</i>	145
6.3.2	<i>Experimental details about CVD experiments</i>	151
6.4	VAPOR PRESSURE MEASUREMENTS.	151
6.5	FILM CHARACTERIZATION	154
6.5.1	<i>XPS analysis.</i>	154
6.6	X-RAY CRYSTAL STRUCTURE ANALYSES.	156
<b>7.</b>	<b>CONCLUSIONS AND OUTLOOK</b>	<b>166</b>

# 1. INTRODUCTION

## 1.1 Motivation for this work

The aim of this work is the development of new precursors for MOCVD, having substantially improved chemical and physical properties, for the deposition of zirconium-based, nitrogen-containing coatings.

One of the most important classes of metal organic precursors employed, is the four-coordinate tetrakis(dialkylamides) ( $M(NR_2)_4$ ,  $M = Ti, Zr, Hf$ ),<sup>[1-6]</sup> which are highly volatile and thermally stable, but very sensitive to air and moisture. This class of compounds can be viewed as isoelectronic analogues of the four-coordinated metal alcoholates used for MOCVD of zirconium oxide (figure 1.1)<sup>[7, 8]</sup>.

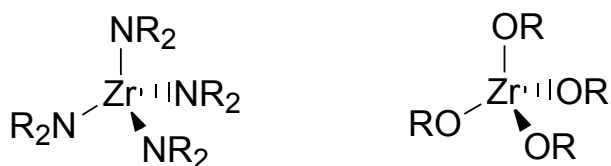


**Figure 1.1: Four-coordinate zirconium dialkylamide and alcoholates**

In the case of nitrides, only minor efforts have been undertaken to tune the precursors toward improved properties. Some studies have been carried out to tailor precursors for TiN thin film applications<sup>[4, 9]</sup>. In the deposition of ZrO<sub>2</sub> thin films, also six-<sup>[10]</sup> and eight-coordinate<sup>[11-15]</sup> precursors have been used, affecting coordinative saturation, which is expected to reduce water and oxygen sensitivity. Such an approach has not yet been pursued for the precursors used in the deposition of transition metal nitrides. Existing precursors for this process have so far not taken such properties into account.

In the course of ZrN deposition studies conducted in our laboratories,<sup>[16]</sup> the precursors shown in figure 1.2 were tested.

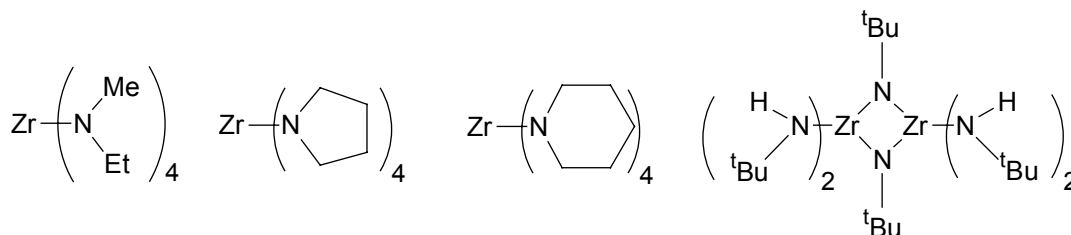


**Figure 1.2: Four-coordinate MOCVD precursors already tested**

All the studied zirconium tetrakis(dialkylamides) were found to have a very high affinity for water and oxygen both during storage and the growth process itself. This prompted us to design new precursors with higher coordination numbers, following the approach already used in the tailoring of zirconium oxide and zirconium silicate single-source precursors.<sup>[17, 18]</sup> An example of these complexes is given in figure 1.3: two bidentate mononegative acetylacetonato ligands and two monodentate alcoholato ligands. This result in a coordination number of six, which enhances the air stability of the compounds and keeps the volatility at the desired level required for MOCVD processes.

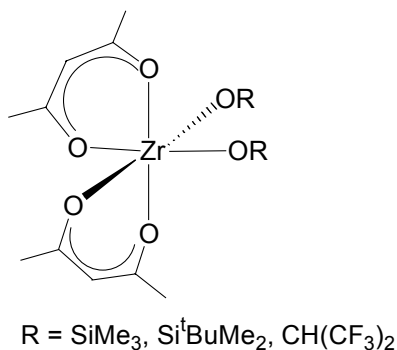
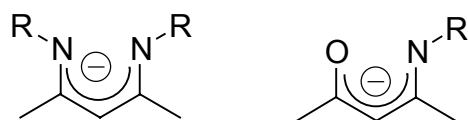


**Figure 1.3: Six-coordinate complexes for oxygen containing Zr-based thin films**

Our tuning efforts have been carried out with the ligand systems shown in figure 1.4. These  $\beta$ -ketoimines and  $\beta$ -diketimines are, in their deprotonated forms, analogues of the  $\beta$ -diketonate fragment, and can be combined with dialkylamido ligands to form compounds of appropriate coordination numbers higher than four, in analogy with the compounds depicted in figure 1.3.



R=H, Alkyl

**Figure 1.4:  $\beta$ -diketiminato and  $\beta$ -ketoiminato ligands in their monoanionic deprotonated form**

Another class of potentially useful ligands is that of amidinates and guanidates, depicted in figure 1.5. Guanidates are particularly interesting, since the ligands can be obtained starting from relatively inexpensive, commercially available starting materials.

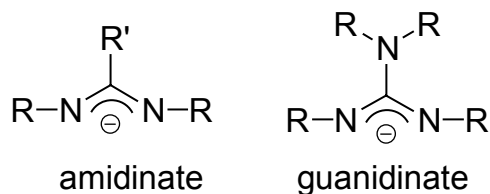


**Figure 1.5 : Bidentate amidinate and guanidinate ligands in the deprotonated form.**

## 1.2 General concepts on CVD

### 1.2.1 Introduction

Chemical vapor deposition (CVD) is a method for depositing films of various materials, and involves the thermally induced reaction of a molecule on a heated surface. The CVD technology combines several scientific and engineering disciplines including thermodynamics, kinetics, fluid dynamics and of course, chemistry. CVD is not a new process. As stated in the pioneer work of Powell, Oxley, and Blocher,<sup>[19]</sup> its first practical use was developed in the 1880s in the production of incandescent lamps to improve the strength of filaments by coating them with carbon or metal. In the same decade, the carbonyl process was developed by Ludwig Mond and others for the production of pure nickel. CVD developed slowly over the next fifty years and was limited mostly to extraction and pyrometallurgy for the production of high-purity refractory metals, such as tantalum, titanium, and zirconium. Several classical CVD reactions were developed at that time, including the carbonyl cycle (the Mond process), the iodide decomposition (the de Boer-Van Arkel process) and the magnesium-reduction reaction (the Kroll process). At the end of World War II, CVD expanded rapidly as researchers realized its advantages for the production of coatings and free standing shapes. Its importance has been growing ever since. Two major areas of application of CVD have rapidly developed in the last twenty years or so, namely in the semiconductor industry and in the so-called metallurgical-coating industry, which includes coating of cutting tools and components. CVD technology is particularly important in the production of semiconductors and related electronic components. Yet, in spite of this progress, many formidable challenges remain, such as the accurate prediction of a given CVD composition and its structure and properties.

CVD is a versatile process suitable for the manufacturing of coatings, powders, fibers, and monolithic components. It is possible to produce most metals, many nonmetallic elements, such as carbon and silicon, as well as a large number of compounds including carbides, nitrides, oxides, borides, diamond, intermetallics, and

many others. This technology is now an essential factor in the manufacture of semiconductors and other electronic components, in the coating of tools, bearings, and other wear-resistant parts and in many optical, optoelectronic and corrosion applications.

The wide range of CVD products is illustrated by the following recent commercial products (updated to 1997):

- Diffusion barrier layers for advanced semiconductor integrated circuits of titanium nitride deposited by metal-organic CVD (MOCVD)
- III/V-semiconductors: GaAs, InP, GaN (blue LED's), poly-Si, epi-Si, BPSG (glassy phase for protection of circuits)
- Diamond-like carbon (DLC) coatings produced by plasma-CVD for bushings and textile components with a much-improved wear resistance.
- Titanium carbide and titanium nitride coatings for carbide tools that greatly outperform uncoated tools and are taking an increasing share of the market.
- Iridium, deposited by MOCVD, which has shown remarkable resistance to corrosion in small rocket nozzles at temperatures up to 2000°C.
- Metallization of semiconductors with copper deposited by MOCVD, replacing aluminum, minimizing electromigration. CVD is now the major process in the production of advanced semiconductor components.
- Energy-saving optical coatings for architectural glass by atmospheric-pressure CVD, produced *in situ* during the processing of float glass.
- Pyrolytic boron-nitride crucibles produced by CVD, with outstanding chemical inertness, which are used extensively in the electronic industry.
- CVD boron fibers, which are extremely stiff and strong, and are used as reinforcement in structural components in aerospace designs.
- High-thermal-conductivity, CVD-diamond films deposited on heat spreaders or heat slugs to dissipate the heat of high-density integrated circuits.



### 1.2.2 Description of the process

A schematic representation of the generalized key steps is presented in figure 1.6. A volatile precursor is transported (1) into the reactor and to the substrate, where it adsorbs (2) and reacts (3) to liberate the supporting ligands, which are subsequently desorbed in initial or pyrolyzed form (6) and transported out of the reactor (7). The adsorbed species then diffuse (4) to form stable a nucleus, where subsequent growth occurs (5). Once a continuous film is formed, growth takes place on the material being deposited.

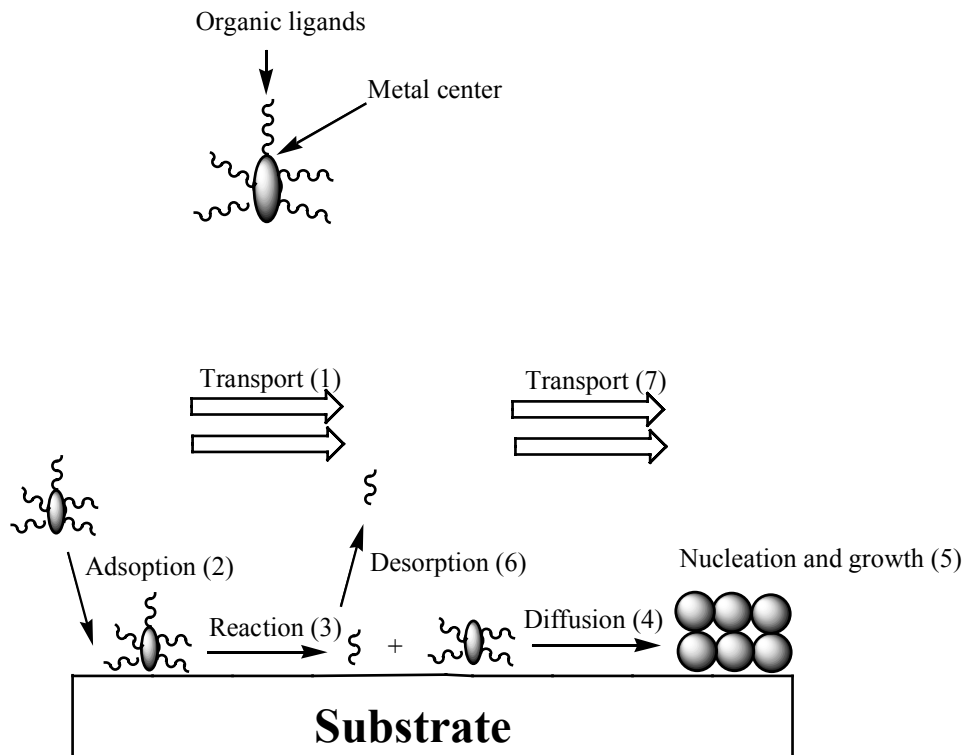


Figure 1.6. Different steps involved in the CVD process.

Inert gas carriers such as  $N_2$  or Ar are often used to enhance the rate of transport of solid or liquid precursors to the reactor chamber. In some cases, other reactive gases, such as  $H_2$ ,  $O_2$  or  $NH_3$ , are employed, which participate in the chemistry of the film deposition by acting as reducing or oxidative gases. Chemical reaction may also occur in the gas phase, depending on the kind of gas employed and on the deposition

conditions. Often gas phase reactions are undesirable because they might result in the nucleation of solid particles, which give rise to impurities, defects, presence of particulates on the film surface, or poor adhesion to the substrate.

### 1.2.3 Deposition Kinetics

Both gas-phase transport rates and surface reaction rates are important for CVD and either of them can be rate limiting. If the surface is at a sufficiently high temperature, the reaction can potentially proceed more rapidly than the rate at which reactant gases are supplied to the substrate. This results in a mass-transport-limited process. If the mass transport is sufficiently fast, the deposition rate may then be limited by the rate at which the reactants are fed to the chamber. The general trend of the growth rate (in logarithmic form) as a function of the inverse of the temperature is depicted in figure 1.7. Feed rate limited deposition usually provides a rate with a weak temperature dependence. Increasing the surface temperature does not result in an increase in the rate, which can be no faster than the rate of delivery of the precursor into the reactor. This case is encountered for precursors with low vapor pressures. For a given system and operating conditions, it can be determined whether the deposition rate is feed-rate limited by estimating the fraction of the precursor consumed by the reaction. This is accomplished by measuring the growth rate and the deposition area, to get the total consumption of precursor by reaction. This value is then compared to the rate at which the precursor is delivered into the reactor. If the fraction (precursor reacted/precursor introduced) is near unity, and little precursor exits the reactor, feed-rate limited deposition is occurring.

For diffusion-limited deposition, the rate depends only weakly on the temperature, primary through the temperature dependence of the diffusion coefficient, which is roughly  $T^{3/2}$ . This dependence is far weaker than the dependence of rate on temperature observed for surface-reaction-limited deposition and is nearly flat when plotted on a logarithmic scale.

In a surface-reaction-controlled process, the rate increases exponentially with temperature according to the Arrhenius relationship. The deposition rate often increases as the substrate temperature increases at low temperatures and low reactant concentrations.

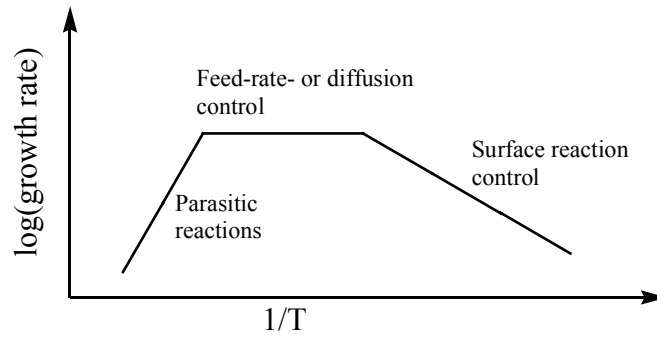


**Figure 1.7. Temperature dependence of the deposition rate.**

Finally, as the substrate temperature is increased, gas-phase particle formation may occur (induced for example by heat irradiation from the substrate), which depletes the reactant concentration, therefore reducing the rate. Alternatively, in this high temperature regime, the precursor rapidly desorbs from the surface before any reaction can occur.

Another factor affecting the deposition rate is, of course, the reactant concentration: as this increases, the deposition rate increases. For feed-rate-limited, deposition, the rate does not depend on the precursor partial pressure or total pressure at a constant feed rate. Therefore, increasing the total pressure while keeping the precursor feed rate constant has little effect on the rate. A test for this limit is to increase the feed rate while keeping all other parameters (total pressure, precursor partial pressure, temperature, etc.) constant and at the same time avoiding diffusion-limited deposition (which can be influenced by changes in gas flow rate). If the deposition rate increases, then the feed-rate is the limiting step. An indicator of a diffusion-limited deposition is that increasing the total pressure while keeping the partial pressure of the precursor constant decreases the rate, because the diffusion coefficient is inversely proportional to the total pressure.

#### 1.2.4 Hot- and cold-wall reactors

The process selected and the size, shape, and number of substrates define the type of reactor and its geometry. Two main reactor types can be distinguished:

1. In the hot-wall reactor, the reactor tube is surrounded by a tube furnace. This means that the substrates and the wall of the reactor have the same temperature. In addition to the film growth occurring on the substrates, film growth might thus take place on the inside of the reactor walls. With thicker films on the reactor walls, there is a risk that particles will break loose from reactor walls, fall down on the surface of the growing film, and introduce pinholes in it. There might also be a source of contamination in this reactor type because of the reaction between the material of the reactor wall and the vapor. In the hot-wall reactor, homogeneous reactions, affecting the deposition reactions and hence the structure of the films, may take place in the vapor. There is a successive depletion with respect to the reactants as they are transported through the reactor. Such a depletion may yield different deposition conditions within the reactor. Finally, in a hot-wall reactor, many substrates can be deposited simultaneously.
2. In the cold-wall reactor, the substrates are heated internally by resistive, inductive or IR radiation heating. The reactor walls thus remain cold and usually no deposition occurs on the walls, eliminating the risk of particles breaking loose from the walls. Furthermore, a low wall-temperature reduces the risk of contaminating vapor/wall reactions. In the cold-wall reactor, the homogenous reactions in the vapor are suppressed and the importance of the surface reactions is increased. The steep temperature gradients near the substrate surface may introduce severe natural convection resulting in a non-uniform film thickness and microstructure. However, with the higher flexibility of the cold-wall reactor, high cleanliness, high deposition rates (yielding high wafer throughput), high cooling rates combined with the needs of thickness uniformity, automatic wafer handling and use of increasing wafer diameter,

there is an increasing tendency to use cold-wall reactors in microelectronics fabrication. A disadvantage is the possibility of the condensation of low-vapor-pressure precursors on the reactor wall.

### **1.2.5 Additional CVD terminology**

**Low Pressure CVD (LPCVD).** Low-pressure CVD technology is widely used in the semiconductor industry due to several advantages over conventional atmospheric-pressure CVD techniques. Operating at lower pressure to increase diffusivity in the gas phase, and allowing the system to be under kinetic control, enhances uniformity of deposition. The mass-transfer rate and the surface-reaction rate are generally of the same order of magnitude at normal atmospheric pressure (conventional CVD), while the mass-transfer rate is much higher than the surface reaction rate at lower pressure, i.e., 0.5–1 torr (LPCVD), and thereby the rate-determining step is the surface reaction. The transfer rates of gaseous reactants and reaction products are inversely proportional to pressure. If the pressure is reduced from 760 torr to 0.5–1 torr, diffusivity increases by a factor of 1000, which is only partially offset by the increase in thickness of the boundary layer (by the square root of pressure). At this low pressure, mass transfer cannot be the rate limiting step, and the deposition rate is mainly controlled by surface reactions, resulting in uniform film thickness, and properties over extended surfaces with better step coverage and conformity, and good structural integrity with fewer pinholes.

**Plasma-Assisted CVD (PACVD)/Plasma Enhanced CVD (PECVD).** Thermal activation is not the only way to promote the precursor reaction. Plasma-assisted chemical vapor deposition (PACVD) can be defined as a process in which the constituents of the vapor phase react to form a solid film assisted by an electric discharge. In the PACVD technique, the gas molecules are mainly dissociated by electron impact, generating very reactive neutral, radical, and ion species. These reactive species arrive on a surface and react with each other via an ionic or free-radical mechanism in the film forming process. Since the gas molecules are activated by energetic electrons instead of thermal energy, the reaction temperature can be

easily reduced. Films can be deposited at temperatures that are typically below 300°C. Furthermore, the inherent limitations of conventional thermodynamics and of chemical availability in thermal CVD are eliminated in plasma activation due to the non-equilibrium nature of the glow-discharge plasma. Neutral radicals are believed to be the major deposition agents among the reactive species generated in the plasma. The number of neutral radicals is determined by a set of variables, which are the glow discharge power, electrode spacing, gas-collision mean free path, and ion diffusibility. The substrate temperature still plays an important role in the PACVD process, although the activation energy for the chemical reaction is provided mainly by the glow discharge. During film growth, the absorbed radical has to diffuse to a stable site to become part of the growing film. This radical mobility on the surface of the substrate is strongly affected by substrate temperature. The radicals on the surface obtained more energy and diffuse to the stable site more easily at high substrate temperature producing a denser film, while at low temperatures, the diffusion of adatoms on the surface is much retarded and thereby the film has more defects and a lower density. There are several advantages of PACVD processes over conventional CVD processes:

1. Ability to deposit films at a much lower temperature.
2. Almost unique method to prepare heavily hydrogenated amorphous silicon films for solar cells and diamond-like carbon (DLC) films.
3. Good adhesion of the films to their substrates
4. Higher deposition rates than by the thermal CVD technique.

The present limitations of PACVD processes are:

1. More defects in the films and a lower density of the film compared to a high temperature deposited film.
2. Difficulties with deposition of pure materials.
3. Limited chamber size because of the necessity to have a large-area homogeneous plasma.

**Laser-Induced CVD (LCVD).** Since the substrate is bombarded by charged and energetic particles, as well as by high-energy radiation in the PACVD process, this

technique can introduce deleterious effects for radiation-sensitive electronic devices. Recently, laser-induced CVD processes have been attracting much attention. In this process the reaction energy is selectively provided by photons. There are two types of processes in LCVD, *pyrolytic LCVD* and *photolytic LCVD*. In pyrolytic LCVD, polyatomic gas molecules are dissociated near a gas-substrate interface by localized heating of the substrate, which is exposed to the laser beam. This technique is limited by the choice of the laser/source gas/substrate. The gas/vapor sources are required to be relatively transparent at the exciting laser wavelength and the substrates strongly absorbing. In photolytic LCVD, a molecule near the substrate is decomposed by means of a photochemical reaction. Specific chemical bonds in polyatomic molecules can be broken selectively through the choice of the laser wavelength. In this technique, photodissociation of the vapor source fixes the maximum allowable wavelength of the laser, since only radiation which is absorbed by the reactants can lead to a photochemical reaction.

### **1.3 MOCVD and precursor design**

The first step in CVD of any material is to consider which molecules may be useful as precursors. The factors that affect the choice of a particular source molecule for CVD of a specific material are complex and depend on the application under consideration. High-purity, dense metal films with controlled crystallite size and smooth surfaces deposited at relatively low temperature ( $< 500\text{ }^{\circ}\text{C}$ ), high deposition rate ( $> 0.1\text{ }\mu\text{m}/\text{min}$ ) and low pressures are required for microelectronic application. Some of these constraints may be relaxed in other coating applications where, for example, high substrate temperatures can be tolerated or impurities are not detrimental.

CVD precursors can be broadly classified into three types: inorganic precursors, which do not contain carbon; metal-organic precursors, which contain organic ligands but no carbon-metal bond and organometallic precursors, which possess an organic ligand and a carbon-metal bond.

There are a number of obvious precursor design requirements that have to be satisfied for a precursor to be useful for CVD. First of all the precursors need high vapor pressures, to achieve high transport rates. Inorganic precursors often exhibit low vapor pressures and high activation energies for the decomposition on the substrate. This situation can be improved using organometallic or metal-organic precursors. There are several design strategies exploited to have compounds with high vapor pressure: first of all the precursor (solid or liquid) should be monomeric. This is sometimes achieved using bulky functional groups on the ligand, which allows the intermolecular distance to be increased, thus decreasing intermolecular forces. Another strategy often used is the introduction of fluorinated ligands, such as the popular bidentate hexafluoroacetylacetonato. The strong carbon-fluorine bond is much less polar than the carbon-hydrogen bond, giving a lower contribution to the molecular polarizability, which implies reduced intermolecular forces. Of course, the main drawback of this approach is the possibility of having undesired fluorine incorporation in the film. In any case, a detailed understanding of the structure-volatility relationship is still lacking, since many factors are involved

Aromatic functional groups on the ligand system should be avoided because of the strong intermolecular  $\pi$ -stacking interaction that they exert.

Ideally, a CVD precursor should not be too air-sensitive, a frequent problem with metal-organic compounds. Air sensitivity is sometimes problematic because it makes the handling and storage of the compounds more difficult. It could also be detrimental during the deposition process (unless we want to deposit metal oxides). A way to decrease air sensitivity is to have a saturated coordination sphere around the metal center, in order to reduce the reactivity towards water or oxygen.

The mechanism of decomposition of the precursor on the substrate is a particular characteristic of the molecule being used and is often a difficult matter to predict. Several experimental and theoretical studies have been carried out so far to address this important issue, but we are still far from being able to predict, *a priori*, the decomposition pathway for a given precursor.



A liquid precursor is always the best situation since the transport from the evaporator system to the reactor can be easily controlled. In contrast a solid precursor might lead to an irreproducible evaporation rate, due to the variation of the exchange surface between the carrier gas and precursor during the process.

## 1.4 PVD: Advantages and disadvantages compared to CVD

Physical vapor deposition (PVD) processes are alternative techniques to CVD for the deposition of thin films. PVD involves the creation of material vapors, (by evaporation, sputtering, or laser ablation) and their subsequent condensation onto a substrate to form the film. The basic PVD processes fall into two general categories: (1) *sputtering* and (2) *evaporation and arc vapor deposition*

*Vacuum Deposition*, which is sometimes called vacuum evaporation is a PVD process in which material from a thermal vaporization source reaches the substrate with little or no collision with gas molecules in the space between the source and substrate. Typically, vacuum deposition takes place in the gas pressure range of  $10^{-5}$  Torr to  $10^{-9}$  Torr. Thermal evaporation is generally done using thermally heated sources such as tungsten wire coils or by high-energy-electron-beam heating of the source material itself. *Sputter Deposition* is the deposition of particles vaporized from a surface (“target”), by the physical sputtering process. Physical sputtering is a non-thermal vaporization process where surface atoms are physically ejected from a solid surface by momentum transfer from an atomic-sized energetic bombarding particle, which is usually a gaseous ion accelerated from a plasma. Generally the source-to-substrate distance is short compared to vacuum deposition. Sputter deposition can be performed by energetic ion bombardment of a solid surface (sputtering target) in a vacuum using an ion gun or low-pressure plasma (<5 mTorr), where the sputtered particles suffer few or no gas phase collisions in the space between the target and the substrate. Sputtering can also be done in a higher plasma pressure (5–30 mTorr), where energetic particles sputtered or reflected from the sputtering target are

“thermalized” by gas phase collisions before they reach the substrate surface. The sputtering source can be an element, alloy, mixture, or a compound and the material is vaporized with the bulk composition of the target. The sputtering target provides a longlived vaporization source that can be mounted so as to vaporize in any direction. Compound materials such as titanium nitride (TiN) and zirconium nitride (ZrN) are commonly reactively sputter-deposited by using a reactive gas in the plasma. The presence of the plasma “activates” the reactive gas (“plasma activation”) making it more chemically reactive. Another PVD-related technique is *arc vapor deposition*. It uses a high-current, low-voltage arc to vaporize a cathodic electrode (cathodic arc) or anodic electrode (anodic arc) and deposit the vaporized material on a substrate. The vaporized material is highly ionized and usually the substrate is biased so as to accelerate the ions (“film ions”) to the substrate surface.

CVD has several important advantages which make it the preferred process in many cases. These can be summarized as follows:

- It is not restricted to a line-of-sight deposition, which is a general characteristic of sputtering, evaporation and other PVD processes. As such, CVD has high throwing power. Deep recesses, holes, and other difficult three-dimensional configurations can usually be coated with relative ease. For instance, integrated circuit via holes with an aspect ratio of 10:1 can be completely filled with CVD tungsten.

- The deposition rate is high, and thick coatings can be readily obtained (in some cases centimeters thick) and the process is generally competitive and, in some cases, more economical than the PVD processes.

- CVD equipment does not normally require ultrahigh vacuum and generally can be adapted to many process variations. Its flexibility is such that it allows many changes in composition during deposition and the co-deposition of elements or compounds is readily achieved.

CVD however is not a universal coating panacea. It has several disadvantages, a major one being that it is most versatile at temperatures of around 600°C and above; many substrates are not thermally stable at these temperatures and coating of precision parts can be a problem because of lack of dimensional stability due to the high temperatures. However, the development of plasma-CVD and metal-organic

CVD partially offsets this problem. Another disadvantage is the requirement of having chemical precursors (the starter materials) with high vapor pressure which are often hazardous and at times extremely toxic. The by-products of the CVD reactions are also toxic and corrosive and must be neutralized, which may be a costly operation.

## References

- [1] D. M. Hoffman, *Polyhedron* **1994**, *13*, 1169.
- [2] D. C. Bradley, I. M. Thomas, *J. Chem. Soc.* **1960**, 3857.
- [3] R. M. Fix, R. G. Gordon, D. M. Hoffman, *J. Am. Chem. Soc.* **1990**, *112*, 7833.
- [4] C. I. M. A. Spee, J. P. A. M. Driessen, A. D. Kuypers, *J. de Physique Colloque IV, Colloque* **1995**, *C5*, 719.
- [5] H. Wendel, H. Suhr, *Appl. Phys. A: Mater. Sci. Process.* **1992**, *54*, 389.
- [6] H. Berndt, A. Q. Zeng, H. R. Stock, P. Mayr, *Surf. Coat. Technol.* **1995**, *74-75*, 369.
- [7] D. C. Bradley, *Chem. Rev.* **1989**, *89*, 1317.
- [8] T. J. Leedham, *Mater. Res. Soc. Symp. Proc.* **1996**, *415*, 79.
- [9] C. H. Winter, T. S. Lewkebandara, J. W. Proscia, A. L. Rheingold, *Inorganic Chemistry* **1994**, *33*, 1227.
- [10] M. Morstein, I. Pozsgai, N. D. Spencer, *Chem. Vap. Deposition* **1999**, *5*, 151.
- [11] A. C. Jones, T. J. Leedham, P. J. Wright, D. J. Williams, M. J. Crosbie, H. O. Davies, K. A. Fleeting, P. O'Brien, *J. Eur. Cer. Soc* **1999**, *19*, 1431.
- [12] J. A. Belot, R. J. McNeely, A. Wang, C. J. Reedy, T. J. Marks, *J. Mater. Res.* **1999**, *14*, 12.
- [13] K. A. Fleeting, P. O'Brien, D. J. Otway, A. J. P. White, D. J. Williamns, A. C. Jones, *Inorg. chem.* **1999**, *38*, 1432.
- [14] G. Garcia, A. Figueras, J. Casado, J. Llibre, M. Mokchah, G. Petot-Ervas, J. Calderer, *Thin Solid Films* **1998**, *317*, 241.
- [15] M. H. Siadati, T. L. Ward, J. Martus, P. Atanasova, C. Xia, R. W. Schartz, *Chem. Vap. Deposition* **1997**, *3*, 311.
- [16] C. P. Allenbach, ETH Zürich, Laboratory for Surface Science and Technology (Zürich), **2000**. <http://e-collection.ethbib.ethz.ch/show?type=diss&nr=13832>
- [17] M. Morstein, *Inorg. chem.* **1999**, *38*, 125.

- [18] S. Zürcher, M. Morstein, N. D. Spencer, M. Lemberger, A. Bauer, *Chem. Vap. Deposition* **2002**, *8*, 171.
- [19] C. F. Powell, in *Vapor Deposition* (Eds.: P. C. F., O. J. H., B. J. M.), John Wiley & Sons, New York, **1966**, p. 249-276.

## 2 APPLICATION OF GROUP 4 TRANSITION METAL CARBIDES AND NITRIDES

### 2.1 Hard, wear resistant, low-friction coatings: an overview

Mankind has used hard surfaces on various tools since antiquity. Examples are:

1. An axe dating back to 900 B.C., possessed a Brinell Hardness value of 444 at the edge where it had been intentionally carburized. A chisel from 700 B.C., less satisfactorily carburized, had a Brinell Hardness of 300 on its edge.<sup>[1]</sup> These are precursors of modern techniques of carburizing and nitriding, which is a chemical vapor deposition process.

2. The ancient precursor to micro- and nano laminate composites are the “Damascus” swords, and the Roman and Viking swords made during the latter centuries of the first millennium A.D. They consisted of finely spaced alternating layers of high-carbon and low-carbon steel, which had been forged to create intricate patterns with the layers stacked in different directions. The result was high strength and toughness and, in the case of Damascus swords, a very pleasing sheen on the surface.<sup>[1]</sup>

Traditionally, the term *hard coatings* refers to the property of high hardness in the mechanical sense with good tribological properties.

Most hard coatings are ceramic compounds such as oxides, carbides, nitrides, ceramic alloys, cermets, metastable materials such as diamond, and cubic boron nitride. Their properties, and environmental resistance depend on the composition, stoichiometry, impurities, microstructure, imperfections, and in the case of coatings, the preferred orientation (texture). Diamond, diamond-like carbon (DLC), cubic boron nitride, and the new class of nano-layered composites are currently referred to as *superhard* materials.

Stricter pollution control requirements demand “green” manufacturing processes. Many machining processes use cutting fluids to cool the workpiece, the tool, and the machine during cutting. The coolant also reduces friction, and the chips created during the operation are removed from the cutting area. Coolants, however, create high costs in production, and can be hazardous to the environment and to human health. For example, the cost of cutting fluid technology (amortization, equipment, staff, service, energy, disposal, etc.) represents about 17% of the costs of machining an engine cylinder heads and a cam shaft. The recycling of the coolant fluids in machining application contribute to 10-40% of the total amount of the machining costs, depending on the type of applications.<sup>[2]</sup>

Transition metal carbides, nitrides and carbonitrides are by far the most widely commercially employed hard coatings, used to improve the mechanical and tribological properties of tool surfaces<sup>[3-7]</sup>. TiN, TiCN, TiAlN, and other coatings have been used to enhance the performance and life of cold-forming tools in processes such as stamping, bending, rolling, extrusion, embossing, etc.<sup>[8]</sup>

The CVD coating materials for wear and corrosion resistance consist mostly of carbides and nitrides and, to a lesser degree, borides and kappa-alumina. Titanium carbide, TiC, with its great hardness and wear resistance, is particularly suitable to reduce mechanical and abrasive wear. However, it is susceptible to chemical attack and is not a good diffusion barrier. Titanium nitride (TiN) is chemically stable. TiN forms an excellent diffusion barrier and has a low coefficient of friction. As such, it is well suited for reducing corrosion, erosion, and galling. It is used extensively as a coating for gear components and tube- and wire-drawing dies. Titanium carbonitride. Ti(C,N) is a solid solution of TiC and TiN and combines the properties of both materials. It offers excellent protection against abrasive wear and has good lubricating characteristics. It is used to coat tools and dies for the processing of ceramics, graphite, and filled plastics. (Ti,Al)N has essentially the properties of TiN but with much higher oxidation resistance. It is now deposited by sputtering and its deposition by CVD is being investigated. Hafnium nitride (HfN) has good oxidation resistance and is being developed as a cutting tool material<sup>[9]</sup>

The evolution and variety of coatings for tribological applications is shown in Table 2.1. The early days, 1968 onwards for CVD coatings, and 1972 onwards for PVD coatings, featured simple compounds such as TiN or TiC. A 2–3 micrometer thick coating on cemented carbide tips produced a 100% improvement in tool life. In 1973, a CVD multilayer coating, TiC-Ti(CN)-TiN, was marketed, and demonstrated remarkable improvements over simple coatings. Subsequent major developments have occurred with the advent, and maturing of PVD technologies.

**Table 2.1 Transition metal nitrides/carbonitrides coatings for High Performance Machining**

Coating	Bulk Vickers Hardness	Friction coefficient Comparative	Adhesion Critical Load Minimum	Uses Application
TiN	~ 2200	~ 0.6	> 55 N	A general coating for various tools and dies. The most widely used and well known coating
Low Temp. TiN	~ 2200	~ 0.6	> 55 N	Used for coating temperature sensitive tools, e.g. brazed carbides, D2 01 dies, bearing steels, etc. Coating temperature 200-300 °C
TiAlN	~ 3500		> 50 N	For higher speed machining, particularly carbide tooling where operational temperatures are increased. Know to work better than TiN on machining tough steels, e.g. D2 and cast irons.
TiZrN	~ 3500	< 0.6	> 50 N	Similar to TiAlN, hardness of up to 4000 Hv can be achieved
ZrN	~ 3300	< 0.6	> 45 N	Very good for the machining of aluminum alloys, always significant improvement over TiN
TiCN	~ 2800	0.6	> 50 N	Though coating suitable for punches. Better than TiN in some application where friction is important
AlTiN	~ 3800	unknown	> 50 N	Used in dry or minimum lubrication machining. Still cubic NaCl phase.



## 2.2 Group 4 nitrides: general properties

Three general and interrelated atomic characteristics play an essential part in the formation of nitrides: the difference in electronegativity between the element nitrogen and the other element forming the nitride, the size of the atoms, and the electronic bonding characteristics of these atoms. Nitrogen has a higher electronegativity than any other of the elements with the exception of oxygen and fluorine. This difference is large with the interstitial nitrides (Ti-N: 1.5, Zr-N:1.6, Hf-N: 1.7) <sup>[10]</sup>. The second factor controlling the formation of nitrides is the atomic radius of the constituent elements. One should note that nitrogen is one of the smallest atoms, and smaller than carbon. Only the early transition metals (Groups 4, 5, and 6) have a host lattice that is large enough for the nitrogen atom to fit readily and so form stable interstitial compounds. Generally speaking, when the difference in radii of the two elements is large, interstitial nitrides are formed (i.e., TiN, ZrN); when it is small, covalent nitrides are formed. The third factor governing the structure of nitrides is the nature of the bond between the nitrogen atom and the other element forming the compound. The difference in electronegativity between nitrogen and the metal is large and so is the difference in atomic size so that the nitrogen atom nests readily in the interstices of the metal lattice.

The nitrides of Group 4 and 5 are considered refractory. The word *refractory* defines a material with a high melting point, i.e. any carbide and nitride with a melting point arbitrarily selected as greater than 1800°C. In addition, to be considered refractory the material must have a high degree of chemical stability.

The interstitial nitrides have several important characteristics:

- They have a complex electronic bonding system which includes metallic, covalent, and ionic components.
- They are primarily non-stoichiometric phases.
- Like ceramics, they have high hardness and strength.
- Like metals, they have high thermal and electrical conductivity.

The interstitial nitrides are susceptible to the presence of even very small amounts of impurities particularly oxygen, which tend to distort the structure. The interstitial

nitrides allow nonmetallic vacancies (i.e., nitrogen) in the lattice, and they also tolerate metal-atom vacancies. This means that if the metal-atom vacancies are more numerous than the nitrogen-atom vacancies, the nitrogen-to-metal ratio will be  $> 1$ . As a result, the structure of interstitial nitrides is sometimes difficult to identify with certainty. There are two types of interstitial sites in the close-packed structure of early transition metals, i.e., the tetrahedral sites and the octahedral sites. The nitrogen atoms occupy only the octahedral sites since the tetrahedral sites are too small to accommodate them. There is one octahedral site per atom of the host metal

Many different compositions are known and, of these, the most common and important is the mononitride, usually expressed as  $MN_x$ , ( $M = \text{metal}$ ). This notation shows that the nitrogen content is variable and the result of incomplete filling of the available sites. The mononitrides have a face-centered-cubic close-packed structure (fcc) where the successive layers follow the sequence ABCABC; the coordination number of the metal atom is 12.

The overall bonding scheme in interstitial nitrides is a combination of the three types of bonding: ionic bonding resulting from a transfer of electrons from the metal to the nitrogen atom, metallic bonding with a finite density of states at the Fermi-energy level and covalent bonding, the major type, between metal  $d$ -state and the nitrogen  $p$ -state with some metal-to-metal interaction. The electronic configuration of the interstitial mononitrides, including the band structure, the density of states, and other bonding considerations, have been the object of much research and are now relatively well defined. A schematic representation of the bonding orbitals of TiN on the (100) crystallographic plane, typical of interstitial mononitrides, involves the formation of a covalent bond between the nitrogen  $p$  orbitals and the titanium  $d$  orbitals, to form both  $\sigma$  and  $\pi$  covalent bonds. The  $\sigma$ -bonded overlapping titanium  $d$  orbitals indicate a certain degree of Ti-Ti interaction. The metallic character of the bond gives the interstitial nitrides properties such as high electrical and thermal conductivities. In addition, these materials have high melting points and high hardness; they are chemically inert but only the nitrides of Groups 4 and 5 fully meet the refractory criteria.

Nitrides formed by the metals of Group 4 (titanium, zirconium, and hafnium) have similar properties and characteristics and titanium nitride has the greatest importance from an application standpoint. Interstitial nitrides are essentially non-stoichiometric compounds, which accounts in part for the variations in the property values reported in the literature (such as hardness and coefficient of friction, for example). Unlike the interstitial monocarbides, MC, where C is never  $>1$ , the interstitial mononitrides, MN, can have a composition where  $x > 1$ . In substoichiometric compositions ( $x < 1$ ), the sublattice of nitrogen is predominantly deficient while at hyperstoichiometric compositions ( $x > 1$ ), the metal lattice is predominantly deficient. The lattice parameter is at a maximum at stoichiometry. Even at stoichiometry, a substantial fraction of both nitrogen and metal sites are usually vacant.

Some interesting physical properties of interstitial nitrides of the group 4 are shown in Table 2.2.

**Table 2.2. Physical properties of binary Group 4 nitrides** <sup>[11]</sup>

	Melting Point (°C)	Density (g/cm <sup>3</sup> )	Electrical Resistivity ( $\mu\Omega\cdot\text{cm}$ )
TiN	2950	5.40	$20 \pm 10$
ZrN	2980	7.32	7-21
HfN	3387	13.8	33

At a nitrogen pressure of 1 MPa, the nitrides of Group 4 melt without decomposition but those of Group V decompose. Large spreads in the reported values are common and are related to differences in stoichiometry, impurity levels, and fabrication processes. These materials have a ductile-brittle transition temperature of approximately 800°C. The Group 4 nitrides generally have higher hardnesses than those of Group 5. This reflects the greater contribution of M-N covalent bonding found in these compounds. Hardness of Group 4 nitrides varies with

composition and reaches a maximum at stoichiometry. A similar behavior is observed for the corresponding carbides. The hardness varies depending on crystal orientation, the (111) orientation being the hardest. [12] The interstitial nitrides are chemically stable and have a chemical resistance similar to that of the Group 4 and 5 carbides. Titanium nitride is completely and mutually soluble with nitrides of Groups 4 and 5. It is isomorphous with TiC as carbon can substitute for nitrogen to form a binary solid solution, titanium carbonitride, Ti(CN), over a wide range of composition.

Zirconium nitride is completely and mutually soluble with the nitrides and carbides of Groups 4 and 5 with the exception of VN and VC. The Zr-N phase diagram is shown in figure 2.1.

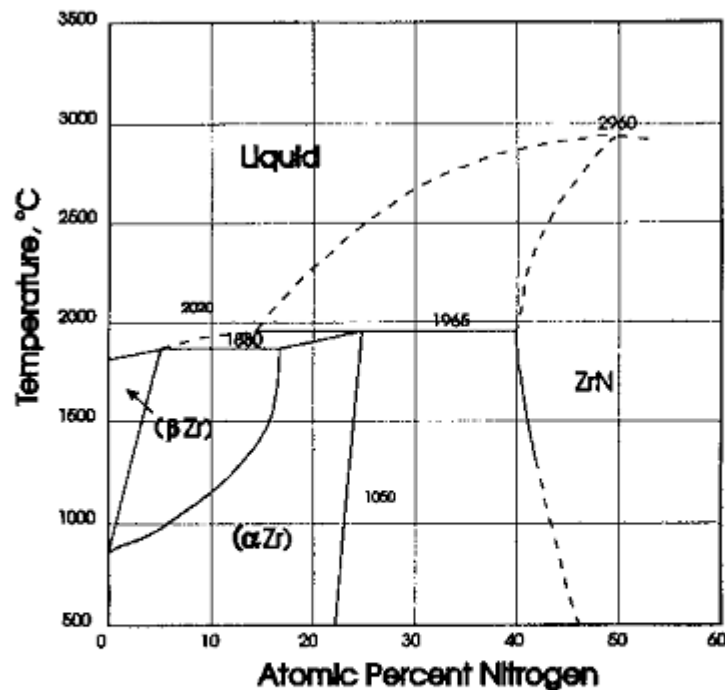


Figure 2.8. Phase Diagram for the Zr-N system.

## 2.3 Novel Superhard Coatings

A novel concept of superhard coating has been advanced by Veprek and his co-workers<sup>[13, 14]</sup>, and has been recently reviewed<sup>[15]</sup>. They propose a nanocrystalline/amorphous composite material. The bulk of the material consists of 4–12 nm crystallites surrounded by amorphous material of 0.3–0.6 nm thickness. Dislocations cannot be generated in the small-sized crystallites, and crack propagation is stopped in the surrounding amorphous mass. They discuss various methods to prepare the nc/a composite, and settle on the low temperature plasma-assisted CVD process to minimize interdiffusion. Ideal candidates for the nanocrystalline phase are the transition metal nitrides such as TiN, VN, ZrN, etc., with amorphous Si<sub>3</sub>N<sub>4</sub> being an ideal candidate for the amorphous phase. According to the Hall-Petch relation the hardness increased rapidly with the decrease in the crystallite size, reaching a value of 50 GPa at crystallite size of 3–4 nm, along with an elastic modulus >500 GPa, which could be reached in a film of thickness 4 to 5 micrometers, and load of 10–50 mN. The nc TiN/a-Si<sub>3</sub>N<sub>4</sub> composites showed a remarkable stability against oxidation up to 800°C and TiAlN/Si<sub>3</sub>N<sub>4</sub> beyond that (up to 1000°C).

## 2.4 Other applications

**Microelectronics applications.** Group 4 transition metal nitrides, in particular TiN and ZrN, have been considered for other applications, for example as diffusion barriers in integrated circuit devices,<sup>[16, 17]</sup> The interface between a metal and semiconductor is unstable; after some time these materials start to interdiffuse causing the failure of the device. For this reason thin films of another material have to be placed between the metal and the semiconductor layer. The materials typically used for this applications is TiN, but the columnar growth of this material might be

problematic at current small features dimensions, 0.18  $\mu\text{m}$  and below.<sup>[16]</sup> For an integrated ferroelectric random access memory (FeRAM) higher than 4 Mbit, a stacked capacitor cell structure is required as a modification of a lateral transistor capacitor. In this case, a direct electrical contact must be formed from the source of the transistor to the bottom of the capacitor via a conducting barrier layer which prevents reaction between the ferroelectric film and the Si substrate. Transition metal nitrides with a NaCl structure have been widely applied as barrier metals for a ferroelectric capacitor because they have high electrical conductivity, a low Schottky barrier,<sup>[18]</sup> and thermal and chemical stability. Among them, ZrN is the most attractive candidate for the barrier metal because it has the lowest resistivity. The dramatic changes in the metallization process taking place in the IC industry is evidencing the needs for new materials for diffusion barriers. Copper will be soon replacing aluminum in metallization schemes. This metal easily reacts with Si (forming  $\text{CuSi}_n$ ) without an effective diffusion barrier, causing the degradation of the devices. There is currently a strong research effort aimed at finding new barrier materials, the best candidate being the Ti-Si-N system.<sup>[19]</sup>

Group 4 transition metal nitrides have been also considered as gate materials,<sup>[20]</sup> thin-film thermistors,<sup>[21]</sup> and Josephson junctions.<sup>[22]</sup>

**Decorative hard coatings.** Cost effective value addition to base metals for decorative and ornamental applications is a subject of major economic importance. Electrochemical methods have been used for a long time for various decorative coatings. The advent of PVD TiN coatings with the characteristic “gold-like” color in the early seventies opened up a new technology for hard decorative coatings. Today, decorative coatings are deposited by various PVD methods, including electron-beam evaporation, cathodic arc evaporation, or magnetron sputtering, or in some machines by a combination of cathodic arc, and magnetron sputtering. The colors available for decorative hard coatings range from metallic tones of CrN, to various bright yellow and gold tones of TiN, TiCN, and TiZrN alloys, as well as other colors such as yellow brown, grey violet, neutral blue grey based on the TiAl alloys, light grey to dark grey

for TiC, and deep black for DLC coatings, or DLC with incorporation of metals such as Ti. Another application which combines the abrasion resistance, corrosion resistance, and a brass color are ZrN coatings on zinc castings for bathroom fixtures and door hardware.

## References

- [1] L. Aitchinson, *A History of Metals*, **1960**.
- [2] T. Cselle, B. A., *Surf. Coat. Technol.* **1995**, 76/77, 712.
- [3] P. C. Johnson, H. Randhava, *Surf. Coat. Technol.* **1987**, 33, 53.
- [4] W. C. Russel, *J. de Physique Colloque* **1995**, C5, 127.
- [5] G. Sundararajan, M. Roy, D. K. Das, *Surf. Eng.* **1997**, 13, 219.
- [6] J. Vetter, R. Rochotzki, *Thin Solid Films* **1990**, 192, 253.
- [7] W. D. Sproul, *Thin Solid Films* **1983**, 107, 141.
- [8] R. F. Bunshah, *Handbook of Hard Coatings: Deposition technologies, properties and applications*, Noyes publications, **2001**.
- [9] J. Oakes, *Thin Solid Films* **1983**, 107, 159.
- [10] F. A. Cotton, G. Wilkinson, *Advanced Inorganic Chemistry*, Interscience Publishers, New York, **1972**.
- [11] H. O. Pierson, *Handbook of Refractory Carbides and Nitrides: Properties, Characteristics, Processing and Applications*, Noyes Publications, **1996**.
- [12] J. E. Sundgren, et-al., in *Physics and Chemistry of Protective Coatings*, Vol. 149, American Institute of Physics Conf. Proc., **1986**.
- [13] S. Veprek, M. Haussmann, S. Reiprich, L. Shizhi, J. Dian, *Surf. Coat. Technol.* **1996**, 86/87, 394.
- [14] S. Veprek, S. Reiprich, *thin solid films* **1995**, 268, 64.
- [15] S. Veprek, *J. Vac. Sci. Technol. A* **1999**, 17, 2401.
- [16] K. Hiramatsu, H. Ohnishi, T. Takahama, K. I. Yamanishi, *J. Vac. Science and Technol. A* **1996**, 14, 1037.
- [17] N. Kobayashi, H. Tanoue, G. Linker, *Nucl. Instr. Meth Phys. Res. B* **1988**, 33, 795.
- [18] J. Wittmer, *J. Vac. Sci. Technol. A* **1985**, 3, 1797.
- [19] X. Liu, Z. Wu, H. Cai, Y. Yang, T. Chen, C. E. Vallet, R. A. Zuhr, D. B. Beach, Z.-H. Peng, Y.-D. Wu, T. E. Concolino, A. L. Rheingold, Z. Xue, *J. Am. Chem. Soc.* **2001**, 123, 8011.



- [20] L. L. Zhang, S. K. Liang, N. W. Cheung, *J. Vac. Science and Technol. B* **1987**, 1716.
- [21] M. Yoshitake, T. Yotsuya, S. Ogawa, *Jpn. J. Appl. Phys* **1992**, 31, 4002.
- [22] K. Schwarz, A. R. Williams, J. J. Cuomo, J. H. E. Harper, H. T. G. Hentzell, *Phys. Rev. B* **1985**, 32, 8312.

### 3. LITERATURE OVERVIEW

#### 3.1 $\beta$ -diketiminato ligands

The interest in the chemistry of  $\beta$ -diketiminates started to grow since the late nineties, although the first example of synthesis of diketimines ligands dates back to 1968, when McGeachin prepared several alkyl-substituted  $\beta$ -diketiminates derived from acetylacetone, and some nickel and cobalt complexes.<sup>[1]</sup> The synthetic procedure is shown in Figure 3.1.

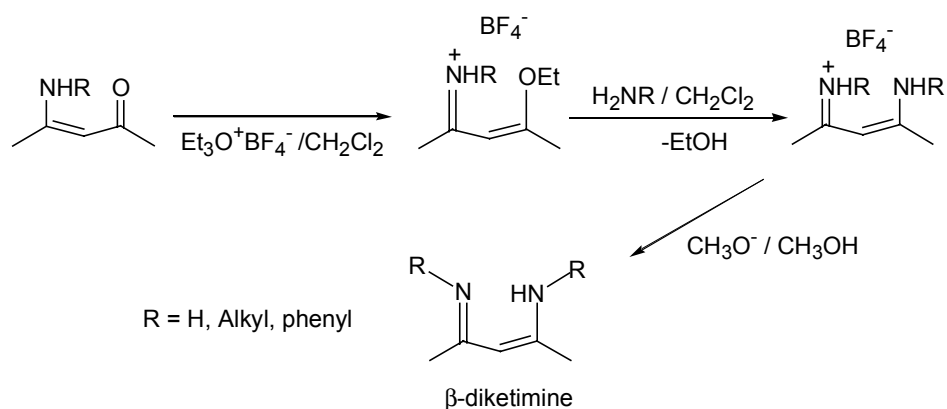


Figure 3.9. Reaction sequence for the synthesis of  $\beta$ -diketiminates

The starting  $\beta$ -ketoimine is converted to the O-alkylated product using the Meerwein salt, then the amine is added *in situ*, to obtain the protonated form of the  $\beta$ -diketimine with tetrafluoroborate as counterion. The latter is deprotonated with sodium methoxide.

From the end of the nineties the number of papers appearing in the literature using  $\beta$ -diketiminato ligands has grown extremely fast, and involves a large portion of the main group, transition metal and lanthanide elements. The common application, these studies are addressed to, is the synthesis of novel catalysts for olefin polymerisation.

The potential advantage of diketiminato ligands is the possibility of modulating steric and electronic properties by using different substituents on the imino nitrogen.

Several examples of  $\beta$ -diketiminato supported aluminum complexes have appeared, often in combination with alkyl ligands.<sup>[2-7]</sup> The synthesis, structure, reactivity of other elements in group 13 and 14 have been investigated, the series including boron,<sup>[8]</sup> gallium,<sup>[9-13]</sup> germanium,<sup>[14, 15]</sup> and tin.<sup>[15, 16]</sup>

Recently, the group of Lappert has investigated lanthanide chemistry using  $\beta$ -diketiminates as ancillary ligands.<sup>[17-20]</sup>

Among transition metals, there are recent examples of  $\beta$ -diketiminato-based zinc compounds which were reported to be active in the copolymerisation of CO<sub>2</sub> with epoxides.<sup>[21]</sup> Some other copper and zinc complexes displayed an interesting reactivity with oxygen.<sup>[22]</sup> Other Cu(I) and Cu(II) complexes have been synthesized.<sup>[23-29]</sup> There is only one report concerning Group 10 transition metals.<sup>[30]</sup> Recently, also chromium, manganese, iron and cobalt have been investigated in combination with  $\beta$ -diketiminates.<sup>[31-34]</sup>  $\beta$ -diketiminato-supported dialkylscandium complexes were synthesized by the group of Piers.<sup>[35-37]</sup> Other examples of scandium-based complexes have been recently reported.<sup>[38, 39]</sup>

$\beta$ -diketiminates have been already investigated for their use as ancillary ligands in group 4 transition metal complexes. In some papers they were sought to replace cyclopentadienyl moieties in organometallic complexes employed in Ziegler-Natta catalysis.<sup>[40-42]</sup> The ligands so far employed in combination with titanium and zirconium were all N-aryl substituted compounds, as for the majority of the previously cited compounds, probably due to their specific properties in catalytic applications. Collins and co-workers prepared a series of five- and six-coordinate  $\beta$ -diketiminato substituted complexes starting from Zr(NMe)<sub>4</sub> or ZrBn<sub>4</sub> (Bn = benzyl).<sup>[40]</sup> The dynamics in solution and reactivity with alkylating reagents was also investigated. Smith and co-workers expanded the previous series of compound: titanium and zirconium complexes were synthesized, slightly different aryl substituent on the imido nitrogen were employed, and some  $\beta$ -ketoiminato structural analogues were also prepared.<sup>[42]</sup> In the same year Smith also reported several five-coordinate zirconium

alkyl complexes supported by  $\beta$ -diketiminate ligands. One year later Collins and Novak reported the first ethylene polymerisation experiments.<sup>[43, 44]</sup> The new five-coordinate trichlorozirconium complex supported by an N-methyl substituted  $\beta$ -diketimine, reported by Novak, appeared to be most active.

### 3.2 Guanidinate-supported Zirconium complexes

Another class of bidentate N-donor ligands are amidinate and guanidinate, whose structure are depicted in Figure 3.2.

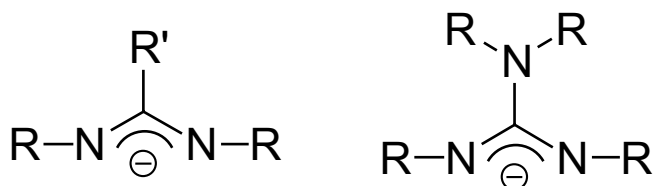
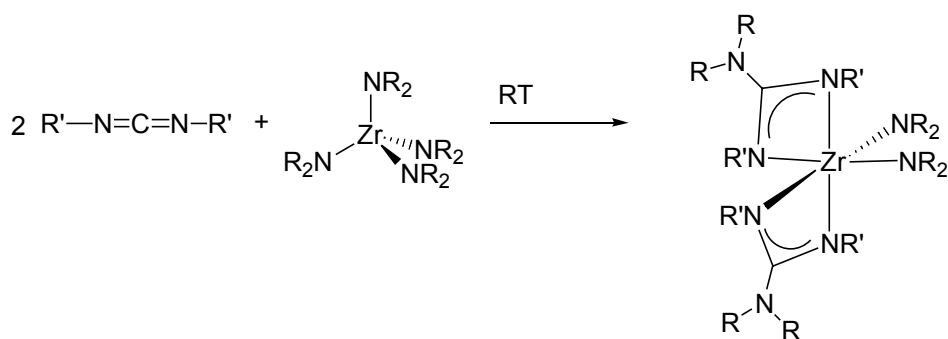


Figure 3.2. Deprotonated form of amidinate and guanidinate ligands.

The first paper reporting the insertion of a carbodiimide into the Zr-N bond of the complex  $Zr(NMe_2)_4$ , dates back to 1970.<sup>[45]</sup> This reaction appears to be particularly useful, since the starting carbodiimide is readily available, and the guanidinate ligand is formed by migration of a dimethylamido group on the carbodiimide carbon, as shown in figure 3.3.



**Figure 3.3. Insertion of carbodiimides into the Zr-N bond**

The interest in these ligands was renewed when the need for alternatives to cyclopentadienyl-based ligands in early transition metal chemistry led many research groups to investigate complexes with N-centered donor ligands. Richeson reported several amidinato-based complexes of the type  $\text{M}(\text{CyNC}(\text{CH}_3)\text{NCy})_2\text{Cl}_2$ , where  $\text{M} = \text{Ti}, \text{Zr}$  and  $\text{Hf}$  using the reaction shown in figure 3.4, and tested them as ethylene polymerisation catalysts.<sup>[46]</sup>

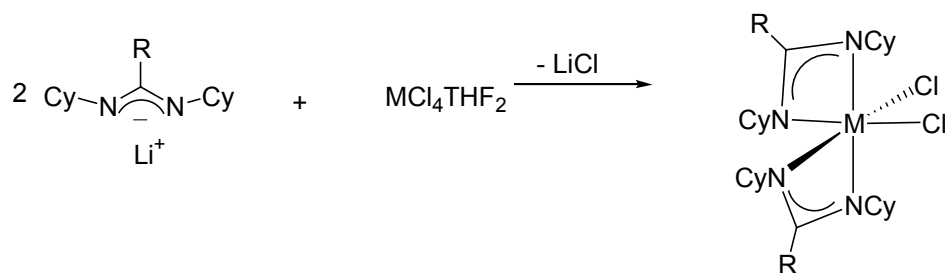


**Figure 3.4. Synthesis of amidinato based complexes**

The same group reported also the guanidinato-based dichlorides using the same salt metathesis reaction shown in Figure 3.4, which allowed them to prepare group 4 compounds of the type  $M\{RNC[N(SiMe_3)_2]NR\}_2Cl_2$ .<sup>[47]</sup>

Giesbrecht et al. synthesized some compounds of the type (guanidinate)Zr(CH<sub>2</sub>Ph)<sub>3</sub> and interestingly report that the crystal packing forces dictate whether the benzyl group displays an  $\eta^1$  or  $\eta^2$  coordination to the Zr atom.<sup>[48]</sup>

Bergman and co-workers investigated other guanidinate-substituted complexes with different substituents, reporting some cationic derivatives and some polymerisation experiments.<sup>[49]</sup>

### 3.3 CVD of Zr-based coatings

The simplest precursor available to deposit ZrN is ZrCl<sub>4</sub>, in the presence of ammonia and N<sub>2</sub>.<sup>[50]</sup> The disadvantage of this process is the high evaporation and substrate temperature, and the production of HCl during the deposition, which is a serious drawback for several applications.

The first precursors employed to deposit nitrogen-containing zirconium-based coatings were Zr(NMe<sub>2</sub>)<sub>4</sub> and Zr(NEt<sub>2</sub>)<sub>4</sub> by Sugiyama et al.<sup>[51]</sup> Using atmospheric pressure CVD, the deposition temperature was 400 and 500 °C respectively for the above mentioned precursors, and the resulting coatings were pale brownish or golden-bronze. Fix et al. used Zr(NEt<sub>2</sub>)<sub>4</sub> and ammonia at atmospheric pressure and a substrate temperature of 200-400 °C to obtain Zr<sub>3</sub>N<sub>4</sub> with low contamination of C and O.<sup>[52]</sup> Other authors used PACVD, and various gas-phase compositions (H<sub>2</sub>, N<sub>2</sub>/H<sub>2</sub>, NH<sub>3</sub>/H<sub>2</sub>), and observed that in the presence of H<sub>2</sub>, films of better characteristics were obtained.<sup>[53]</sup> Täschner et al. used Zr(NEt<sub>2</sub>)<sub>4</sub> to obtain Zr(C,N) films.<sup>[54]</sup> Using H<sub>2</sub>-Ar mixtures led to grey or dark-grey coatings, while the mixture H<sub>2</sub>-N<sub>2</sub>-Ar led to yellow-brown colored films. High oxygen content was found, independent of the process conditions, and addition of nitrogen to the reactor led to lower carbon content. Berndt et al. compared the two precursors Zr(NEt<sub>2</sub>)<sub>4</sub> and Zr(NEtMe)<sub>4</sub> in PACVD experiments.<sup>[55]</sup> The latter precursor is more volatile but led to higher carbon

contamination in the film: this is probably due to the higher tendency of the methyl group to be incorporated into the surface. According to this explanation, the ethyl group can be eliminated more easily, since it can be converted in ethylene by hydrogen elimination. These are, to our knowledge, the only studies undertaken to grow nitrogen-containing, zirconium-based coatings by MOCVD. Only minor efforts have been done to tune the precursors toward improved properties. In our laboratory Allenbach conducted a systematic study of the influence of alkyl substituents on the CVD process of zirconium-based nitrogen-containing coatings, using four coordinate precursors of the type  $Zr(NR_2)_4$ .<sup>[56]</sup> Only studies aimed at tailoring precursors for TiN thin films applications have been reported.<sup>[57, 58]</sup>

## References

- [1] McGeachi.Sg, *Canadian Journal of Chemistry* **1968**, *46*, 1903.
- [2] B. X. Qian, D. L. Ward, M. R. Smith, *Organometallics* **1998**, *17*, 3070.
- [3] C. E. Radzewich, M. P. Coles, R. F. Jordan, *J. Am. Chem. Soc.* **1998**, *120*, 9384.
- [4] C. E. Radzewich, I. A. Guzei, R. F. Jordan, *J. Am. Chem. Soc.* **1999**, *121*, 8673.
- [5] F. Cosledan, P. B. Hitchcock, M. F. Lappert, *Chem. Commun.* **1999**, 705.
- [6] Y. L. Huang, B. H. Huang, B. T. Ko, C. C. Lin, *J. Chem. Soc.-Dalton Trans.* **2001**, 1359.
- [7] C. M. Cui, H. W. Roesky, H. G. Schmidt, M. Noltemeyer, H. J. Hao, F. Cimpoesu, *Angew. Chem.-Int. Edit.* **2000**, *39*, 4274.
- [8] B. X. Qian, S. W. Baek, M. R. Smith, *Polyhedron* **1999**, *18*, 2405.
- [9] N. J. Hardman, C. M. Cui, H. W. Roesky, W. H. Fink, P. P. Power, *Angew. Chem.-Int. Edit.* **2001**, *40*, 2172.
- [10] N. J. Hardman, B. E. Eichler, P. P. Power, *Chem. Commun.* **2000**, 1991.
- [11] N. J. Hardman, P. P. Power, *Chem. Commun.* **2001**, 1184.
- [12] N. J. Hardman, P. P. Power, *Inorg. Chem.* **2001**, *40*, 2474.
- [13] N. J. Hardman, P. P. Power, J. D. Gorden, C. L. B. Macdonald, A. H. Cowley, *Chem. Commun.* **2001**, 1866.
- [14] M. Stender, A. D. Phillips, P. P. Power, *Inorg. Chem.* **2001**, *40*, 5314.
- [15] Y. Q. Ding, H. W. Roesky, M. Noltemeyer, H. G. Schmidt, P. P. Power, *Organometallics* **2001**, *20*, 1190.
- [16] A. Akkari, J. J. Byrne, I. Saur, G. Rima, H. Gornitzka, J. Barrau, *J. Organomet. Chem.* **2001**, *622*, 190.
- [17] A. G. Avent, A. V. Khvostov, P. B. Hitchcock, M. F. Lappert, *Chem. Commun.* **2002**, 1410.
- [18] M. C. Cassani, Y. K. Gun'ko, P. B. Hitchcock, A. G. Hulkes, A. V. Khvostov, M. F. Lappert, A. V. Protchenko, *J. Organomet. Chem.* **2002**, *647*, 71.



- [19] P. B. Hitchcock, M. F. Lappert, S. Tian, *J. Organomet. Chem.* **1997**, *549*, 1.
- [20] P. B. Hitchcock, M. F. Lappert, S. Tian, *J. Chem. Soc.-Dalton Trans.* **1997**, 1945.
- [21] M. Cheng, D. R. Moore, J. J. Reczek, B. M. Chamberlain, E. B. Lobkovsky, G. W. Coates, *J. Am. Chem. Soc.* **2001**, *123*, 8738.
- [22] S. Yokota, Y. Tachi, S. Itoh, *Inorg. Chem.* **2002**, *41*, 1342.
- [23] X. L. Dai, T. H. Warren, *Chem. Commun.* **2001**, 1998.
- [24] B. A. Jazdzewski, P. L. Holland, M. Pink, V. G. Young, D. J. E. Spencer, W. B. Tolman, *Inorg. Chem.* **2001**, *40*, 6097.
- [25] D. W. Randall, S. D. George, P. L. Holland, B. Hedman, K. O. Hodgson, W. B. Tolman, E. I. Solomon, *J. Am. Chem. Soc.* **2000**, *122*, 11632.
- [26] D. J. E. Spencer, N. W. Aboeella, A. M. Reynolds, P. L. Holland, W. B. Tolman, *J. Am. Chem. Soc.* **2002**, *124*, 2108.
- [27] W. B. Tolman, D. J. E. Spencer, A. M. Reynolds, P. L. Holland, B. A. Jazdzewski, V. G. Young, *J. Inorg. Biochem.* **2001**, *86*, 107.
- [28] W. B. Tolman, P. L. Holland, B. A. Jazdzewski, A. M. Reynolds, L. L. Bowen, D. J. E. Spencer, D. C. Price, M. Pink, V. G. Young, *Abstr. Pap. Am. Chem. Soc.* **2001**, *221*, 16.
- [29] S. Yokota, Y. Tachi, N. Nishiwaki, M. Ariga, S. Itoh, *Inorg. Chem.* **2001**, *40*, 5316.
- [30] J. Feldman, S. J. McLain, A. Parthasarathy, W. J. Marshall, J. C. Calabrese, S. D. Arthur, *Organometallics* **1997**, *16*, 1514.
- [31] A. Panda, M. Stender, R. J. Wright, M. M. Olmstead, P. Klavins, P. P. Power, *Inorg. Chem.* **2002**, *41*, 3909.
- [32] J. M. Smith, R. J. Lachicotte, P. L. Holland, *Chem. Commun.* **2001**, 1542.
- [33] V. C. Gibson, C. Newton, C. Redshaw, G. A. Solan, A. J. P. White, D. J. Williams, *Eur. J. Inorg. Chem.* **2001**, 1895.
- [34] L. A. MacAdams, W. K. Kim, L. M. Liable-Sands, I. A. Guzei, A. L. Rheingold, K. H. Theopold, *Organometallics* **2002**, *21*, 952.
- [35] P. G. Hayes, W. E. Piers, L. W. M. Lee, L. K. Knight, M. Parvez, M. R. J. Elsegood, W. Clegg, *Organometallics* **2001**, *20*, 2533.

- [36] P. G. Hayes, W. E. Piers, R. McDonald, *J. Am. Chem. Soc.* **2002**, *124*, 2132.
- [37] L. W. M. Lee, W. E. Piers, M. R. J. Elsegood, W. Clegg, M. Parvez, *Organometallics* **1999**, *18*, 2947.
- [38] L. K. Knight, W. E. Piers, R. McDonald, *Chem.-Eur. J.* **2000**, *6*, 4322.
- [39] A. M. Neculai, H. W. Roesky, D. Neculai, J. Magull, *Organometallics* **2001**, *20*, 5501.
- [40] M. Rahim, N. J. Taylor, S. X. Xin, S. Collins, *Organometallics* **1998**, *17*, 1315.
- [41] L. Kakaliou, W. J. Scanlon, B. X. Qian, S. W. Baek, M. R. Smith, D. H. Motry, *Inorg. Chem.* **1999**, *38*, 5964.
- [42] B. X. Qian, W. J. Scanlon, M. R. Smith, D. H. Motry, *Organometallics* **1999**, *18*, 1693.
- [43] X. Jin, B. M. Novak, *Macromolecules* **2000**, *33*, 6205.
- [44] R. Vollmerhaus, M. Rahim, R. Tomaszewski, S. X. Xin, N. J. Taylor, S. Collins, *Organometallics* **2000**, *19*, 2161.
- [45] G. Chandra, A. D. Jenkins, M. F. Lappert, Srivasta.Rc, *Journal of the Chemical Society a -Inorganic Physical Theoretical* **1970**, 2550.
- [46] A. Littke, N. Sleiman, C. Bensimon, D. S. Richeson, G. P. A. Yap, S. J. Brown, *Organometallics* **1998**, *17*, 446.
- [47] D. Wood, G. P. A. Yap, D. S. Richeson, *Inorg. Chem.* **1999**, *38*, 5788.
- [48] G. R. Giesbrecht, G. D. Whitener, J. Arnold, *Organometallics* **2000**, *19*, 2809.
- [49] A. P. Duncan, S. M. Mullins, J. Arnold, R. G. Bergman, *Organometallics* **2001**, *20*, 1808.
- [50] S. Kudapa, K. Narasimhan, P. Boppana, W. C. Russell, *Surf. Coat. Technol.* **1999**, *121*, 259.
- [51] K. Sugiyama, S. Pac, Y. Takahashi, S. Motojima, *J. Electrochem. Soc.* **1975**, *122*, 1545.
- [52] R. M. Fix, R. G. Gordon, D. M. Hoffman, *J. Am. Chem. Soc.* **1990**, *112*, 7833.
- [53] H. Wendel, H. Suhr, *Appl. Phys. A-Mater. Sci. Process.* **1992**, *54*, 389.
- [54] C. Taschner, K. Bartsch, A. Leonhardt, *Surf. Coat. Technol.* **1993**, *61*, 158.
- [55] H. Berndt, A. Q. Zeng, H. R. Stock, P. Mayr, *Surf. Coat. Technol.* **1995**, *74-5*, 369.

- [56] C. P. Allenbach, Dissertation ETH Zürich, Department of Materials Sciences, (Zürich), **2000**.  
<http://e-collection.ethbib.ethz.ch/show?type=diss&nr=13832>
- [57] C. Spee, J. Driessen, A. D. Kuypers, *J. Phys. IV* **1995**, 5, 719.
- [58] C. H. Winter, T. S. Lewkebandara, J. W. Proscia, A. L. Rheingold, *Inorg. Chem.* **1994**, 33, 1227.

## 4. RESULTS AND DISCUSSION: SYNTHESSES AND CHARACTERIZATION

### 4.1 Chemistry of $\beta$ -ketoiminato- and $\beta$ -diketiminato-Based Precursors

#### 4.1.1 Reactions with HMeNacNac.

One of the most versatile ligands used during this thesis work was the methyl-substituted  $\beta$ -diketimine N-methyl-4-(methylimino)pent-2-en-2-amine, which is formally derived from acetylacetonone (abbreviated “Hacac”), after substitution of the two oxygen by N-Me groups (thus we will abbreviate it as “HMeNacNac”, for simplicity). This ligand can be obtained from relatively cheap starting materials on a multigram scale following the procedure shown in Figure 3.1, Chapter 3. As mentioned in Chapter 3, some five- and six-coordinated complexes with  $\beta$ -diketiminato and dialkylamido ligands in a 2:2 ratio have been already described by Collins and co-workers<sup>[1]</sup>, and by Smith and co-workers.<sup>[2, 3]</sup> Amide substitution is a suitable synthetic route to introduce weakly acidic ligands into the coordination sphere of homoleptic compound such as  $M(NR_2)_4$ .<sup>[4, 5]</sup> Reaction of 2 equivalents of HMeNacNac with  $Zr(NMe_2)_4$  (figure 4.1) proceeds smoothly at room temperature with elimination of two equivalents of  $HNMe_2$  and provides the desired compound **1** in good yield. Reaction with  $Zr(NEt_2)_4$  requires higher temperatures (90 °C), which results in lower yields, presumably due to partial thermal degradation. Attempts to obtain compound **2** under milder conditions (for instance 70 °C) and longer reaction time (48 h) were unsuccessful. Under these conditions zirconium tetrakis(dialkyl) amides bearing alkyl substituents other than  $CH_3$ , are reluctant to undergo amine elimination. This has already been reported by Jordan and co-workers,<sup>[6-8]</sup> and is likely due to the higher steric congestion around the metal center.

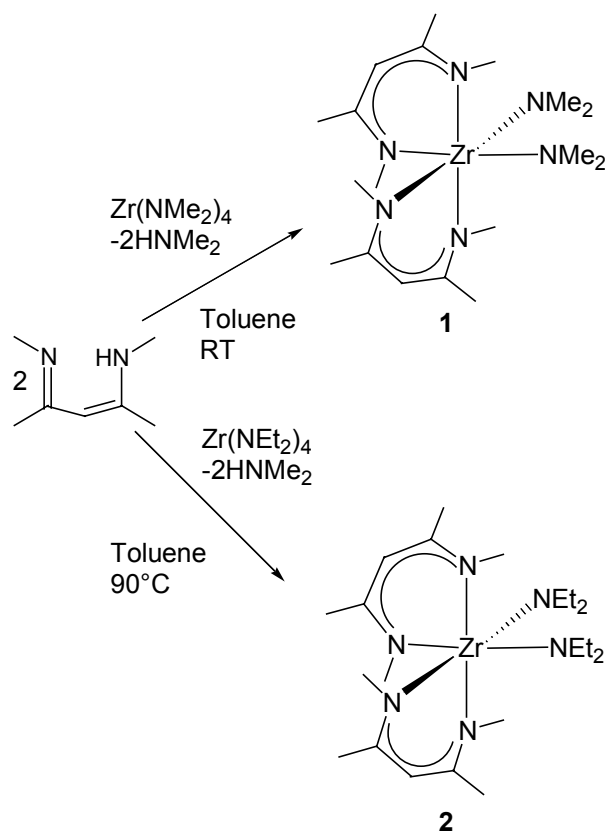


**Figure 4.1. Synthesis of six-coordinated  $\text{Zr}(\text{MeNacNac})_2(\text{NR}_2)_2$  complexes**

Despite their similarities, compounds **1** and **2** display different dynamic behaviour in solution and this aspect will be analysed in the NMR-characterization section.

An alternative reaction route to obtain these compounds was considered. This involves the synthesis of the lithium salt  $\text{LiMeNacNac}$  (by reaction of  $\text{HMeNacNac}$  with  $\text{BuLi}$ ), and the subsequent reaction with  $\text{ZrCl}_4\text{thf}_2$  in order to have  $(\text{MeNacNac})_2\text{ZrCl}_2$ . After isolation and characterization of the latter compound, this was allowed to react with 2 equivalent of  $\text{LiNEt}_2$ , using  $\text{Et}_2\text{O}$  as solvent (the overall reaction scheme is shown in figure 4.2). The reaction did not proceed in the desired direction. The NMR spectrum of the reaction product was different from that of compound **2**, presenting many unidentified signals. This reaction scheme is probably

not the best choice, due to the high basicity of the LiNEt<sub>2</sub> entering group, which probably attack the  $\beta$ -diketiminato ligand ring protons.

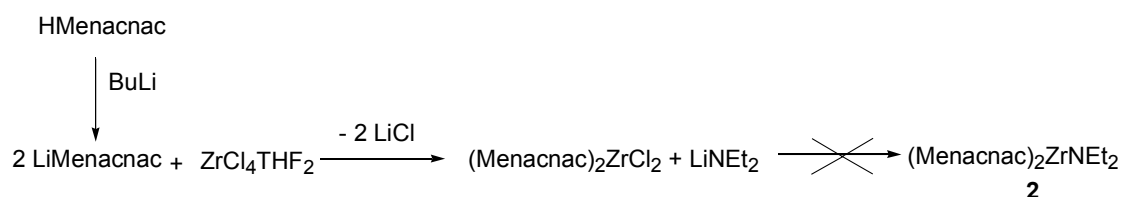


**Figure 4.2. Alternative synthetic route to six-coordinate compounds**

Attempts to use the complex Zr(NMeEt)<sub>4</sub> to produce six-coordinate compounds was unsuccessful. Even using high-temperature reaction conditions, only the five-coordinate compound was obtained (see section 4.1.3).

#### 4.1.2 Reaction of HMeNacac.

By analogy with the abbreviation used previously, we will name the 4-(methylamino)pent-3-en-2-one compound as “HMeNacac”. It is an intermediate in the synthesis of HMeNacNac. We thought it would be interesting to prepare complexes with a mixed coordination sphere around the zirconium metal center, not only bearing nitrogen donor atoms. In view of an application as a zirconium nitride CVD precursor, however, these ligands appear not to be the best choice. However, the presence of oxygen atoms directly bound to zirconium could be exploited to produce Zr(O, N) layers. Furthermore it was planned to investigate how the type of coordinative environment could influence the thermal stability and the volatility of the precursors. As a first starting point we aimed at the generation of six-coordinate compounds isostructural with complexes **1** and **2**. Reaction of two equivalents of HMeNacac with

Zr(NEt<sub>2</sub>)<sub>4</sub> at room temperature (Figure 4.3) produces the desired Zr(MeNacac)<sub>2</sub>(NEt<sub>2</sub>) species in 57% yield after crystallisation.

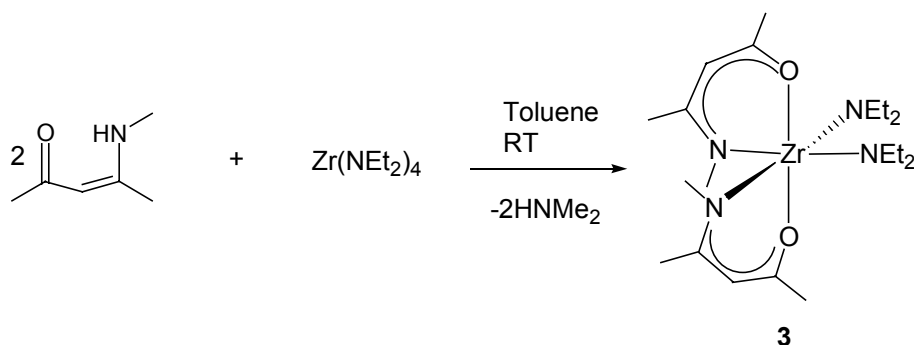


**Figure 4.3. Synthesis of the Schiff-base supported six-coordinate compound 3**

The complex bears two ethylamido and two  $\beta$ -ketoiminato moieties (**3**). The same reaction with  $\text{Zr}(\text{NMe}_2)_4$  gave a complex mixture, which could not be fully characterised. On the basis of the <sup>1</sup>H NMR spectra the desired product seemed to be present, but it was not possible to isolate it from the reaction mixture. This is explained on the basis of the assumption that amine elimination proceeds well when slow exchange allows the stoichiometry to be controlled.  $\beta$ -diketimines are less acidic and more sterically encumbered than the corresponding  $\beta$ -ketoimines, and therefore the reactions proceeded smoothly. In the case of the reaction with  $\text{Zr}(\text{NEt}_2)_4$ , the presence of an ethyl group slows down the substitution, thereby allowing the desired stoichiometry to be obtained. Another reason for the unsuccessful reaction of the  $\beta$ -ketoimine with  $\text{Zr}(\text{NMe}_2)_4$  may be an intrinsic thermal instability of the  $\beta$ -ketoiminato complexes. Compound **3**, if allowed to stand for 72 hours at room temperature, starts to decompose even under nitrogen, as indicated by a change in colour from yellow to deep red. In contrast, it can be stored for an indefinite time at -20°C and, if care is taken, it is possible to obtain a satisfactory elemental analysis and also to grow good quality single crystals for an X-ray diffraction study.

#### 4.1.3 Five-coordinate $\beta$ -diketiminato-based compounds.

Attempts to obtain six-coordinate compounds containing two N-isopropyl substituted  $\beta$ -diketiminato ligands (HPrNacNac) and two dialkylamido groups were unsuccessful. The reaction of two equivalents of HPrNacNac with one equivalent of  $\text{Zr}(\text{NMe}_2)_4$  gave, after a reaction time of 24 h at  $90^\circ\text{C}$ , a clean mixture of one equivalent of the unreacted ligand, plus a product that is consistent with a 1:3 stoichiometric ratio between the bidentate ligand, and the dimethylamido ligand (Figure 4.4). This compound was subsequently prepared by mixing one equivalent of  $\text{Zr}(\text{NMe}_2)_4$  and one equivalent of HPrNacNac, affording the five-coordinate compound **4** in a quantitative yield. Reaction of the same  $\beta$ -diketimine ligand with  $\text{Zr}(\text{NEt}_2)_4$  in a 1:1 stoichiometric ratio gave no reaction products, even after repeated stirring at  $110^\circ\text{C}$  for 48 h.

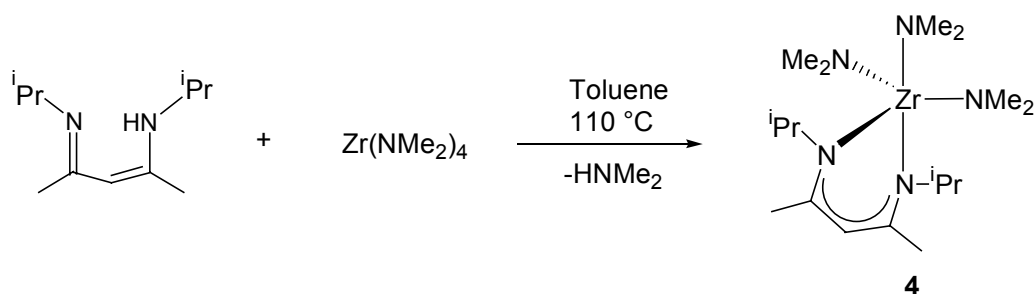
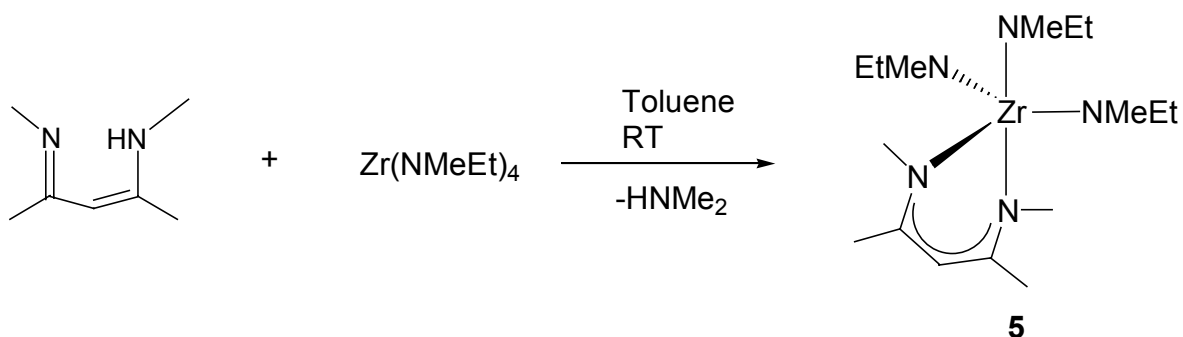


Figure 4.4. Synthesis of  $\beta$ -diketiminato-based five-coordinate compound **4**.

As already mentioned in section 4.1.1, the reaction of the complex  $\text{Zr}(\text{NMeEt})_4$  with two equivalents of HMeNacNac in toluene at  $90^\circ\text{C}$  afforded only the five-coordinate compound  $\text{Zr}(\text{MeNacNac})(\text{NMeEt})_3$  (**5**) plus one equivalent of unreacted HMeNacNac. Compound **5** is a liquid, which is a desired property for CVD applications. Therefore, the compound was synthesized purposely according to the



scheme shown in Figure 4.5. Reactions between HPrNacNac and  $\text{Zr}(\text{NEt}_2)_4$  in a 1:1 stoichiometric ratio, gave no reaction products. Even at temperature as high as 90 °C for 2 days, the NMR only revealed the presence of the signals of the starting materials.



**Figure 4.5.** Synthesis of the five-coordinate  $\beta$ -diketiminato-based compound **5**

#### 4.1.4 Reactions with HNacNac and HNacac.

The N-hydrogen substituted compounds 4-iminopent-2-en-2-amine and 4-aminopenten-2-one (HNacNac and Hnacac), are the least sterically demanding  $\beta$ -diketiminato ligands. It was decided to investigate the reactivity with respect to an amido exchange reaction of the  $\text{Zr}(\text{NR}_2)_4$  complexes. However in this case a completely different reactivity was found (Figure 4.6). As one might expect, the reaction of two equivalents of the above ligand proceeds faster than in the case of the N-methyl substituted compound. A sudden change in colour is observed (from yellow to deep red), and the NMR analysis of the crude reaction product revealed the presence of a mixture of  $\text{Zr}(\text{NR}_2)_4$  ( $\text{R} = \text{Me}, \text{Et}$ ), plus signals typical of  $\beta$ -diketiminato ligands. This was attributed to the formation of homoleptic, eight-coordinate compound tetrakis( $\beta$ -diketiminato)zirconium (see Figure 4.6). This molecule (**6**) has been prepared by the reaction of four equivalents of the ligand with  $\text{Zr}(\text{NMe}_2)_4$ , recovering the desired product in 47% yield. The same behaviour was observed also

for the parent  $\beta$ -aminoketone (Figure 4.6). Reaction between four equivalents of 4-amino-3-penten-2-one yields the eight-coordinate molecule **7** as a white solid. The reason why the heteroleptic six-coordinate compound cannot be isolated is presumably, that as soon as it forms it undergoes a ligand disproportionation in solution, rearranging and giving the thermodynamically more stable eight-coordinate compound. Compound **6** can also be synthesised in higher yield by salt metathesis in the reaction of four equivalents of the lithium salt of 2-amino-4-imino-2-pentene (generated in-situ with BuLi) and one equivalent of  $\text{ZrCl}_4(\text{thf})_2$  in tetrahydrofuran. Attempts to obtain eight-coordinate compounds using four equivalents of LiMeNacNac were all unsuccessful, and the only compound obtained was the dichloride complex  $(\text{MeNacNac})_2\text{ZrCl}_2$ . It is evident that the presence of the imido methyl groups prevent the possibility of accomodating more than two of these N-methyl substituted diketiminates around the metal center for steric reasons.

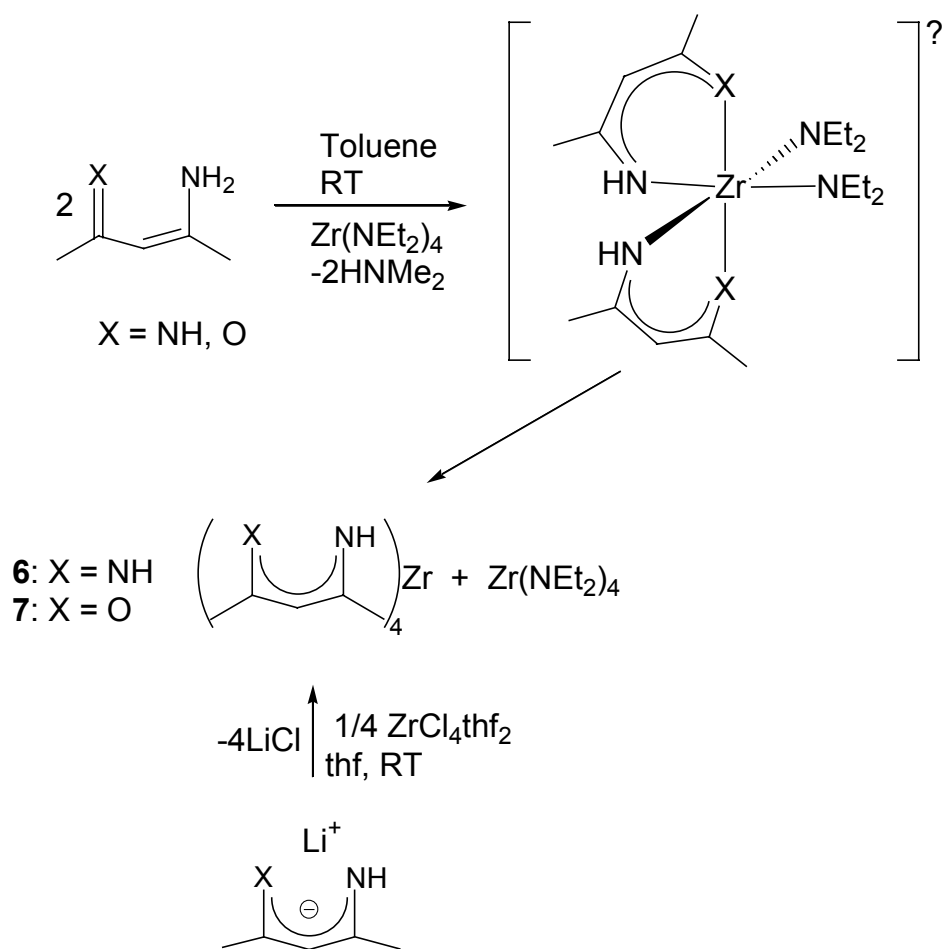
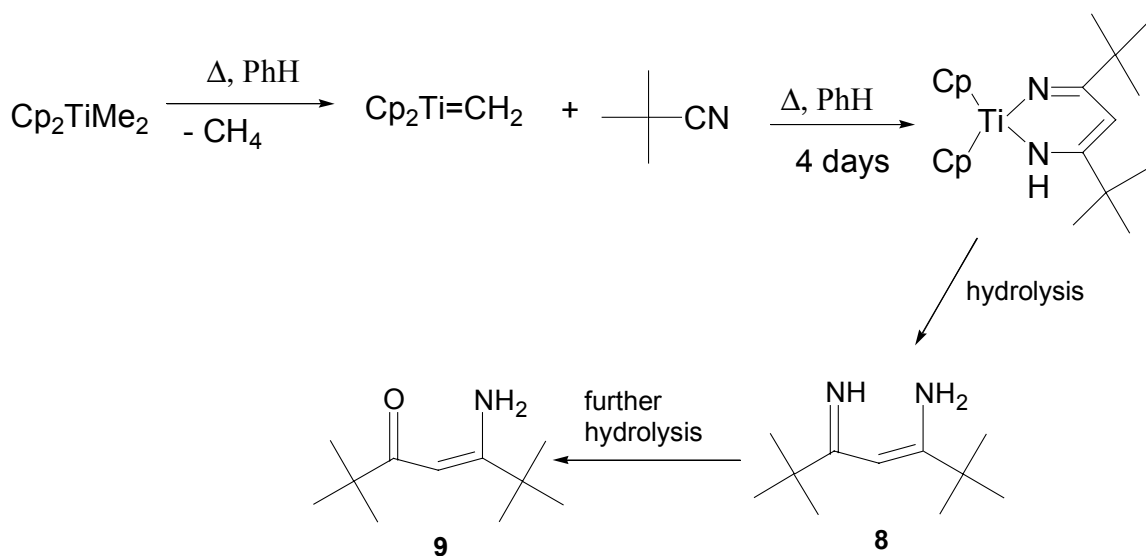


Figure 4. 6. Synthesis of eight-coordinate compounds

#### 4.1.5 Attempts to use (3Z)-5-imino-2,2,6,6,-tetramethylhept-3-en-3-amine.

Barluenga *et al.* reported the synthesis of N-hydrogen substituted diketimines, containing <sup>t</sup>Bu groups instead of methyls on the diketimines skeleton (Figure 4.7).<sup>[9]</sup> This procedure is attractive since the diketiminato ring is built around a titanium metal center in one step.



**Figure 4.7. Synthesis of t-Bu ring-substituted diketimines.**

The name of the ligand (3Z)-5-imino-2,2,6,6,-tetramethylhept-3-en-3-amine (8), will be abbreviated with HN<sub>2</sub>thd, by analogy with the oxygenated counterpart, called Hthd. It is particularly interesting in order to obtain compounds analogous to the oxygen-based Zr(thd)<sub>4</sub>, already tested in CVD experiments.<sup>[10, 11]</sup> By stirring a mixture of Cp<sub>2</sub>TiMe<sub>2</sub> with t-butylacetonitrile at 60 °C in benzene for 4 days, the intermediate carbene Cp<sub>2</sub>Ti=CH<sub>2</sub> is formed, and subsequently it undergoes an insertion reaction with the nitrile. The NMR analysis of the black, crude solid from this reaction revealed the presence of the signals of the insertion product shown in Figure 4.7: no other signals were present. On the other hand, the elemental analysis revealed that the product was impure, all impurities being apparently totally NMR inactive. Attempts to purify this intermediate were not successful. The subsequent hydrolysis step was carried out as described in the literature, but unfortunately the desired product was not synthesized with a good yield and sufficiently pure form. Several reaction conditions were tried to enable controlled hydrolysis: for example treatment with Na<sub>2</sub>SO<sub>4</sub>·10H<sub>2</sub>O (the method reported in the literature), affords as a byproduct the ketoiminato compound derived from the reaction of 8 with water (compound 9 see

figure 4.7). 1 M HCl in Et<sub>2</sub>O gave additional decomposition products and led to the protonation of compound **8**. In one of the experiments carried out to obtain **8**, we isolated the product in about 10% yield, and this small quantity was used to probe whether the desired eight-coordinate compound is achievable. Analogously an eight-coordinate compound was prepared from molecule **9**, which was obtained in a reasonable yield when the hydrolysis was carried out for long time, in large excess of Na<sub>2</sub>SO<sub>4</sub>·10H<sub>2</sub>O. The reaction scheme is shown in figure 4.8, and involves the usual salt metathesis with elimination of LiCl.

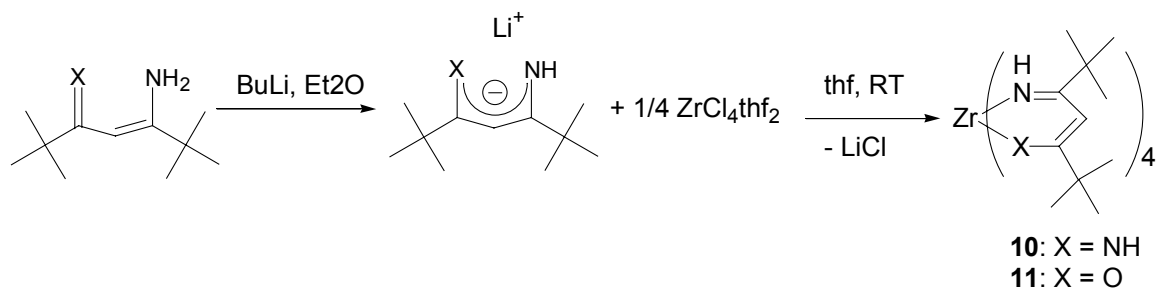


**Figure 4.8.** Synthesis of 'Bu ring-substituted diketimines.

## 4.2 NMR characterization of $\beta$ -ketoiminato- and $\beta$ -diketiminato-based precursors.

### 4.2.1 Compound **1** and **2**.

The NMR spectra of **1** and **2** provided us interesting information about their dynamic behaviour in solution. The <sup>1</sup>H NMR spectra of compound **1** between -50 °C

and at 20 °C are shown in Figure 4.10. At 20 °C it is possible to detect the singlet of the methyne ring proton at 4.66 ppm, the singlet of the methylamido group at 3.00 ppm and only very broadened signals for the other resonance. At 0°C, two resonances for the methyl of the imido group and two resonances for the methyl group of the ring start to appear as broad signals. As shown in Figure 4.10, these resonances become sharp singlets at -40 °C, centered at 3.33 and 2.46 ppm and at 1.89 and 1.67 ppm for the imido and the ring methyls, respectively. No splitting of the signals of the dimethylamido group is observed as a function of temperature. The  $^{13}\text{C}$  NMR spectra also reveal this kind of dynamic feature. For example, in the region around 160 ppm, the imido carbon resonances were expected to appear, but this chemical shift region was completely free of signals, whereas at lower temperature of -40°C two sharp singlets at 166.7 and 162.6 ppm evolved. This is typically seen in the presence of an enantiotopic center, in which two diastereotopic sites are rapidly exchanging at high temperature, but can be distinguished at lower temperature. This phenomenon has been observed recently for six-coordinate zirconium compounds containing N-aryl substituted  $\beta$ -diketiminato ligands, and has been interpreted as a process evolving along a Bailar-twist mechanism<sup>[1, 2, 12]</sup>, shown in Figure 4.11. In the picture, the three nitrogen atoms form one face of the octahedron around the zirconium atom: by rotating these two triangles with respect to each other we obtain a symmetric trigonal-prismatic intermediate. At low temperature the interconversion is slow, and the methyl protons *a* and *a'* are inequivalent, giving rise to two NMR signals. The same for *b* and *b'*, whose chemical shift difference is quite high. At room temperature, this interconversion is fast on the NMR time scale and only one signal appears for *a* and *a'*. *b* and *b'* have a much larger chemical shift difference and cannot coalesce at room temperature but they broaden to a large extent.

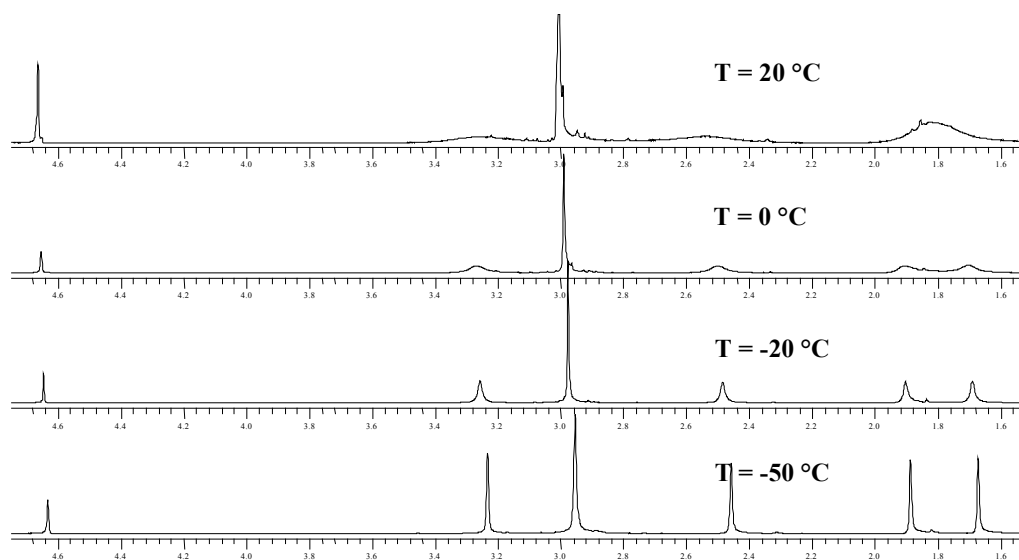


Figure 4.10. Variable temperature  $^1\text{H-NMR}$  of complex 1 in  $\text{CD}_2\text{Cl}_2$ .

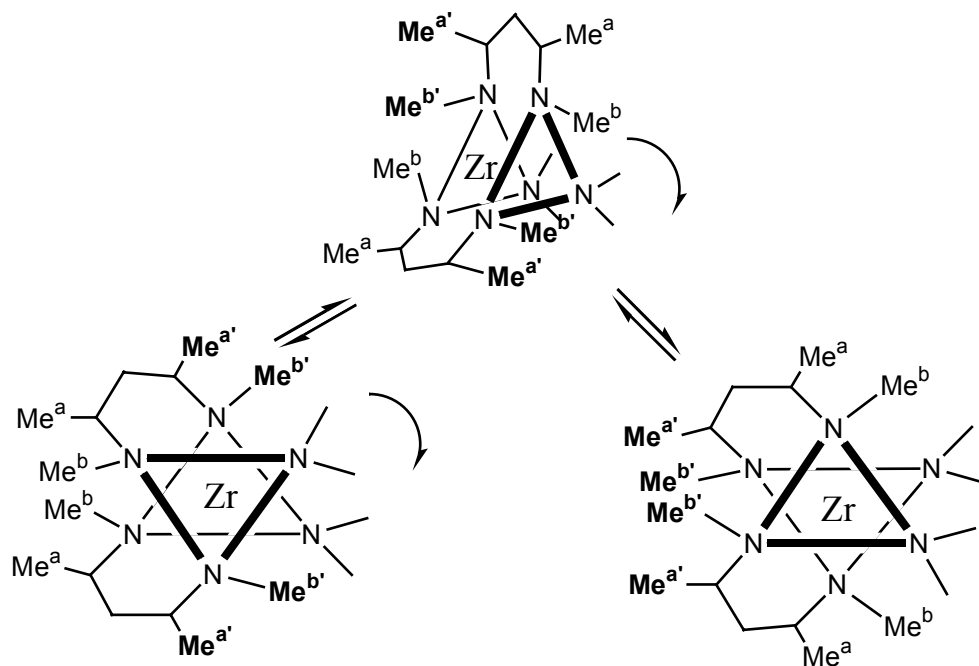
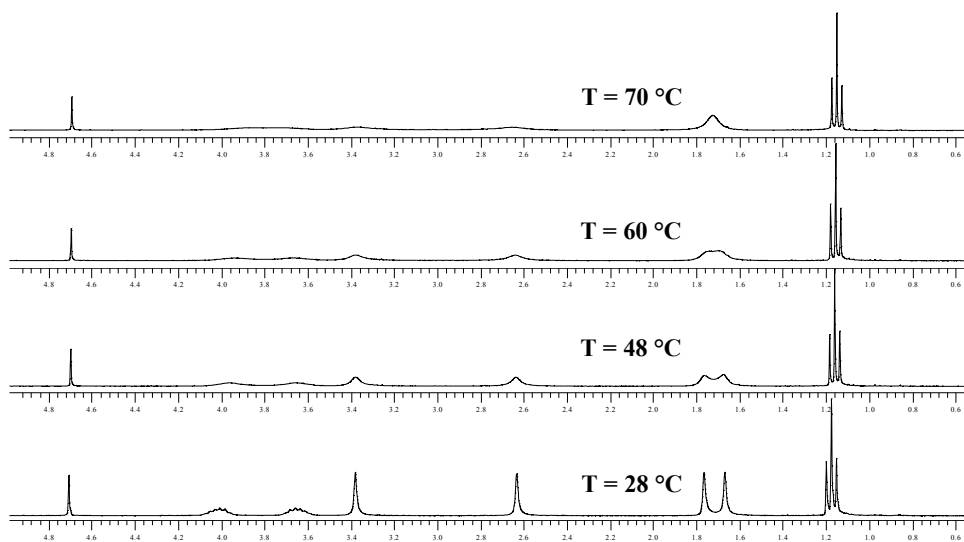


Figure 4.11. Description of the Bailar-twist mechanism for compound 1.



**Figure 4.12.** Variable temperature  $^1\text{H-NMR}$  of complex **2** in  $\text{CD}_2\text{Cl}_2$ .

On the other hand, at room temperature the spectrum of compound **2** (Figure 4.12) displays two sets of multiplets for the two chemically inequivalent methylene signals (4.01 and 3.66 ppm), two signals for the methyl-imido protons (3.38 and 2.63 ppm) and for the ring methyls (1.77 and 1.67 ppm). No exchange has been observed for the methyl protons of the ethyl groups, which appear as a unique triplet centered at 1.18 ppm. In this case, the higher steric demand of the ethyl groups further hinders the equilibration of the two enantiomers. By increasing the temperature coalescence in a single broad peak of the two ring methyls resonances can be observed at 70°C. A full line-shape analysis of the exchanging signals of compounds **1** and **2** has been performed in order to determine the rate constant for the site exchange process. By means of an Eyring plot (see below) the values of the activation parameters were determined:

$$\ln\left(\frac{k_r}{T}\right) = \frac{\Delta H^\ddagger}{RT} + \frac{\Delta S^\ddagger}{RT} + \ln\frac{k}{h}$$



In the formula  $h$  is the Planck constant,  $k$  the Boltzmann constant,  $k_r$  is the rate of interconversion determined by curve fitting of the NMR signals,  $R$  is the gas constant,  $T$  is the temperature expressed in Kelvin and  $\Delta H^\ddagger$  and  $\Delta S^\ddagger$  are activation parameters. The values of  $\Delta H^\ddagger$  for compounds **1** and **2** are  $10.9 \pm 0.6$  and  $19.5 \pm 0.5$  kcal mol<sup>-1</sup>, respectively. For compound **2** the higher activation barrier could be attributed to the higher steric demand of the ethyl groups. These values are in the same range of those obtained by Collins and co-workers and by Smith and co-workers.<sup>[1, 2]</sup> The  $\Delta S^\ddagger$  values are  $-10 \pm 2$  and  $8 \pm 1$  cal mol<sup>-1</sup>K<sup>-1</sup> for compounds **1** and **2** respectively: the first negative value is in agreement with a transition state of higher symmetry that is assumed in the Bailar twist mechanism. The positive value obtained for compound **2** could be explained by an increased steric hindrance affecting the transition-state dynamics.

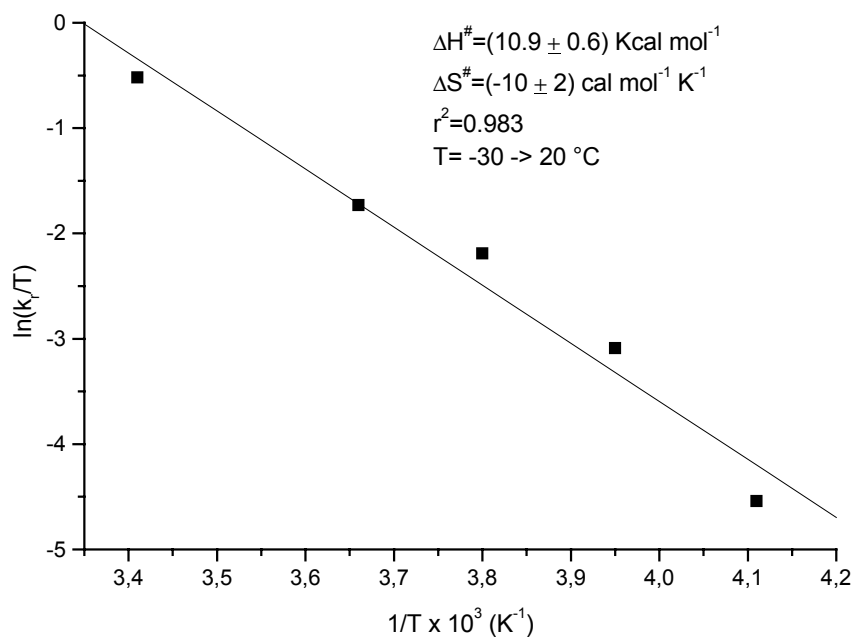


Figure 4.13. Eyring plot for the interconversion of the two enantiomers of compound **1**

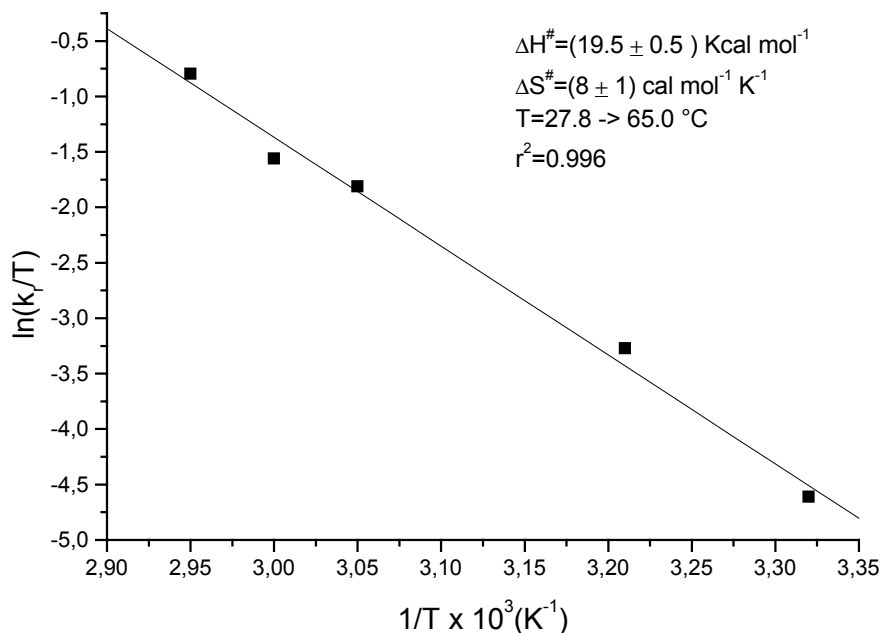


Figure 4.14. Eyring plot for the interconversion of the two enantiomers of compound 2

#### 4.2.2 Compound 3, 4, 5.

The proton and carbon NMR spectra of these compounds do not present any remarkable features. The proton NMR of the  $\beta$ -ketoiminato-based compound **3** reveals the presence of only one of the possible isomers but these data alone did not allow the exact structure of **3** to be established.

The  $^1\text{H}$  NMR of **4** shows a single sharp resonance at 3.08 ppm for the three chemically equivalent dialkylamido groups: on cooling to  $-80^\circ\text{C}$  in  $\text{CD}_2\text{Cl}_2$  the NMR spectrum shows no splitting in any of the resonances. Compound **5** also displays three chemically equivalent NMeEt groups: the Et group gives a triplet at 1.19 ppm for the  $\text{CH}_3$  and a quartet at 3.35 for the  $\text{CH}_2$ , while the Me is the singlet at 3.03 ppm. Also, this compound does not display any splitting in the temperature range from  $-80^\circ\text{C}$  to  $25^\circ\text{C}$ . The X-ray crystal structure of compounds of the type  $\text{LZr}(\text{NMe}_2)_3$  (where L is a N-aryl-substituted  $\beta$ -diketiminato ligand) have been reported by Smith and co-

workers.<sup>[2]</sup> In the solid state it shows that the three dialkylamido ligands are not equivalent. It appears that the equivalency on the NMR time scale is due to fluxional processes in solution.

#### 4.2.3 Compounds **6**, **7**, **10**,**11**.

All these eight-coordinate compounds have very simple NMR spectra, due to a highly symmetric coordination environment around the metal center. Compound **6** has slightly broadened singlets at 1.80 ppm (methyl of the ring), 4.60 ppm (methyne) and 6.79 ppm (NH); the latter signal is much sharper and evidently shifted up-field compared to the signal of the free protonated  $\beta$ -diketimine ligand: for instance, all the H-substituted  $\beta$ -ketoimines and  $\beta$ -diketimines always display the three protons on the nitrogen atom as one very broad signal in the range of 10-12 ppm. Compound **7**, despite the possibility of existence of several isomers, has a very simple proton NMR spectra, with sharp singlets assigned to the two proton methyls (2.06 and 1.53 ppm), a singlet for the ring methyne (4.91 ppm) and a singlet for the coordinated NH (7.78 ppm). Compound **10** displays only three singlets at 6.99, 4.98 and 1.22 ppm, assigned to the NH, CH and <sup>t</sup>Bu, respectively. Compound **11** displays four singlets: two broad resonances at 1.10 and 1.37 are assigned to the <sup>t</sup>Bu groups, the methyne proton is found at 5.34 ppm, and the NH signal falls at 8.10 ppm.

### 4.3 X-ray Crystallographic Studies of $\beta$ -diketiminato-based Compounds

#### 4.3.1 Structure of $\text{Zr}(\text{MeNacNac})_2(\text{NMe}_2)_2$ and $\text{Zr}(\text{MeNacNac})_2(\text{NEt}_2)_2$ (**1** and **2**).

The structures of both compounds **1** and **2** have been determined by single-crystal X-ray diffraction. The two ORTEP drawings and selected bond lengths and angles are displayed in Figure 4.15 and 4.16 and in Table 1.

The dialkylamido ligands are *cis* to each other and both compounds are arranged in a distorted octahedral geometry. All structural characteristics are very similar for these two compounds. The C-N-C atoms of the dialkylamido groups and the Zr atom are in the same plane. Due to the *trans* influence of the amido ligand, the two different Zr-N bonds of the  $\beta$ -diketiminato ligand differ by approximately 0.1 Å, depending if they are *trans* or *cis* to the amide. The zirconium atom lies in both cases slightly above the plane formed by the  $\beta$ -diketiminato ligands (on the average 0.8 Å for both **1** and **2**).

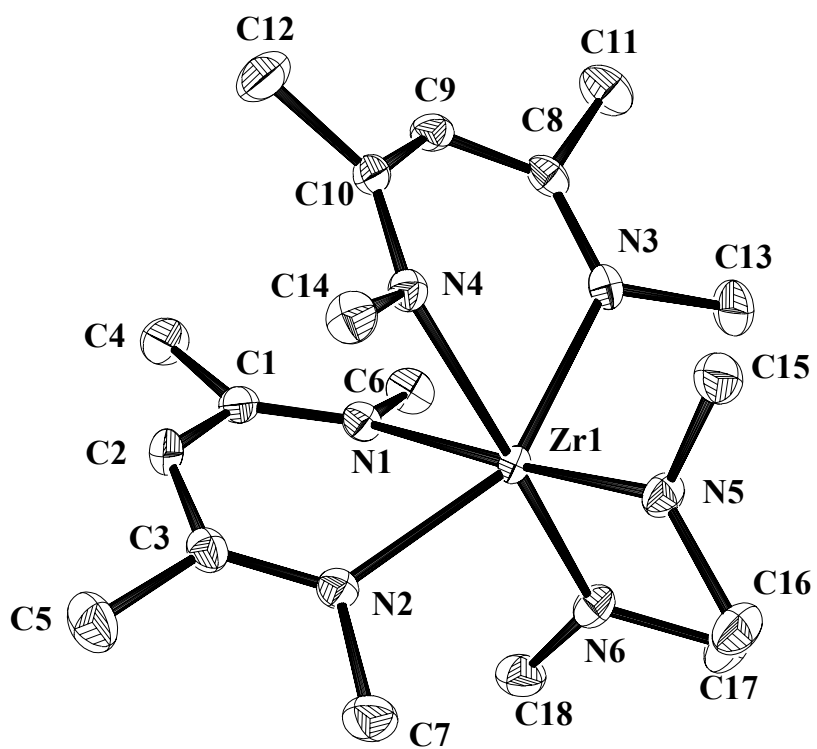


**Figure 4.15.** X-ray single crystal structure of compound 1. Displacement ellipsoids are shown with a 50% probability level. H-atoms are omitted for clarity.

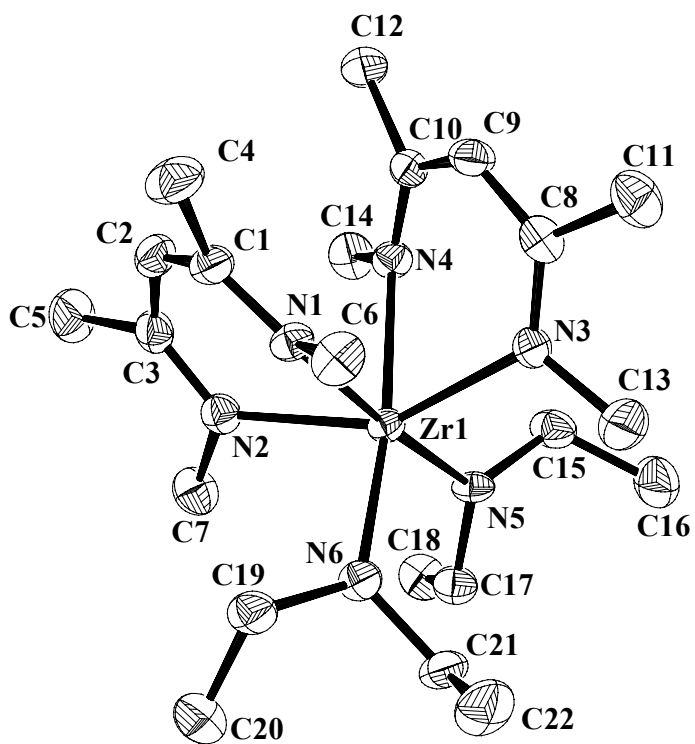


Figure 4.16. X-ray single crystal structure of compound 2. Displacement ellipsoids are shown with a 50% probability level. H-atoms are omitted for clarity.

**Table 1: Selected bond lengths (Å) and angles (deg) for compounds 1 and 2**

	<b>1</b>	<b>2</b>
Zr1-N6	2.0966(14)	2.109(3)
Zr1-N5	2.1078(13)	2.124(3)
Zr1-N3	2.2295(14)	2.236(3)
Zr1-N2	2.2284(13)	2.225(3)
Zr1-N4	2.3071(13)	2.306(3)
Zr1-N1	2.3119(13)	2.309(3)
N6-Zr1-N5	93.97(5)	94.77(11)
N2-Zr1-N1	77.55(5)	77.68(10)
N3-Zr1-N4	77.90(5)	77.39(10)
N3-Zr1-N2	153.82(5)	149.81(10)
N5-Zr1-N1	175.20(5)	175.92(10)
N2-Zr1-N1	77.55(5)	77.68(10)

#### 4.3.2 Structure of Zr(MeNacac)<sub>2</sub>(NEt<sub>2</sub>)<sub>2</sub> (**3**).

As already mentioned, the proton NMR reveals the presence of only one of the possible isomers for this compound, and these data alone did not allow the exact structure of **3** to be established. This was achieved by a single-crystal X-ray diffraction study (see Figure 4.17 and Table 2 for relevant distances and angles). The coordination geometry is a significantly distorted octahedron. The two  $\beta$ -ketoiminato ligands are arranged in a way such that the two oxygens are *trans* to each other and the two nitrogen atoms are located *cis* to each other. This finding is in agreement with the observation that as the steric demand of the imido nitrogen substituent increase, this kind of arrangement becomes favored for the bidentate  $\beta$ -ketoiminato moiety.<sup>[2]</sup> Also in this case the metal atom lies slightly above the plane formed by the bidentate ligand, with values of dihedral angles being for example Zr-O1-C1-C2 = -20.7(3) and Zr-N1-C3-C2 = 7.0(2).

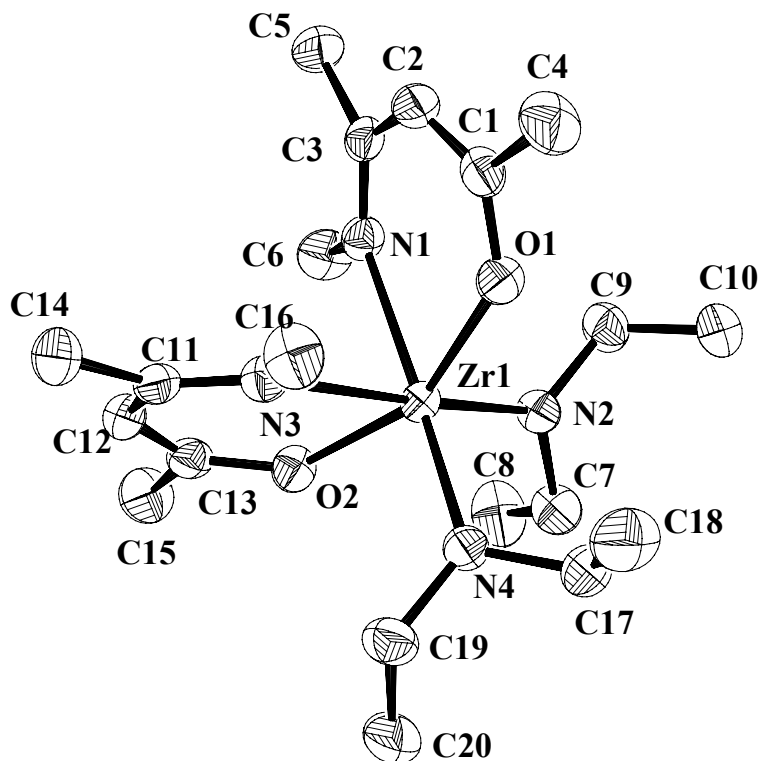


Figure 4.17. X-ray single crystal structure of compound 3. Displacement ellipsoids are shown with a 50% probability level. H-atoms are omitted for clarity.



**Table 2: selected distances (Å) and angles (deg) for compound 3**

Bond lengths (Å)	
Zr1-O1	2.0658(11)
Zr1-N2	2.0698(13)
Zr1-N1	2.3896(13)
C1-C2	1.357(3)
C2-C3	1.440(2)

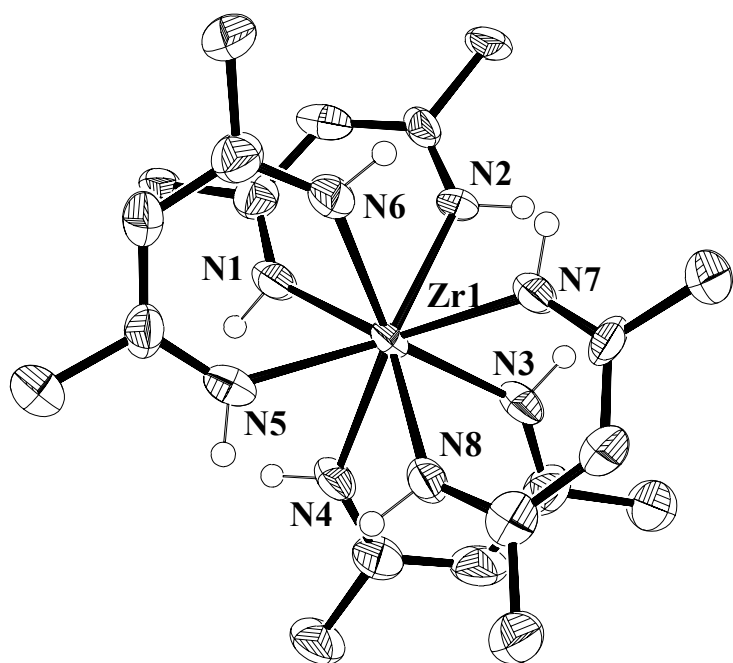
  

Bond Angles (deg)	
O1-Zr1-N2	95.90(5)
O1-Zr1-N1	77.52(5)
N2-Zr1-N1	88.71(5)

#### 4.3.3 Structure of Zr(NacNac)<sub>4</sub> (**6**) and Zr(Nthd)<sub>4</sub> (**10**).

Single crystals suitable for X-ray diffraction were grown from pentane solution for compound **6**. It turns out to be isostructural with Zr(acac)<sub>4</sub> (acac = acetylacetonato), which has been previously studied by X-ray diffraction.<sup>[13, 14]</sup> Another related molecule is the eight-coordinate sandwich-like zirconium tetraazamacrocyclic compound prepared by Jordan and co-workers,<sup>[15]</sup> for which no single crystal structural analysis was reported. The ORTEP drawing of compound **6** is presented in Figure 4.18 along with selected bond lengths and angles given in Table 3. The coordination geometry is square antiprismatic, with each of the Zr-N-C-C-C-N rings displaying two different

sets of Zr-N distances: a short one falling in the range between 2.276-2.285 Å and a longer one spanning the range of 2.301 and 2.331 Å. Once again the zirconium atom is slightly displaced from the plane formed by the N-C-C-C-N ring.



**Figure 4.18.** X-ray single crystal structure of compound 6. Displacement ellipsoids are shown with a 50% probability level. H-atoms bound to carbon are omitted for clarity. Only N-atoms and Zr are labeled for clarity.

**Table 3: selected distances (Å) and angles (deg) for compound 6**

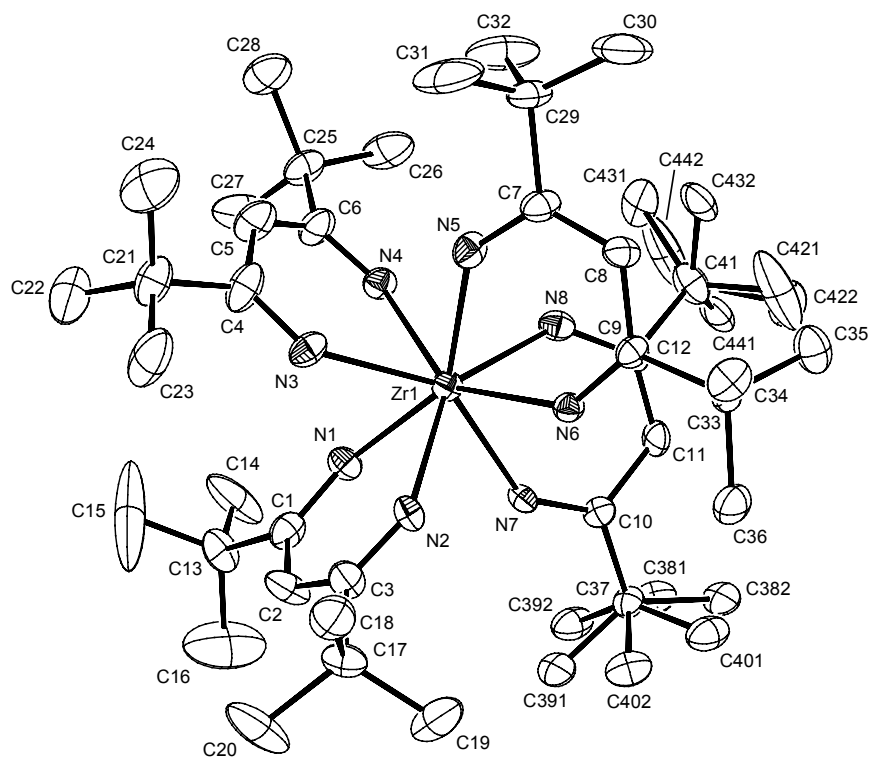
Bond lengths (Å)	
Zr1-N1	2.276(5)
Zr1-N8	2.277(5)
Zr1-N6	2.281(5)
Zr1-N3	2.285(5)
Zr1-N2	2.301(4)
Zr1-N7	2.304(5)
Zr1-N5	2.318(5)
Zr1-N4	2.332(5)

Bond Angles (deg)	
N6-Zr1-N5	72.22(19)
N1-Zr1-N2	72.34(18)
N8-Zr1-N7	72.17(17)
N3-Zr1-N4	71.84(18)
N8-Zr1-N4	75.12(18)
N3-Zr1-N7	76.43(18)
N1-Zr1-N5	76.21(18)
N6-Zr1-N2	75.75(18)
N1-Zr1-N3	110.05(19)
N2-Zr1-N4	121.78(18)

Single crystals of compound **10** were grown from a pentane solution. The structure presents some disorder in the *t*Bu groups. The ORTEP drawing is depicted in Figure 4.18. The coordination geometry is the same as in the case of compound **7** and the

bond angles and distances are comparable as well, thus these details are available in the experimental part (Chapter 6).



**Figure 4. 18.** X-ray single crystal structure of compound 10. Displacement ellipsoids are shown with a 50% probability level. Disorder is present in some of the <sup>t</sup>Bu groups.

## 4.4 Guanidinato-based compounds.

### 4.4.1 Six-coordinate compounds.

The guanidinate ligand can be introduced in several ways onto a zirconium metal center (see Chapter 3), but if we want to obtain mixed bis(guanidinato)bis(alkylamido)zirconium compounds, the most convenient method is the reaction between a carbodiimide and  $Zr(NR_2)_4$ . Isopropyl- and trimethylsilyl-substituted carbodiimides are commercially available and relatively inexpensive. The first complexes that were targeted, were the analogues of the bis( $\beta$ -diketiminato)bis(alkylamido)zirconium compounds **1** and **2**. As shown in Figure 4.19, the reaction of two equivalents of diisopropylcarbodiimide with one equivalent of  $Zr(NR_2)_4$ , affords compounds **12** and **13** in high yields (98 and 78 %, respectively).

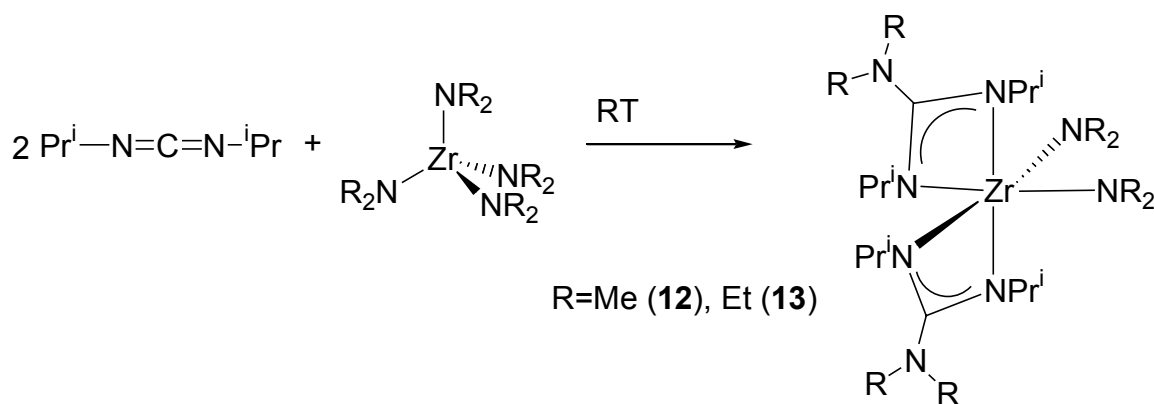


Figure 4. 19. Synthesis of guanidinato-based six-coordinate compounds.

The reaction proceeds smoothly at room temperature to yield the white-crystalline compounds, which are highly soluble in pentane, toluene, ether and dichlorometane. Surprisingly, despite the large steric bulk of the incoming ligand, the reaction

proceeds easily also in the case of compound **13**, while in contrast amide metathesis in the case of  $\text{Zr}(\text{NEt}_2)_4$  was very slow and required high temperatures (paragraph 4.1.1). This might be a hint that electronic factors are also involved in the formation of these compounds.

We also attempted to use a  $\text{SiMe}_3$ -substituted carbodiimide but probably due to the steric bulk of this ligand only five-coordinate compounds were obtained (see next paragraph).

#### 4.4.2 Five-coordinate compounds.

A first attempt to obtain five-coordinate compounds by simply changing the stoichiometry of the reaction shown in Figure 4.19 resulted in a low selectivity. The reaction of one equivalent of isopropylcarbodiimide with  $\text{Zr}(\text{NMe}_2)_4$  gave a mixture of compound **12** and the five coordinate compound  $\text{Zr}(\text{}^i\text{Pr-guanidinato})(\text{NMe}_2)_3$ . We also used the slightly more hindered  $\text{Zr}(\text{NMeEt})_4$  with isopropylcarbodiimide in a 1:1 ratio, in an attempt to obtain the five-coordinate compound  $\text{Zr}(\text{}^i\text{Pr-guanidinato})(\text{NMeEt})_3$ . The NMR analysis of the crude reaction mixture clearly showed that the desired compound was present together with the starting materials, with a conversion lower than 50 %. Warming up the mixture to 90 °C in toluene did not improve the conversion. An attempt to separate these substances by fractional distillation failed, because at around 120 °C, at 0.1 mbar, the mixture started to change its color to brown, probably due to thermal decomposition of the desired five-coordinate product.

Using two equivalents of bis-trimethylsilylcarbodiimide as an entering group to obtain a six-coordinate compound, gave only a five coordinate species as mentioned previously. Warming the reaction mixture to 90 °C in toluene for 2 days gave only an unidentified polymeric product.

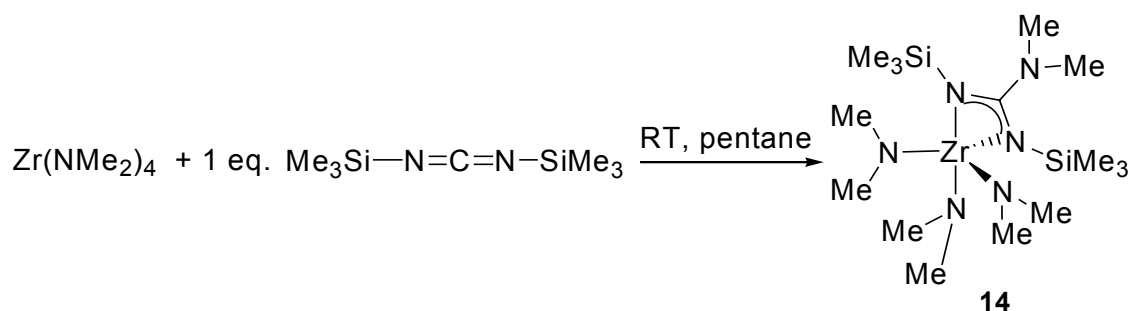


**Figure 4.20. Synthesis of five-coordinate guanidinato-based complexes.**

By reaction of one equivalent of bis-trimethylsilylcarbodiimide and  $\text{Zr}(\text{NMe}_2)_4$  it was possible to obtain the compound shown in Figure 4.20 (compound **14**) in quantitative yield. In this case it seems that the steric requirements of both the entering group and the metal complex, are well optimised to allow the desired stoichiometric control to be obtained.

#### 4.4.3 Attempts to obtain imido-bound complexes.

On a purely speculative basis, a thermally induced CVD reaction to obtain MN starting from a molecular precursor could go through the reaction displayed in Figure 4.21. If we were be able to synthesize a molecule with a very strong metal-nitrogen multiple bond, this would be retained during the deposition process, giving a solid film with a 1:1 stoichiometry between the metal and nitrogen.

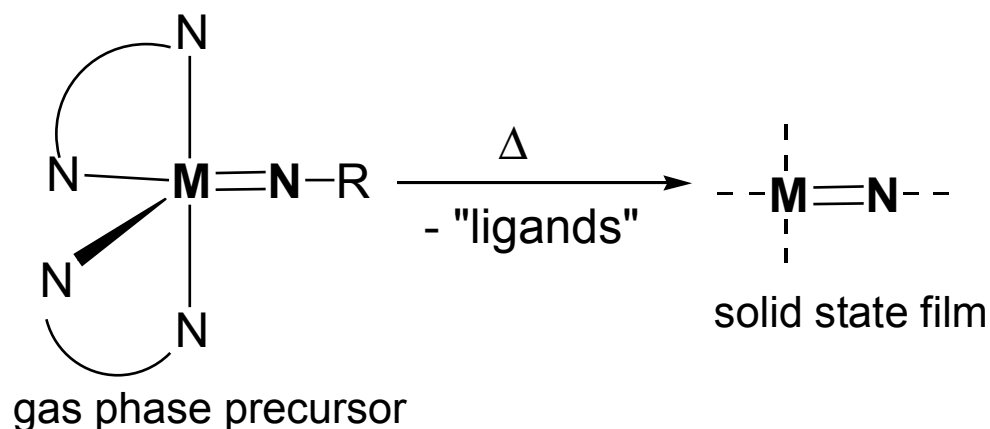


**Figure 4.21. Idealized decomposition reaction for an imido-substituted precursor**

This design strategy led us to investigate the possibility of having precursors containing a multiple metal-nitrogen bond, i.e. to produce an *imido* functionality. The typical route to obtain imido functionalities is the reaction between a dimethylzirconium compound with an amine as described by the group of Bergman<sup>[16]</sup>, as depicted in Figure 4.22.

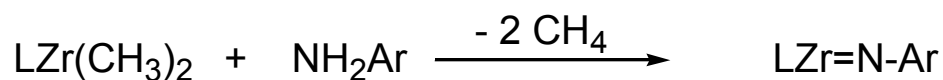


**Figure 4.22. Example of synthesis of imidozirconium compounds by reaction of a dimethylzirconium complex with an arylamine (ref. 16).**



Recently a paper by the group of Richeson<sup>[17]</sup> described the preparation of arylimido guanidinato-supported compounds starting from a dialkylzirconium complex by reaction with an arylisocyanide (Figure 4.23).



Figure 4.23. Recent example of synthesis of imidozirconium compounds by reaction of a dialkylzirconium complex with an arylisocyanide (ref. 17).

Although this method could work well also in our case, it would involve the preparation of a dialkylzirconium compound, adding further synthetic steps; therefore we decided to explore another route. Having the possibility to prepare large amounts of guanidinato-substituted compound such as **12**, we warmed it up in the presence of <sup>t</sup>BuNH<sub>2</sub>, hoping to obtain the elimination of HNMe<sub>2</sub> as displayed in Figure 4.24.

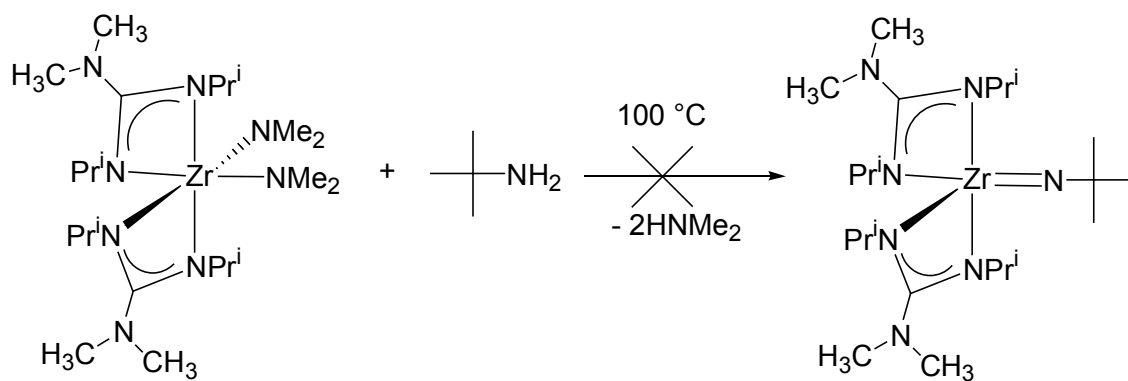


Figure 4.24. Attempt to obtain imido compounds by amide elimination

The reaction failed to work even using the amine as reaction solvent and warming the mixture to 100 °C in an autoclave, and therefore we tried another approach. We had available some *t*-butylamido-bridged compound  $(^t\text{BuNH})_2(\mu\text{-N}^t\text{Bu})_2\text{Zr}_2$ , which is formally a dimer of an imido substituted compound. We expected that, upon entrance of the guanidinato ligands with their steric bulk, and by warming the reaction mixture, we would have been able to break the bridge and obtain the desired monomeric imidozirconium compound. The reaction of this dimer with four equivalents of isopropylcarbodiimide at room temperature did not yield the desired compound (Figure 4.25). Instead, only one of the metallic center of the bridge underwent an insertion reaction. Not only the strong double bridge between the units cannot be broken, but also an unexpected reactivity for each metal center is observed. Apparently, after one of the imido ligands is inserted, the other metallic center becomes deactivated, and the subsequent equivalent of carbodiimide inserts more easily into the just-formed five-coordinate metal center, to give a six-coordinated metal. Neither an excess of carbodiimide (five equivalents) nor warming up the reaction mixture affects this kind of reactivity. The only molecule with similar characteristics to compound **15**, was reported by Mountford and co-workers.<sup>[18]</sup> In this case, instead of the guanidinato ligands, one of the metal centers is coordinated by a tetraazamacrocyclic ligand. Also in this case, the complex displayed the reduced reactivity of the four-coordinate metal center. This phenomenon seems quite interesting from the point of view of the chemistry, but the resulting in compounds are not suitable for our purpose, since dimeric compounds are often not enough volatile. We have therefore decided not to investigate this chemistry any further, since it is outside the scope of this thesis.

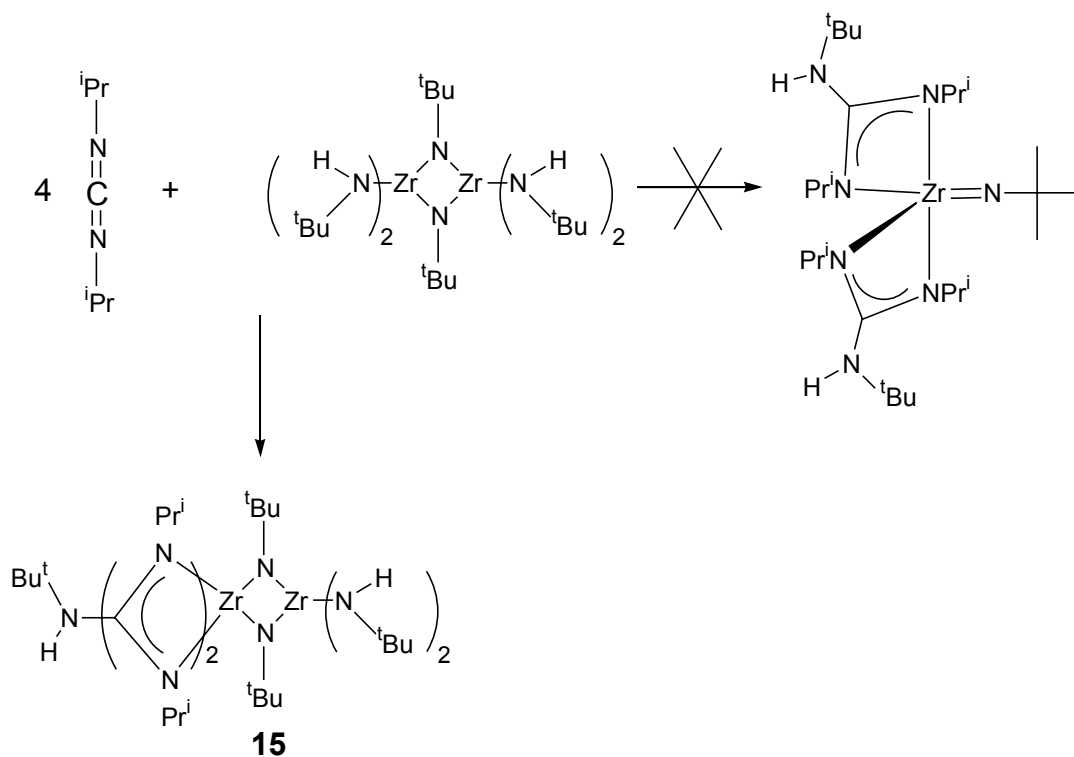


Figure 4.25. Reactivity of amido-bridged zirconium complexes towards carbodiimides

## 4.5 NMR of guanidinato-based compounds.

### 4.5.1 Six-coordinate compounds.

The NMR spectra of compound **12** (Figure 4.25), does not display any remarkable features. The resonance of the dimethylamido group falls at 3.32 ppm, whereas the singlet at 2.52 ppm is assigned to the methylamido group on the guanidinato ligand. The isopropyl groups give a simple pattern, with a doublet at 1.27 ppm (methyl) and a septet at 3.63 ppm (methyne). On the other hand, the  $^1\text{H}$ -NMR spectrum of compound **13** (Figure 4.26) is more complicated. The triplet centered at 0.94 ppm (labelled with *a*,  $J = 7.2$  Hz) can be assigned to the methyl group of the  $\text{NEt}_2$  bound to

the zirconium atom. The CH<sub>2</sub> group coupled to this CH<sub>3</sub> is assigned to one of the of multiplets found at 3.73, 3.55 and around 3.0: there are at least 4 multiplets (*b*, *b'*, *c*, *c'*) among this signals, belonging not only to the NEt<sub>2</sub> bound to zirconium, but also to the NEt<sub>2</sub> bound to the guanidinato moiety. The two NEt<sub>2</sub> of the two guanidinato ligands and the two NEt<sub>2</sub> bound to the zirconium atom, are both enantiotopic, so they display CH<sub>2</sub> signals in different chemical environments, as already observed for compound **2**. There is another triplet at 1.19 ppm (*d*), which is the methyl group of the NCH<sub>2</sub>CH<sub>3</sub> of the guanidinato ligand. The CH groups of the <sup>i</sup>Pr groups give rise to at least 4 doublets (1.26, 1.32, 1.44, 1.48 ppm). This is evidently due to the steric interaction between the diethylamido group and the guanidinato ligands, which even in solution forces the molecule into a distorted geometry, in which the isopropyl groups and the diethylamido groups are not equivalent on the NMR timescale. Indeed the identity of the desired structure was also confirmed by X-ray diffraction (see next section), elemental analysis and mass spectrometry.

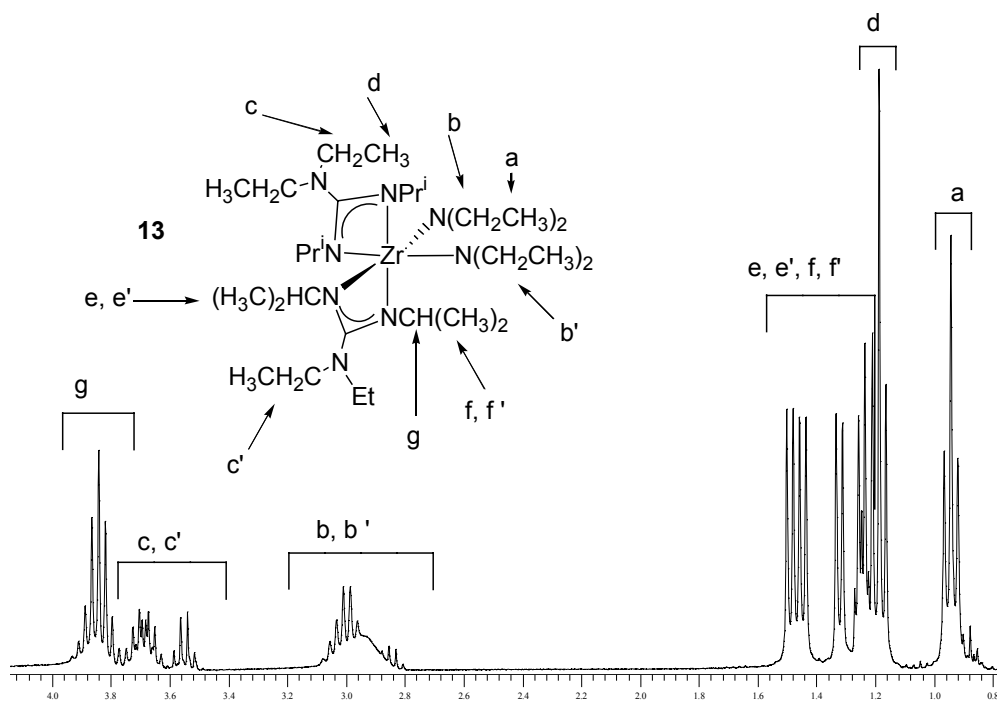
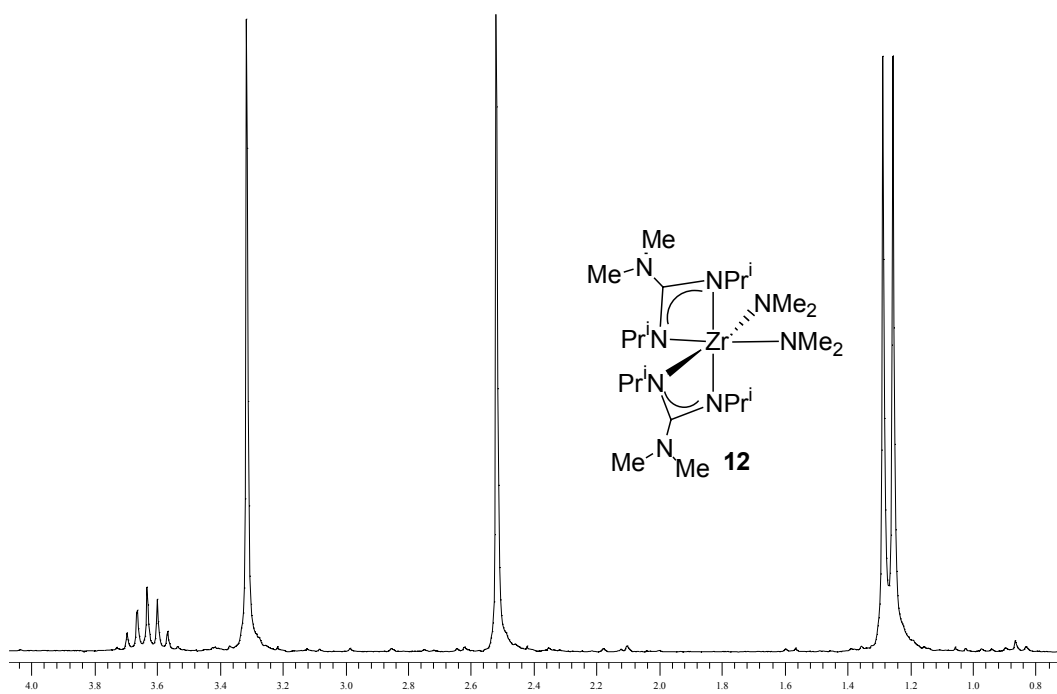


Figure 4.26. Proton NMR of six-coordinate guanidinato-based compounds 12 and 13.

#### 4.5.2 Five-coordinate compounds.

As discussed in section 4.2.2, the compounds  $\text{Zr}(\text{}^i\text{Pguanidinato})(\text{NMeEt})_3$  and  $\text{Zr}(\text{SiMe}_3\text{guanidinato})(\text{NMeEt})_3$  were detected by proton NMR but it was not possible to isolate them in a pure form. The proton spectra of the five-coordinate, guanidinato-supported complexes display some common features and the assignment is quite easy, therefore it will be only briefly discussed. As already observed in the case of the related  $\beta$ -diketiminato complexes, the three dialkylamido ligands are chemically equivalent and give only one NMR signal. The compound  $(\text{}^i\text{Pguanidinato})\text{Zr}(\text{NMeEt})_3$  displays a doublet assignable to the  $\text{CH}_3$  of the isopropyl group at 1.14 ppm; the related  $\text{CH}_3$  is partially masked by the quartet assigned to the  $\text{CH}_2$  of the  $\text{NMe}(\text{CH}_2\text{CH}_3)$  moiety. The latter resonance falls at 3.35 ppm. The CH multiplet falls slightly downfield (about 3.5 ppm). Compound  $(\text{SiMe}_3\text{guanidinato})\text{Zr}(\text{NMeEt})_3$  has two sets of signals for the diethylamido group: the ones belonging to the guanidinato ligand are a triplet at 1.16 ppm and a quartet at 3.24 ppm, the ones belonging to the monodentate ligand are at 1.24 ppm (triplet) and 3.37 ppm (quartet); the  $\text{SiMe}_3$  moiety gives a singlet at 0.27 ppm.

#### 4.5.3 Compound 15.

The proton and carbon NMR spectra of compound **15** clearly show the occurrence of this binuclear complex. In Figure 4.27 only the  $^1\text{H}$ -NMR is shown, with the relative assignments. Three distinct singlets are found for the three different  $^t$ butyl groups (a, b and c): the bridging one (1.25 ppm), the one from the guanidinato moiety (1.50 ppm) and the one bound to the four-coordinate center (1.64). The isopropyl groups of the guanidinato ligand are in a chemically different environment as already observed for compound **13**: the  $\text{CH}_3$  group gives four distinct doublets at 1.81, 1.55, 1.34, 1.26,

labeled as e, e', f, f'. The CH gives two distinct multiplets d and d' at 3.68 and 3.96 ppm. Apparently there is structural inequivalence not only among the two guanidinate ligands bound to Zr, but also among the two isopropyl groups belonging to each guanidinato ligand, probably because of hindered rotation due to intramolecular steric interactions.

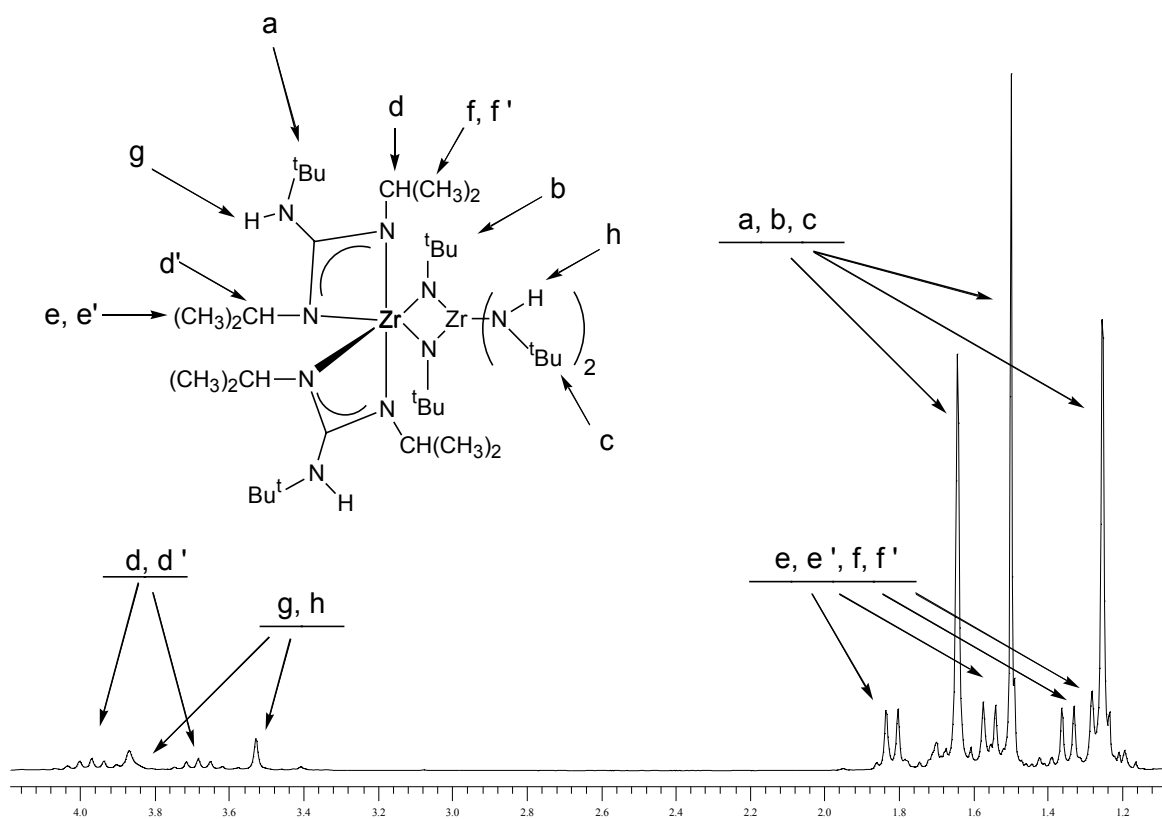


Figure 4.27. Proton NMR of the binuclear compound 15.

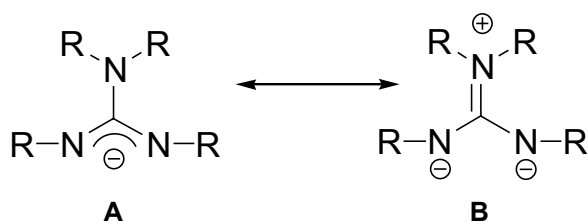
## 4.6 Single-crystal X-ray diffraction studies of guanidinato supported precursors

It was possible to grow single crystals of compound **12**, **13** from pentane solutions, at  $-35\text{ }^{\circ}\text{C}$ . For compound **16**, single crystals suitable for X-ray diffraction were obtained from toluene at  $-35\text{ }^{\circ}\text{C}$ .

Compound **12** and **13** are structurally related to each other, and their ORTEP drawings are shown in Figures 4.28 and 4.29. Compound **13** presents some disorder in all diethylamido groups due to rotation in the solid state. The coordination geometry around the zirconium atom is a distorted octahedron. In both compounds the dialkylamido ligands adopt a *cis* configuration. Selected bond lengths and angles are reported in Tables 4 and 5. The Zr-N distances in the dialkylamido group are shorter than the Zr-N distances in the guanidinato ligand for both compounds (see tables). A structural feature already discussed in the case of the  $\beta$ -diketiminato-substituted analogues, is found also for compound **12** and **13**. For instance, in compound **12**, the *trans* influence arising from the dimethylamido group, makes the Zr(1)-N(1) distance slightly longer than the Zr(1)-N(2) distance (2.320(2) Å against 2.235(2) Å, respectively). The same trend is observed for the Zr(1)-N(4) and Zr(1)-N(5) bonds, where the distances are 2.343(2) and 2.221(2) Å, respectively. Similar behavior is also found for compound **13**, where one can observe two groups of distances for the Zr-N bonds in the guanidinato ligands: the longer ones (Zr(2)-N(14) = 2.360(5) Å, and Zr(2)-N(12) = 2.344(5) Å) for the bonds *trans* to the diethylamido group, and the shorter ones (Zr(2)-N(11) = 2.235(4) Å and Zr(2)-N(15) = 2.252(4) Å) for the bonds *cis* to the diethylamido group. Similar trend in the distances have been already observed for similar compounds.<sup>[19]</sup> The higher distortion in the octahedral coordination geometry for compound **13** has also to be noted: the angle between the two dimethylamido groups is 91.01 for compound **12**, whereas for **13** the corresponding N(10)-Zr(2)-N(9) angle is much larger (98.09). In compound **13**, both angles N(11)-Zr(2)-N(12) and N(15)-Zr(2)-N(14) (57.98 and 58.04, respectively), are slightly smaller



than the corresponding ones in compound **12** (58.24 for N(5)-Zr(1)-N(4) and 58.40(8) for N(2)-Zr(1)-N(1)). In compound **12**, the planar NMe<sub>2</sub> moieties belonging to the guanidinato ligands, are not on the same plane of the four-member cycles Zr1-N1-C1-N2 and Zr1-N4-C2-N5. The dihedral angles formed by the NMe<sub>2</sub> function and the ZrNCN plane are 43.1° and 50.4°, respectively. Similar values are observed for compound **13**. The angles reported in literature for similar compounds with more sterically hindered groups such as NSi(CH<sub>3</sub>)<sub>2</sub>, are close to 90°. The value of this angle can be influenced of course not only by intramolecular interaction but also by solid-state packing effects. Due to this structural arrangement, the contribution of a zwitterionic resonance structure, such as **B** shown below, can be ruled out.



The binuclear compound **15** has two metallic centers displaying a distorted octahedral and a distorted tetrahedral coordination geometry (Figure 4.30). The Zr(1)-Zr(2) distance is 3.13 Å, therefore no metal-to-metal bond is present. The atoms Zr(1)-N(7)-Zr(2)-N(8) are in the same plane. The zirconium-nitrogen distances in this four-member ring are not equivalent, the bonds belonging to the octahedral center being about 0.04 Å longer. As we observed for compound **12** and **13**, the NH<sup>t</sup>Bu groups are not on the same plane of the ZrNCN plane: the dihedral angles are 59.6°, 55.7°, slightly higher than in the previously analyzed guanidinato complexes. The shorter distances for the bridging Zr-N bonds could explain the stability of this structural motif, and the reason why all attempts to break the bridging amido unit were unsuccessful. Also in this case, the *trans* influence of the dialkylamido ligands gives two sets of slightly different bond distances in the guanidinato moieties (*trans* bonds about 0.18 Å longer than the *cis*). As mentioned previously, a similar

tetraazamacrocyclic-substituted complex was described in the literature, and its crystal structure displays all corresponding distances of the Zr(1)-N(7)-Zr(2)-N(8) four-membered ring, shorter than in our case.<sup>[18]</sup>

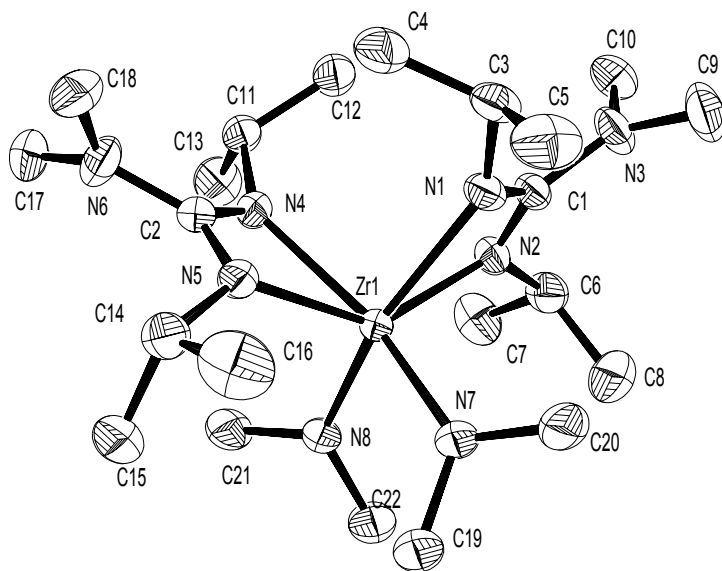


Figure 4.28. Structure of compound 12. Displacement ellipsoids are shown with a 50% probability level. H-atoms are omitted for clarity.

Table 4. Selected bond lengths and angles for compound 11

Bond Lengths (Å)		Bond Angles (deg)	
Zr(1)-N(8)	2.088(2)	N(8)-Zr(1)-N(7)	91.01(10)
Zr(1)-N(7)	2.093(2)	N(5)-Zr(1)-N(4)	58.24(8)
Zr(1)-N(5)	2.221(2)	N(2)-Zr(1)-N(1)	58.40(8)
Zr(1)-N(2)	2.235(2)	N(8)-Zr(1)-N(5)	105.31(9)
Zr(1)-N(1)	2.320(2)	N(8)-Zr(1)-N(2)	101.89(9)
Zr(1)-N(4)	2.343(2)	N(1)-Zr(1)-N(4)	92.28(8)
		N(8)-Zr(1)-N(1)	159.90(9)
		N(7)-Zr(1)-N(4)	160.75(9)
		N(2)-Zr(1)-N(4)	92.25(8)

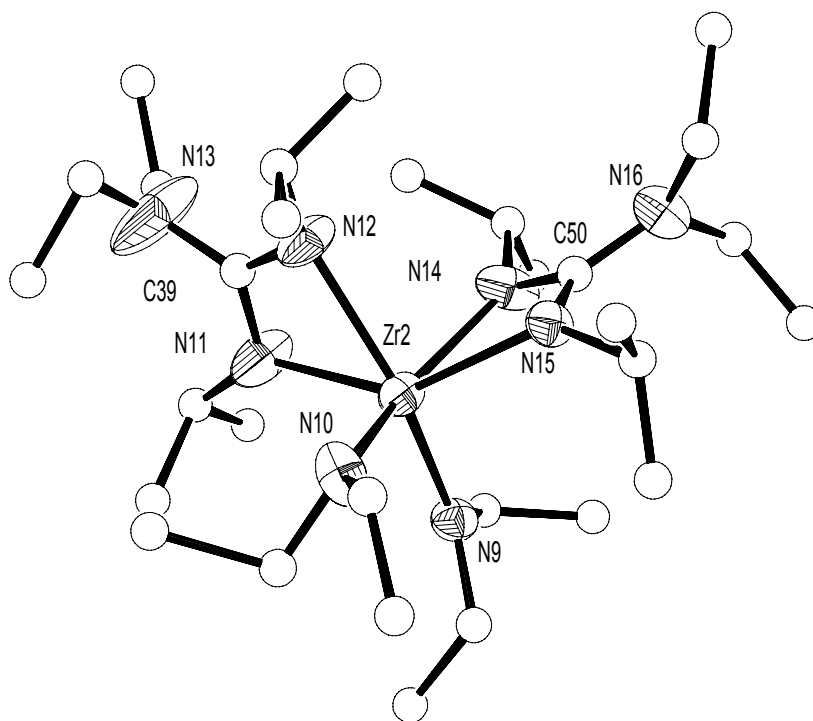


Figure 4.29. Structure of compound 13. Displacement ellipsoids are shown with a 50% probability level. H-atoms are omitted for clarity.

Table 5. Selected bond length and angles for compound 13

Bond Lengths (Å)		Bond Angles (deg)	
Zr(2)-N(9)	2.080(4)	N(9)-Zr(2)-N(10)	98.09(18)
Zr(2)-N(10)	2.083(5)	N(11)-Zr(2)-N(12)	57.98(17)
Zr(2)-N(11)	2.235(4)	N(15)-Zr(2)-N(14)	58.04(14)
Zr(2)-N(15)	2.252(4)	N(10)-Zr(2)-N(11),	102.6(2)
Zr(2)-N(12)	2.344(5)	N(10)-Zr(2)-N(15)	99.37(16)
Zr(2)-N(14)	2.360(5)	N(12)-Zr(2)-N(14)	83.91(19)
		N(10)-Zr(2)-N(14)	157.16(16)
		N(9)-Zr(2)-N(12)	158.09(16)
		N(10)-Zr(2)-N(15)	99.37(16)

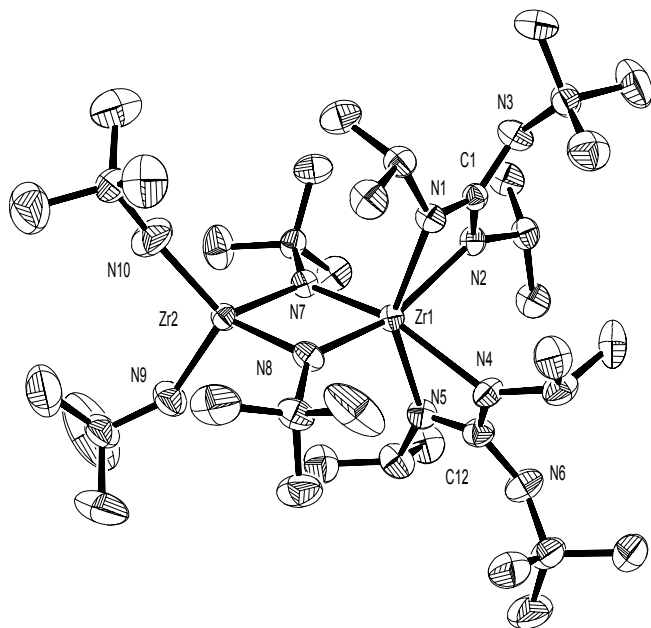


Figure 4.30. Structure of compound 15. Displacement ellipsoids are shown with a 50% probability level. H-atoms are omitted for clarity.

Table 6. Selected bond lengths and angles for compound 15

Bond Lengths (Å)		Bond Angles (deg)	
Zr(1)-N(8)	2.090(2)	N(8)-Zr(1)-N(7)	80.92(9)
Zr(1)-N(7)	2.098(3)	N(1)-Zr(1)-N(2)	58.34(8)
Zr(1)-N(5)	2.241(2)	N(5)-Zr(1)-N(4)	58.06(9)
Zr(1)-N(1)	2.242(2)	N(5)-Zr(1)-N(1)	146.01(9)
Zr(1)-N(2)	2.348(2)	N(7)-Zr(1)-N(1)	104.55(9)
Zr(1)-N(4)	2.353(3)	N(8)-Zr(1)-N(2)	159.21(9)
Zr(2)-N(7)	2.049(2)	N(7)-Zr(2)-N(8)	82.84(9)
Zr(2)-N(8)	2.059(3)	N(10)-Zr2-N(9)	109.39(14)
Zr(2)-N(10)	2.060(3)	Zr(2)-N(7)-Zr(1)	98.11(9)
Zr(2)-N(9)	2.066(3)	Zr(2)-N(8)-Zr(1)	98.06(9)
Zr(1)-Zr(2)	3.1325(5)		

## 4.7 Thermal Properties and Structure-Volatility Correlations.

### 4.7.1 $\beta$ -diketiminato-based compounds.

Both compounds **1** and **2** can be sublimed at a temperature of 125-130°C (oil bath temperature) at 0.1 mbar, which makes them interesting candidates for use as CVD precursors. They are both less volatile than the corresponding isostructural bis(acetylacetonato)bis(alcoholato) compounds.<sup>[20]</sup> The five-coordinate compound **4** is less volatile than the six-coordinate compounds **1** and **2**. It was possible to sublime it at 135°C at a pressure of about  $10^{-4}$  mbar (cold finger temperature of -10 °C). It was attempted to sublime a freshly crystallised batch of **3**, but once a temperature of about 100 °C was reached an evident colour change occurred apparently due to thermal decomposition. The eight-coordinate compound **6** seems to be less volatile than the six-coordinate **1** and **2**. **6** sublimes at 140-145 °C and 0.1 mbar with a reasonable evaporation rate.

The thermal behaviour of compounds **1**, **2**, **4**, **6** and **7** has been also investigated by DSC and TG. Compound **3** has not been taken into consideration due to its thermal instability. The DSC and TG traces of **1** and **2** are quite similar and therefore only those of compound **2** are displayed in Figure 4.31 and 4.32. The DSC shows a single, sharp endothermic peak with a maximum at about 137 °C corresponding to the melting point of the compound: after melting has occurred the compound undergoes partial decomposition with a slight change in color to brown. When the melting point was checked visually using a classical melting point apparatus, the substance seemed to melt and decompose in the range 139-141 °C, thus slightly shifted towards higher temperature compared to the DSC value. In fact, DSC analysis is not considered a reliable tool for determining correctly melting points.

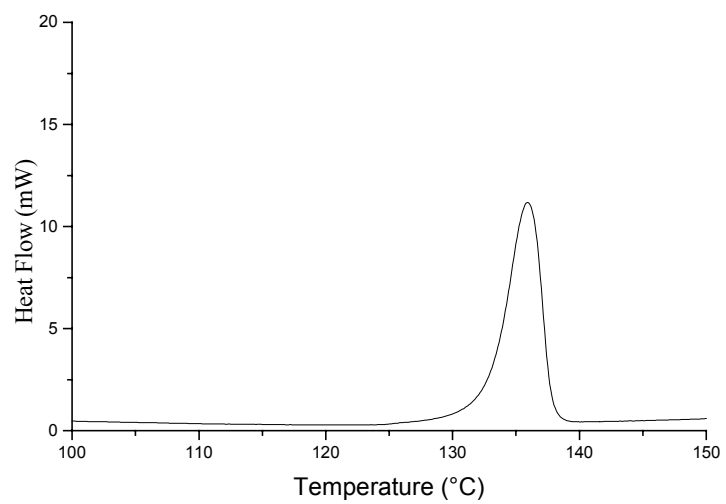


**Figure 4.31 DSC trace for compound 2.**

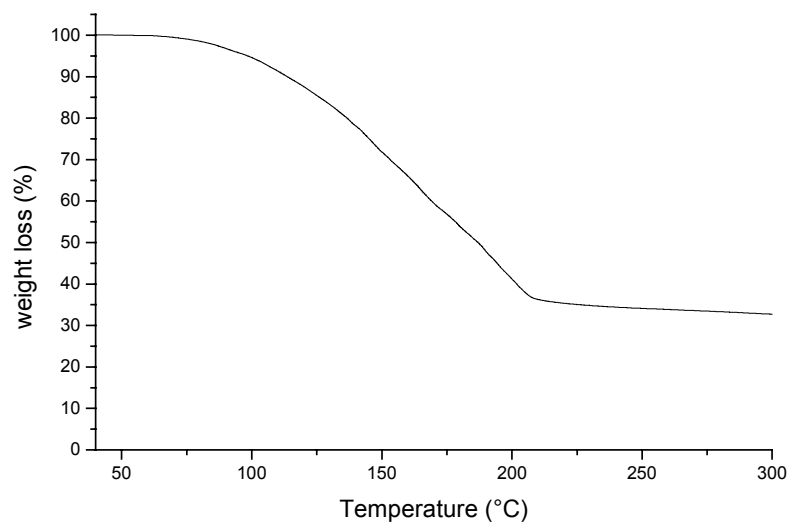


**Figure 4.32 TG trace for compound 2.**

The thermogravimetric curve shows that even around 100 °C the weight loss becomes significant and the curve reaches a plateau when the remaining solid constitutes about 35%. Compound **4** is also thermally much more robust than the above-discussed six-coordinate compounds, but evidently less volatile. The TG trace of compound **4** (not shown), reveals a slow weight loss as a function of temperature between 50 and 350 °C with a residue of about 40% of the initial weight when the plateau is reached. This example demonstrates that there is no simple correlation between the coordination number and the volatility, other factors being involved as the molecular weight (i.e. higher electronic polarizability), dipole moment and packing effects in the solid state. From DSC data of compound **6** (Figure 4.33), it is possible to observe a sharp, endothermic melting peak at around 190 °C. Above this temperature the substance partially decomposes. For compound **7**, a much broader DSC melting peak is found at higher temperature (214 °C, see Figure 4.34), in agreement with the presence of several isomeric structures.

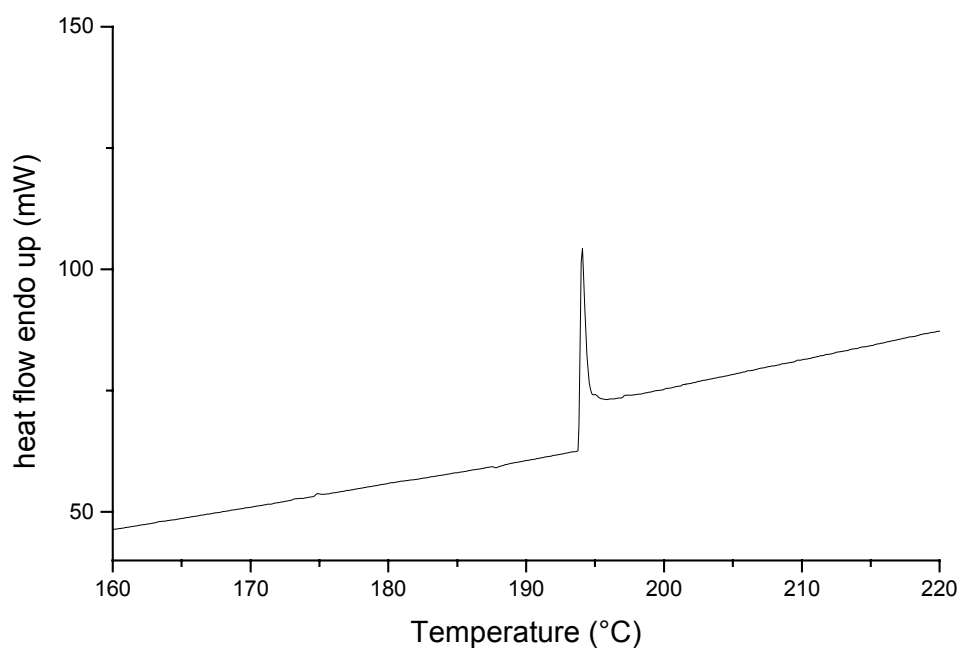




Figure 4.33. DSC melting peak for compound 6.

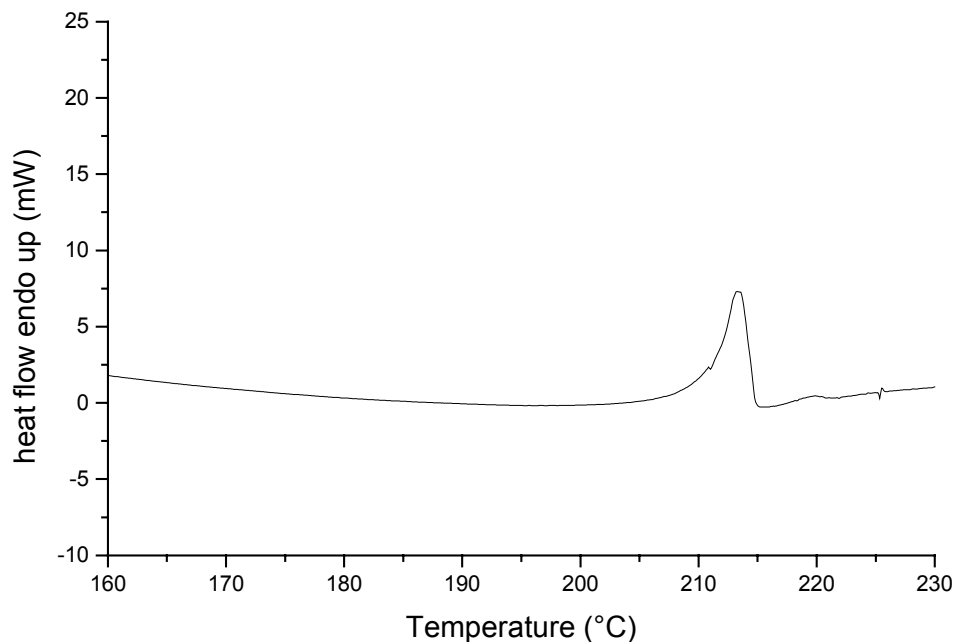
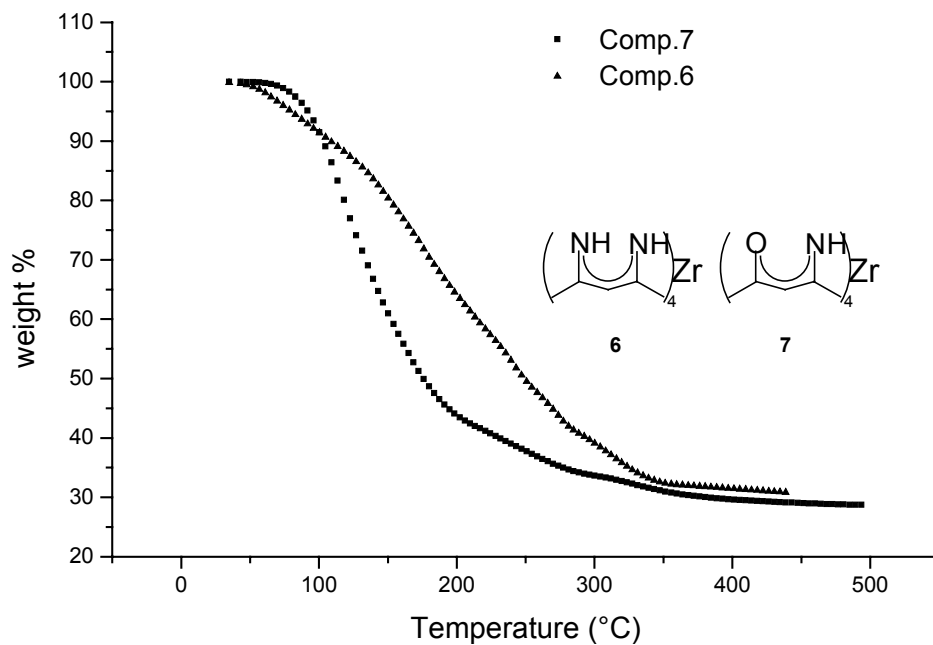


Figure 4.34 DSC melting peak for compound 7.

The TG trace displays a slow weight loss, and the curve reaches a plateau at 300 °C, when about 30 % of the initial weight is left. Complex **7** can be sublimed at 0.1 mbar, 135 °C: it seems to have an increased thermal stability with respect to all the compounds analysed so far: it melts at 212 °C and loses weight more rapidly than the parent eight-coordinate compound **6**. So in this last case we have observed that the  $\beta$ -ketoiminato substituted compound is much more thermally robust than the  $\beta$ -diketiminato, in contrast to what was seen for the six-coordinate compounds. The TG traces of the eight-coordinate compounds **6** and **7** are displayed in Figure 4.35. The low-temperature weight loss observed in the case of compound **6** is likely due to partial loss of the ancillary ligand or degradation of the complex due to the presence

of traces of water in the experimental set-up. Apparently the weight loss as a function of temperature is slightly faster in the case of the  $\beta$ -ketoiminato complex, and its sublimation temperature seems to be slightly lower compared to the parent diketiminato compound **6**. Compound **6** has a dipole moment equal to zero due to its high symmetry, whereas compound **7**, depending on the arrangement of the four bidentate ligand, could display a non-zero dipole moment. For compound **6**, this would of course imply reduced intermolecular forces in the solid state, but this goes against the experimental observation of its higher sublimation temperature. These considerations do not take into account the molecular polarizability of the molecules, which is of course a very important factor when considering intermolecular forces. In general, higher molecular weight (i.e. more electrons) implies higher polarizability: both compounds have approximately the same molecular weight. Nevertheless replacing an oxygen atom with an "NH" might of course give a different group contribution to the total molecular polarizability, but this is difficult to judge on a qualitative basis. Nonetheless it has to be noticed that compound **7** can have more than one isomer. The higher order and the better packing in the solid state due to the symmetry of compound **6**, might explain the slightly higher sublimation point.



**Figure 4.35. Comparison of TG traces of compounds 6 and 7.**

It is interesting to compare the TG curves of the eight-coordinate complex **7** with the corresponding <sup>t</sup>Bu-substituted analogs **11** (Figure 4.36). The presence of the bulky <sup>t</sup>Bu group makes the molecule more thermally stable. The compound sublimes at around 152-156 °C, whereas compound **7**, as already discussed, sublimes at 135 °C. The residue after decomposition in the case of compound **11** is slightly higher than 15%, meaning that a major part of the compound is evaporated intact. Unfortunately, due to the small amount available from the synthesis, it wasn't possible to conduct the same comparative study on the  $\beta$ -diketiminato substituted compound **10**.

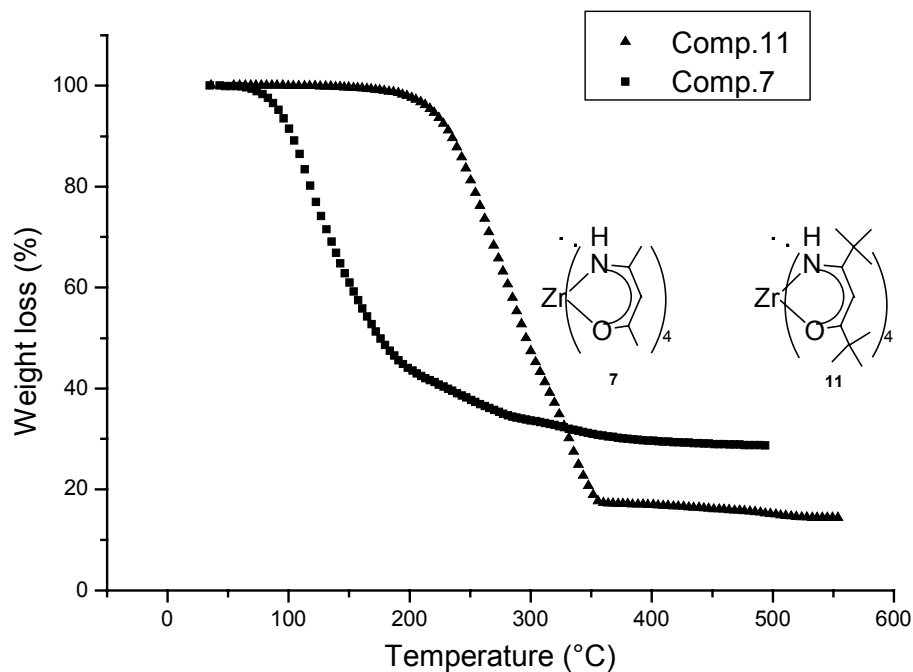


**Figure 4.36. Comparison between evaporation curves of two eight-coordinated ketoiminato-substituted compounds**

#### 4.7.2 Thermal properties of guanidinato-based compounds.

Compounds **12** and **13** are much less volatile than the corresponding  $\beta$ -diketiminato substituted compounds. Both **12** and **13** have similar volatility and sublime at a very slow rate at a bath temperature of about 148-150 °C. It is interesting to compare the volatility of these molecules with that of compounds **1** and **2**, where the only structural variation is the ancillary bidentate ligand. The reason for the lower vapor pressure of compounds **12** and **13** might be found simply in the higher molecular weight of these compounds compared to the structurally related **1** and **2**.

For example, **1** has a molecular weight about 30 % lower than **12**. A higher dipole moment contribution coming from the guanidinato ligand might be an additional reason. The TG traces of compound **12** and **13** are very similar, and therefore only that of compound **12** is displayed in Figure 4.37. It can be observed that in the temperature range from 50 to 100 °C, about 15% of the starting weight is lost. This is likely not due to intact evaporation of the molecule, but rather from partial loss of ancillary ligands due to thermal decomposition. The melting point of compound **12** was found to be 167-169 °C, after which the compound decomposed. The residue after decomposition is about 26 % of the initial weight. For compounds **12** and **13** several attempts were carried out to detect the melting or decomposition point by means of DSC analysis, but it wasn't possible to find any peak, probably due to the small amount of energy involved in this kind of transition for both compounds.

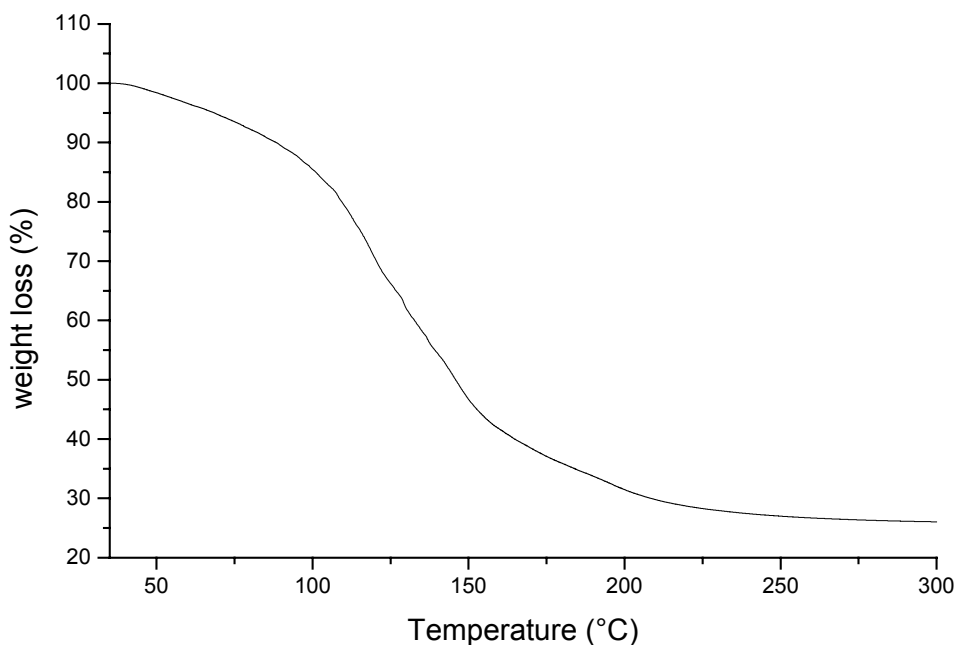


**Figure 4.37. TG trace of the six-coordinate guanidinato-based compound 12.**

### 4.7.3 Vapor Pressure measurements of compound 1.

Since compound  $\text{Zr}(\text{MeNacNac})(\text{NMe}_2)_2$  (**1**) is one of the most volatile substances that we have been able to prepare and therefore the best candidate to be tested in CVD experiments, we have measured its vapor pressure using our home-built apparatus, based on the gas-flow method (described in the experimental section). This kind of measurement allows us to obtain the  $\Delta H_{\text{subl}}$  in the temperature range studied. This is an important parameter to characterize the intermolecular forces in the system studied and when considering the precursor evaporation process during CVD experiments. A first series of measurements was performed in a temperature range from 90 to 140 °C, and the results are shown in Table 7. The value of average pressure reported at each temperature, is the measured total pressure, averaged over the duration of an experiment at a given temperature. The third column indicates the duration of the experiment at a given temperature. The fourth column indicates the measured concentration of zirconium in the solution obtained at the end of each experiment, while column five displays the absolute weight of zirconium collected. The vapor pressure is calculated from these data using the procedure indicated in Chapter 6. One data point (115 °C) was repeated to check the reproducibility, giving a satisfactory result. Slightly over 140 °C the compound melts with decomposition, so this is the upper temperature limit. In Figure 4.38 the vapor pressure of the compound is plotted *versus* the temperature. Only at 125 °C does the vapor pressure reach 0.02 mbar, while at 140 °C it is almost in the  $10^{-1}$  mbar range. These values are acceptable to conduct CVD experiment with normal evaporator systems. From these data it is possible to extract the sublimation enthalpy using the famous Clausius-Clapeyron equation:  $\ln P = -\Delta H_{\text{subl}}(1/T) + \text{constant}$ . The plot is depicted in Figure 4.39.

**Table 7. Experimental data from vapor pressure measurements**

Temp.(°C)	Av. Press. (Pa)	Time (min.)	ppmZr(exp)	grams of Zr	VP(mbar)
90	96329	2970	0.02	3.96E-06	1.97E-05
95	95668	920	0.07	1.31E-05	1.93E-04
100	95893	992	0.01	5.69E-07	2.60E-05
105	96011	1118	0.08	6.45E-05	2.01E-04
110	96188	1250	0.73	4.80E-05	1.79E-03
115	96610	884	0.68	4.88E-06	2.91E-03
115	96088	1161	1.01	1.75E-04	3.55E-03
120	95647	367	0.14	1.32E-06	1.71E-03
125	96155	303	0.95	5.44E-05	1.03E-02
130	95941	377	2.66	2.88E-04	2.27E-02
135	96542	346	4.15	5.54E-04	4.12E-02
140	96338	319	7.27	8.75E-05	8.72E-02

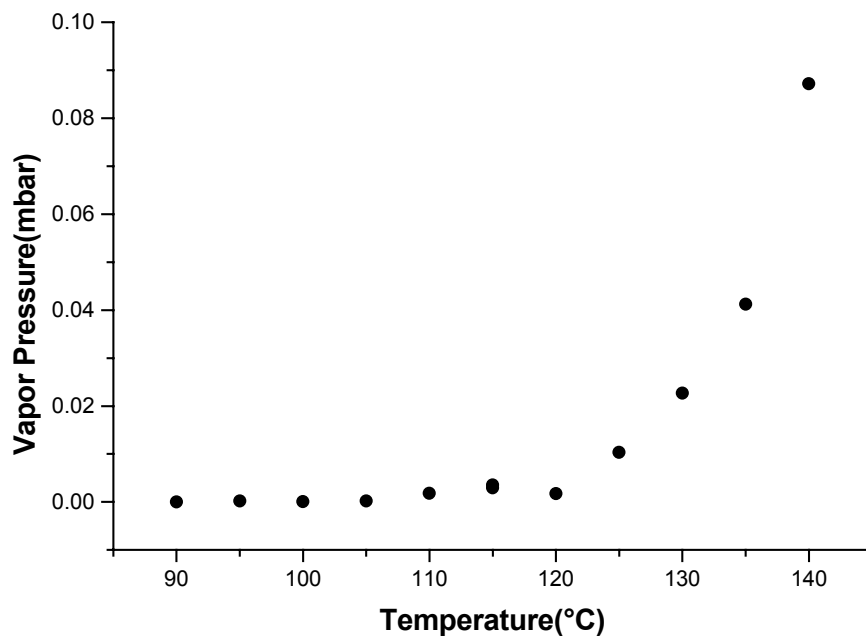


**Figure 4.38. Vapor pressure vs temperature for compound 1.**

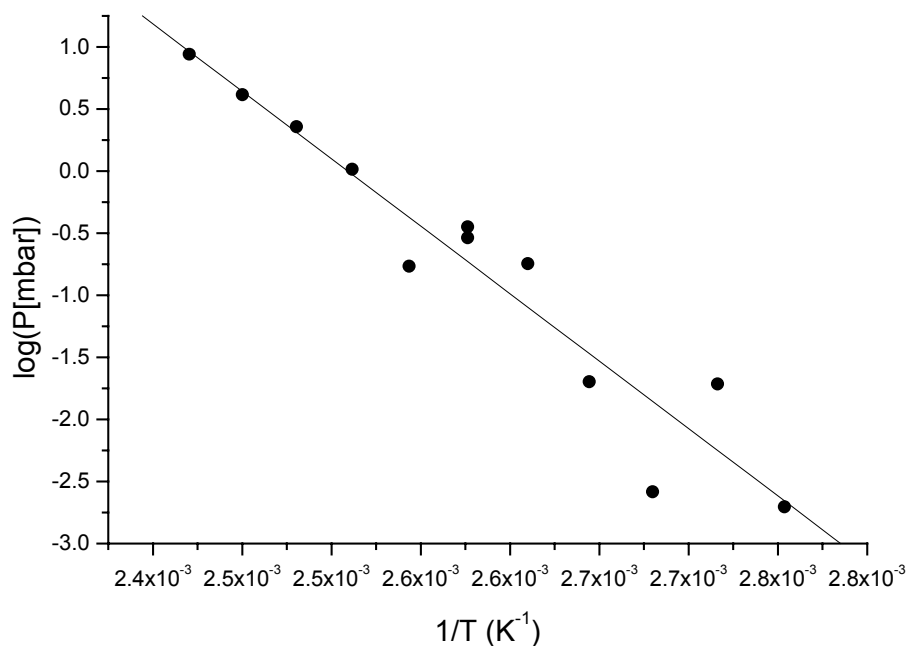


**Figure 4.39. Clausius Clapeyron plot for compound 1.**

As we can see from Figure 4.39 there is some scattering in the data in the low-temperature range. The amount of zirconium collected in the cold trap for this data point was very low (see table), and it is likely that we are at the limit of sensitivity of this technique. The scattering is lower in the higher temperature range, for instance from 120 to 140 °C, where the linear relationship is quite good. It has to be noted that this kind of measurement required that the substance be subjected to a thermal stress for a period of at least one week, which was probably too high for this compound, and might additionally account for the observed scattering in the data points. We observed an evident change in color to brownish at the end of the experiments, which is likely due to partial thermal decomposition of the substance. The remaining substance was dissolved in toluene at the end of the experiment and after filtration of a brownish insoluble portion we analysed the identity of the soluble part: indeed it displayed the expected proton NMR spectra. Nevertheless we believe



that the value obtained from the slope of the plot in Figure 4.39 is still a very good estimate of the enthalpy of sublimation.

The value of enthalpy of sublimation obtained by the slope of this curve is:

$$\Delta H_{\text{subl}} = 90.9 \pm 1.2 \text{ KJ/mol}$$

This is quite close to what has been found for related oxygen-containing six-coordinate compounds already reported in the literature <sup>[21]</sup>: for instance, for the six-coordinate compounds  $\text{Zr}(\text{acac})_2(\text{OSiMe}_3)_2$  and  $\text{Zr}(\text{acac})_2(\text{OSi}^i\text{BuMe}_2)_2$  a values of  $85.5 \pm 1.5$  and  $92.2 \pm 1.1$  KJ/mol were found, respectively.

## 4.8 Outlook.

In this chapter investigations concerning the chemistry of zirconium complexes in combination with bidentate ligands as well as monodentate ligands, and the characterization of their physical properties have been reported, with the aim of designing novel CVD precursors. The emphasis has been directed to the development of the chemistry of alkyl- and hydrogen-substituted  $\beta$ -diketiminato ligands, a field that was not yet investigated in the literature. With the same aims, we have also studied the chemistry and physical properties of guanidinato based ligands, also obtaining novel compounds in this case. In view of the application of these molecules as MOCVD precursors for nitrogen-containing zirconium-based thin films, this study provides an interesting “library” of compounds: for instance we have different molecules in which the ratio between the zirconium atom and other elements such as nitrogen and carbon is varied, providing a platform to investigate the composition of the film as a function of the composition of the precursor. Of course

the size of this library is limited by the fact that not all the compounds synthesized display the required characteristics to be used in CVD experiments.

The synthetic work performed here might also provide some suggestions on how to further improve the properties of the precursors. In this respect, we started an explorative phase of this work, considering fluorinated  $\beta$ -diketimines. First attempts to use fluorinated  $\beta$ -diketonates to obtain fluorinated  $\beta$ -diketimines were unsuccessful, indicating that the introduction of fluorine atoms radically changes the reactivity and should require a deeper study of this chemistry, which is outside the scope of this thesis. An interesting fluorinated ligand has been described in literature<sup>[22]</sup> but the high cost for the starting material might be a serious limitation to further development in this direction.

## References

- [1] M. Rahim, N. J. Taylor, S. X. Xin, S. Collins, *Organometallics* **1998**, *17*, 1315.
- [2] L. Kakaliou, W. J. Scanlon, B. X. Qian, S. W. Baek, M. R. Smith, D. H. Motry, *Inorg. Chem.* **1999**, *38*, 5964.
- [3] B. X. Qian, W. J. Scanlon, M. R. Smith, D. H. Motry, *Organometallics* **1999**, *18*, 1693.
- [4] D. E. Bowen, R. F. Jordan, R. D. Rogers, *Organometallics* **1995**, *14*, 3630.
- [5] G. M. Diamond, S. Rodewald, R. F. Jordan, *Organometallics* **1995**, *14*, 5.
- [6] J. N. Christopher, G. M. Diamond, R. F. Jordan, J. L. Petersen, *Organometallics* **1996**, *15*, 4038.
- [7] G. M. Diamond, R. F. Jordan, J. L. Petersen, *Organometallics* **1996**, *15*, 4030.
- [8] G. M. Diamond, R. F. Jordan, J. L. Petersen, *Organometallics* **1996**, *15*, 4045.
- [9] J. Barluenga, C. D. Losada, B. Olano, *Tetrahedron Lett.* **1992**, *33*, 7579.
- [10] G. Garcia, A. Figueras, J. Casado, J. Llibre, M. Mokchah, G. Petot-Ervas, J. Calderer, *Thin Solid Films* **1998**, *317*, 241.
- [11] M. H. Siadati, T. L. Ward, J. Martus, P. Atanasova, C. Xia, R. W. Schartz, *Chem. Vap. Deposition* **1997**, *3*, 311.
- [12] J. C. Bailar, *Journal of Inorganic & Nuclear Chemistry* **1958**, *8*, 165.
- [13] J. V. Silverton, J. L. Hoard, *Inorg. Chem.* **1963**, *2*, 243.
- [14] W. Clegg, *Acta Crystallogr. Sect. C-Cryst. Struct. Commun.* **1987**, *43*, 789.
- [15] D. G. Black, D. C. Swenson, R. F. Jordan, R. D. Rogers, *Organometallics* **1995**, *14*, 3539.
- [16] P. J. Walsh, F. J. Hollander, R. G. Bergman, *Organometallics* **1993**, *12*, 3705.
- [17] T. G. Ong, D. Wood, G. P. A. Yap, D. S. Richeson, *Organometallics* **2002**, *21*, 1.
- [18] G. I. Nikonov, A. J. Blake, P. Mountford, *Inorg. Chem.* **1997**, *36*, 1107.
- [19] D. Wood, G. P. A. Yap, D. S. Richeson, *Inorg. Chem.* **1999**, *38*, 5788.
- [20] M. Morstein, *Inorg. Chem.* **1999**, *38*, 125.

- [21] S. Zurcher, M. Morstein, N. D. Spencer, M. Lemberger, A. Bauer, *Chem. Vap. Deposition* **2002**, *8*, 171.
- [22] O. E. Petrova, M. A. Kurykin, D. V. Gorlov, *Russ. Chem. Bull.* **1999**, *48*, 1688.

## 5. RESULTS AND DISCUSSION: CVD EXPERIMENTS

As already anticipated in the previous chapter, we have chosen the compound  $\text{Zr}(\text{MeNacNac})_2(\text{NMe}_2)_2$  (1) for CVD experiments, since it meets several requirements. First of all it is volatile, as it has been discussed in Chapter 4. Additionally its synthesis has been scaled up to obtain several grams, a key point for CVD applications. This compound, provided that it is stored under nitrogen, can be kept indefinitely at room temperature. Its handling is facilitated because of its lower moisture sensitivity compared, for example, to the  $\text{Zr}(\text{NR}_2)_4$  precursors.

Several process parameters play an important role during the deposition process: the substrate temperature, the type of carrier and reactant gas used, their respective flow rates, the evaporator temperature and the pressure inside the reactor. In this chapter we will describe how the variation of these parameters affects the deposition of our precursor.

The substrate used in all experiment is a single-side polished Si(100) wafer, which was subjected to *piranha-solution* cleaning, followed by HF etching prior to use.

We explored the different variables using the data shown in Table 1. The evaporator temperature was kept at 133 °C, which gives a good compromise between precursor delivery rate and the thermal stability required for the duration of several experiments. The carrier gas used was  $\text{H}_2$ , and  $\text{NH}_3$  the reactant gas. Some experiments have been carried out using Ar as carrier gas, ammonia as reactant gas, and  $\text{H}_2$  as carrier gas without addition of any reactant gas (entry M and N).

The XPS atomic composition reported in the table refers to measurement carried out on the as-deposited films and on the sputtered films: in some cases a mild sputtering of 45 seconds or 1 minute was carried out, to remove only the surface carbon and oxygen contamination, and in other cases a longer sputtering was performed to probe the composition in the bulk of the film. The sputtering time was never longer than 30 minutes in total.

**Table 1: process parameters and XPS composition for the CVD experiment performed with the precursor (Menacnac)<sub>2</sub>Zr(NMe<sub>2</sub>)<sub>2</sub>. Deposition time was between 30 and 33 minutes in all cases.**

Wafer	Subst. T (°C)	Reactor Pressure (mbar)	Gas		Growth rate (µg/min)	Sputt. time (min)	% Composition (XPS)			
			MFC1 gas /flow (cm <sup>3</sup> /min)	MFC2 gas /flow (cm <sup>3</sup> /min)			C	N	O	Zr
A	550	5	H <sub>2</sub> /7	NH <sub>3</sub> /30	56	0	41.16	5.373	32.89	20.58
						5	21.99	10.19	28.32	39.51
						10	21.77	16.32	21.63	40.28
						20	26.1	15.91	18.09	39.91
						30	25.62	16.53	17.3	40.54
B	550	15	H <sub>2</sub> /7	NH <sub>3</sub> /30	4.6	15.75	20.07	5.233	33.46	41.24
C	600	5	H <sub>2</sub> /7	NH <sub>3</sub> /30	33	0	48.07	4.264	26.28	21.38
						15	20.79	9.844	29.92	39.45
						25	24.49	5.188	28.23	42.1
D	550	25	H <sub>2</sub> /7	NH <sub>3</sub> /30	12	0	48.12	6.549	24.36	20.97
						0.75	44.57	5.8	21.13	28.5
						15.75	29.29	8.332	25.97	36.42
E	550	10	H <sub>2</sub> /7	NH <sub>3</sub> /30	11	0	41.02	5.74	29.77	23.47
						15	46.11	7.612	25.8	20.48
F	500	5	H <sub>2</sub> /7	NH <sub>3</sub> /30	34	0	19.11	6.83	31.19	42.87
						15	26.91	12.42	25.29	35.38
G	450	5	H <sub>2</sub> /7	NH <sub>3</sub> /30	18	0	43	2.737	31.3	22.97
						15	17.78	6.623	36.25	39.35
H	650	5	H <sub>2</sub> /7	NH <sub>3</sub> /30	18	0	35.67	4.835	36.49	23
						0.75	22.08	3.094	38.95	35.87
						15.75	19.46	4.785	31.56	44.19
I	400	5	H <sub>2</sub> /7	NH <sub>3</sub> /30	15.5	0.75	14.39	3.231	47.87	34.51
						20	15.2	4.125	47.26	33.41
L	575	5	H <sub>2</sub> /7	NH <sub>3</sub> /30	42.5	0	48.76	2.231	29.64	19.37
						10	25.4	6.977	35.35	32.27
						20	25.6	7.674	35.1	31.62
M	550	5	H <sub>2</sub> /7	Ar/30	39	0.75	19.69	4.111	44.53	31.67
						15.75	21.67	6.614	38.01	33.71
						20.75	21.36	7.666	37.6	33.38
N	550	5	Ar=7	NH <sub>3</sub> =30	17	0.75	33.83	4.741	30.55	30.88
						20.75	37.62	5.94	28.72	27.72

## 5.1 CVD kinetics

The reaction rate can be calculated from the weight difference of the wafer before and after the deposition, and it is expressed, in our case, as the mass of substance deposited per unit time ( $\mu\text{g}/\text{minute}$ ). The deposition time was in all cases around 30 minutes. A kinetic analysis can be performed for the experiments carried out at the same pressure, flow conditions and with the same gas mixture. Therefore we have compared the deposition rate obtained at 5 mbar, using  $\text{H}_2$  as carrier gas, and ammonia as reactant gas (entries A, C, F, G, H, I and L). The growth rate can be plotted as a function of temperature or, alternatively, in a logarithmic form as a function of the inverse of the temperature. The plot displayed in Figure 5.1 indicates an increase in the growth rate from 400 °C up to a temperature of 550 °C. In this temperature range a surface-reaction-controlled regime is active. Over this temperature the growth rate decreases. There is no intermediate regime, where the growth rate is constant as a function of temperature. In the range 400-550 °C it appears that the deposition is kinetically controlled, and the maximum is reached around 550 °C. Over 550 °C, decomposition of the precursor (likely due to heat irradiation from the substrate) might be occurring, and therefore we observe a decrease of the deposition rate when the temperature is increased. The energy of activation for the decomposition of the precursor can be estimated from the slope of the graph in the range between 400 and 550 °C. The calculated value is  $41 \pm 2 \text{ kJ mol}^{-1}$ . A comparison can be made with other oxygen-containing precursors reported by Zürcher *et al.*,<sup>[1]</sup> where values of  $63 \pm 3 \text{ kJ mol}^{-1}$  and  $145 \pm 7 \text{ kJ mol}^{-1}$  were found for the precursors  $\text{Zr}(\text{acac})_2(\text{OSiMe}_3)_2$  and  $\text{Zr}(\text{acac})_2(\text{OSi}^t\text{BuMe}_2)_2$ , respectively, or with the work by Morstein *et al.*<sup>[2]</sup>, where a value of  $78 \text{ kJ mol}^{-1}$  was found for the precursor  $\text{Zr}(\text{acac})_2(\text{hfip})_2$ . The lower thermal activation for our precursor compared to the above-mentioned oxygen-containing six-coordinate compounds is corroborated also by the thermal properties studied in Chapter 4. The deposition rate for this compound is lower than in the case of the four-coordinate  $\text{Zr}(\text{NR}_2)_4$  precursors studied by Allenbach<sup>[3]</sup>. It is difficult to make a comparison with the experiments

reported by Berndt *et al.*<sup>[4]</sup> and by Täschner *et al.*,<sup>[5]</sup> where plasma-assisted processes were employed, and higher deposition rate were obtained.

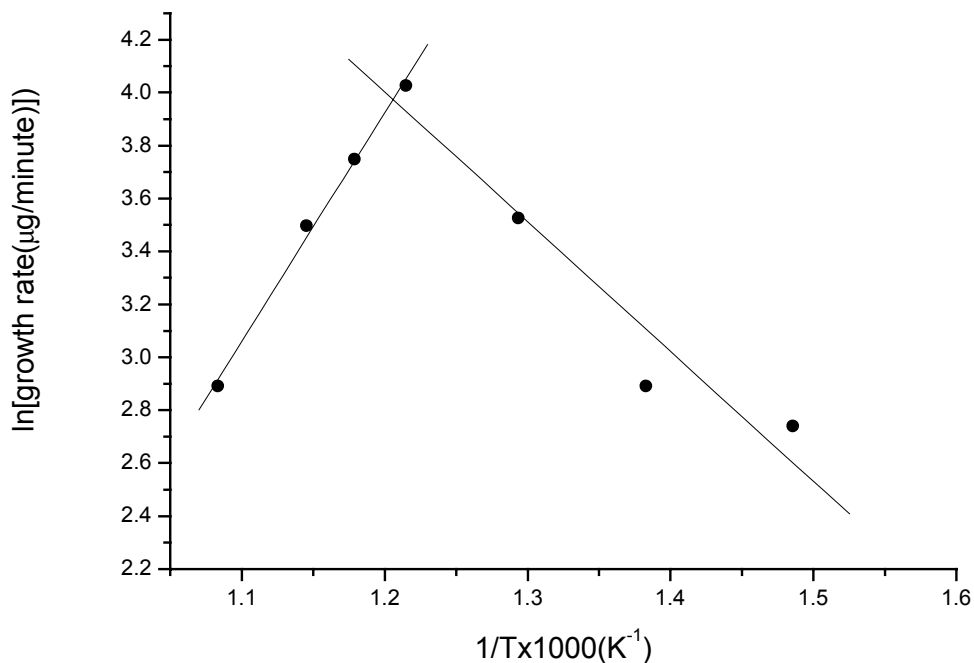


**Figure 5.1. Growth rate kinetics for compound 1 at 5 mbar reactor pressure, in the temperature range from 400 to 700 °C.**

The thickness of the film can be roughly estimated considering the weight gain of the wafer and making some assumptions concerning the density of the film. Considering an average value of the density of ZrO<sub>2</sub>, ZrN, and ZrC (which are 5.89, 7.09 and 6.73 g/cm<sup>3</sup>, respectively), the highest thickness obtained in the case of entry A is roughly 550 nm.



## 5.2 Film Composition

### 5.2.1 General considerations.

The surface composition of the deposited film has been analysed by XPS. A portion of the wafer was cut and, once mounted on the sample holder, it was blown with argon to remove dust, or any particle residues deposited during the cutting process. As mentioned at the beginning of this chapter, the analysis of the film was performed on the as-deposited films and after sputtering with  $\text{Ar}^+$ . This is probably not a completely reliable way to look at the composition below the near-surface region. One has always to be aware that preferential sputtering of one of the elements we are looking at, might be occurring. In addition, re-implantation of the ions that we want to remove from the surface, or changes in the oxidation state of metals might occur. Nevertheless, we can obtain interesting information about the film composition.

All analysed films display oxygen incorporation, which might be due to two main reasons: surface oxidation of the film once it is exposed to air after the CVD experiment, or incorporation of oxygen inside the growing film, as a result of the presence of  $\text{O}_2$  or water residues inside the CVD reactor. Concerning the first hypothesis, it must be stressed that the formation of an oxide film on the surface of zirconium-based nitride coatings is well documented in the literature. Milošev *et al.* studied the electrochemical oxidation of ZrN coating obtained by PVD: their XPS study clearly indicates that an oxide layer is formed upon exposure to air at room temperature<sup>[6]</sup>. Prieto *et al.* studied the phenomenon exposing ZrN PVD coatings to oxygen, and then studying the composition with XPS.<sup>[7]</sup> They showed that the film is not affected when the oxygen exposure is  $< 10^4$  L (L = Langmuir =  $10^{-6}$  Torr s) at an oxygen partial pressure of  $10^{-7}$  Torr. At higher oxygen exposure, a surface layer composed by  $\text{ZrO}_2$  and  $\text{Zr}(\text{N},\text{O})$  is formed. The reaction with oxygen stopped at  $10^8$  L, upon reaching saturation, and the thickness of the oxidized layer was estimated to be 1.7 nm. However, the detailed structure of the film, namely the relative ratio between  $\text{ZrO}_2$  and  $\text{Zr}(\text{N},\text{O})$  and their depth distribution was not unambiguously determined.

Horii *et al.*, showed that the surface oxidation can be partially inhibited by treating the sample with hydrazine after the deposition process.<sup>[8]</sup>

The second hypothesis, for instance the incorporation of oxygen in the film due to the presence of small amount of oxygen and/or water in the reactor during the deposition process, could also be taken into account. A small amount of oxygen-containing impurity would probably be sufficient to form  $ZrO_2$ , due to its very high thermodynamic stability. If we look at the thermodynamic data reported in literature, we can see that the standard enthalpies of formation of the compounds that we might have present in the film are:<sup>[9]</sup>

$$\Delta_f H_{ZrO_2} = -1100.6 \text{ kJ mol}^{-1}$$

$$\Delta_f H_{ZrC} = -365.3 \text{ kJ mol}^{-1}$$

$$\Delta_f H_{ZrN} = -196.7 \text{ kJ mol}^{-1}$$

The formation of zirconium oxide is thus thermodynamically strongly favoured over the corresponding carbide and nitride. As a general consideration, all the PVD deposition methods used to deposit pure  $ZrN$ , rely on kinetically controlled processes (for example using plasmas generated with different methods). This also applies in the case of thermal CVD, where, to suppress the formation of  $ZrO_2$ , we should set the experimental conditions to allow the other components (nitride or carbide) to grow faster. This kind of consideration might help us to interpret the data discussed in the following sections, where the composition of the surface as a function of several parameters will be discussed.

### 5.2.2 Composition as a function of pressure.

One of the parameters to be optimised during the CVD process is the pressure inside the reactor. In Figure 5.2 the XPS composition of the film as a function of reactor pressure is displayed for a substrate temperature of 550 °C. The composition corresponds to that of a film analysed after 20 minutes of Ar<sup>+</sup> sputtering. At 5 mbar, we can observe a maximum in the value of nitrogen content, whereas oxygen is at a minimum. This pressure value seems to provide a good compromise between the required precursor concentration inside the reactor and a reasonable precursor delivery rate. Moreover, as can be seen in Table 1, at 5 mbar the growth rate is the highest. Apparently the experimental conditions corresponding to a high growth rate allow us to obtain films with better quality (i.e. a lower amount of oxygen, and a higher amount of nitrogen). Over this pressure value, the precursor delivery to the reactor decreases and consequently the growth rate is also slower.

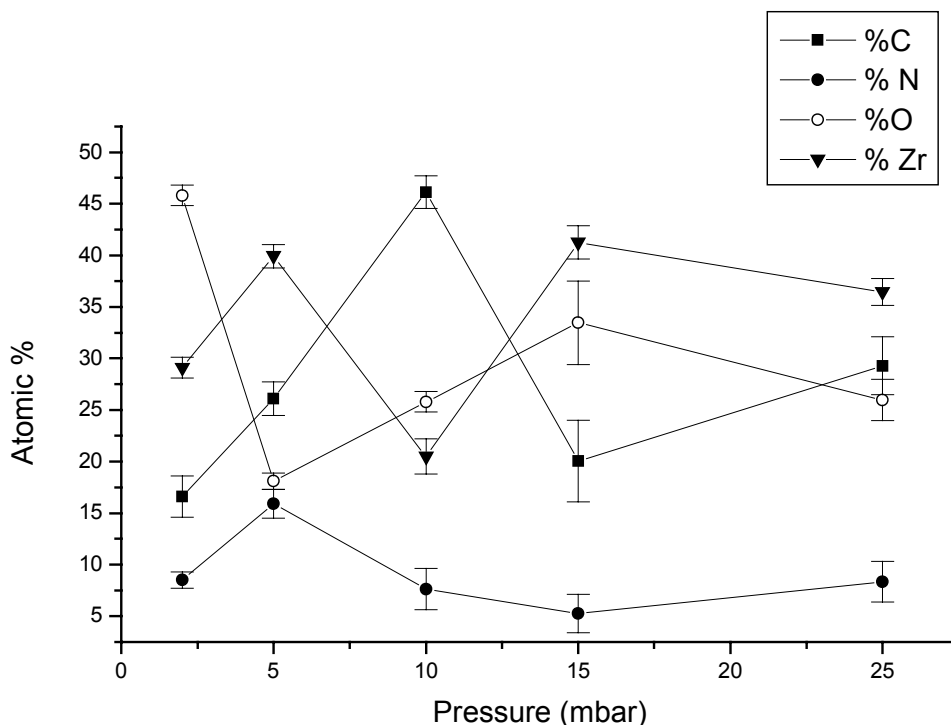


Figure 5.2 Composition of the film using precursor 1, as a function of pressure, for a substrate temperature of 550 °C. Composition after 20 minutes of sputtering.

### 5.2.3 Composition as a function of temperature.

The atomic percent concentration of the film is displayed in Figure 5.3 as a function of temperature in the range between 400 and 650 °C. The oxygen content has a minimum value for a substrate temperature of 550 °C

The XPS of the films obtained at 5 mbar reactor pressure displayed the highest atomic percent of nitrogen after 20 minutes of sputtering. We find again the higher nitrogen content, corresponding to the higher growth rate, around 550 °C. At to this temperature the oxygen content is at a minimum. Zirconium, as expected, remains constant. The carbon content is also slightly higher at a 550 °C substrate temperature.

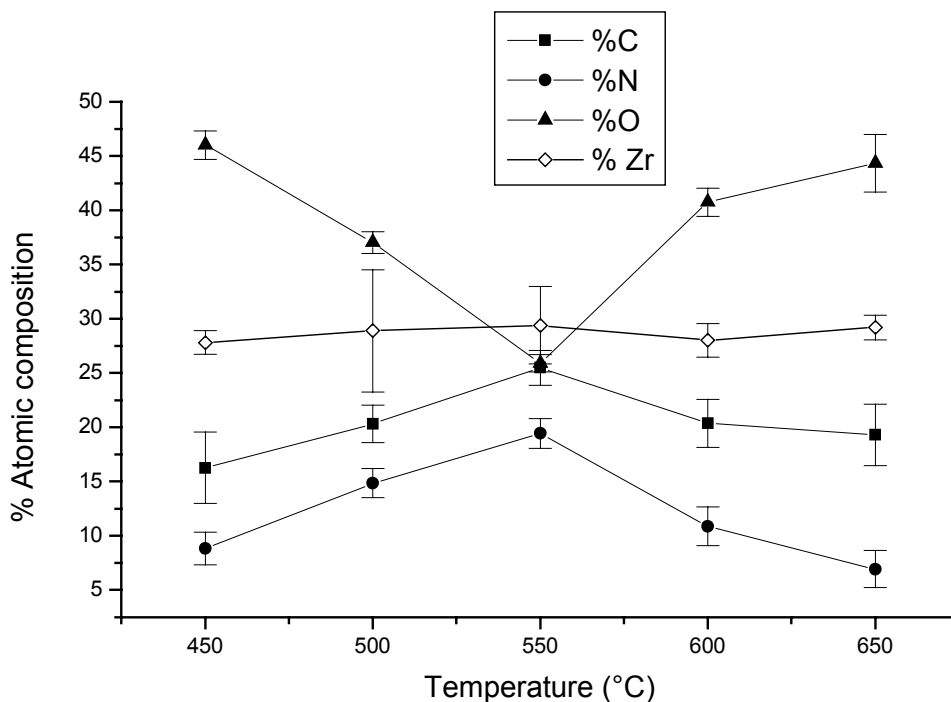
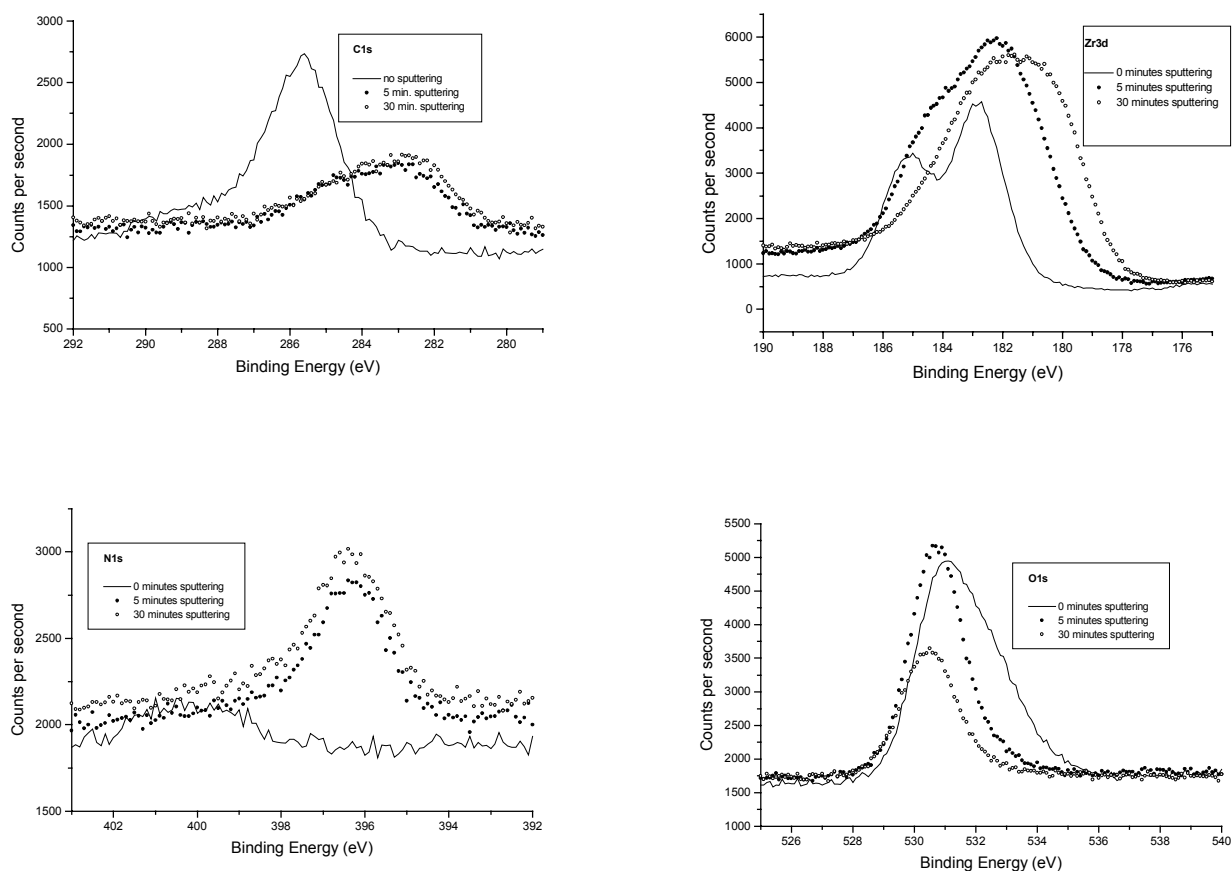


Figure 5.3. Composition of the films obtained using precursor 1 vs temperature, at 5 mbar reactor pressure. The carrier gas is H<sub>2</sub> and the reactant gas is ammonia/N<sub>2</sub> mixture. Spectra collected after 20 minutes of sputtering.

#### **5.2.4 Composition as a function of depth.**

As seen from the composition analysis as a function of pressure and temperature carried out in the previous section, the reaction conditions corresponding to a substrate temperature of 550°C, 5 mbar reactor pressure (Table 1, A), are those that yield the highest content of nitrogen in the film. We therefore report here a more detailed analysis of the XPS spectra. As we can see in Figure 5.4, all the components display a marked variation as a function of the sputtering time, indicating a variation in the composition moving from the near-surface region towards the bulk of the film.



**Figure 5.4 C1s, Zr3d, N1s and O1s XPS spectra after different sputtering times, for a film deposited using parameter set A (Table1).**

The variation in the composition as a function of sputtering time for the parameter set A is summarized in Figure 5.5. A sudden drop in the concentration of carbon is observed, as a result of the removal of the contamination layer. The zirconium concentration stabilizes to a constant value, as expected, after 5 minutes of sputtering. The oxygen atomic percent drops to half of the starting value after 5 minutes, while the nitrogen content reaches a stable value of about 15 %. Oxygen seems to be present in the bulk of the film. Apparently this amount of oxygen contamination is due to incorporation during the deposition. The reason could be water or oxygen adsorbed on the reactor walls. Several tests have been performed to evaluate the influence of the reactor baking conditions on the

composition of the film, but even keeping the reactor under rotary-pump vacuum for times as long as 24 h while warming the substrate to 200 °C, gave no appreciable changes.

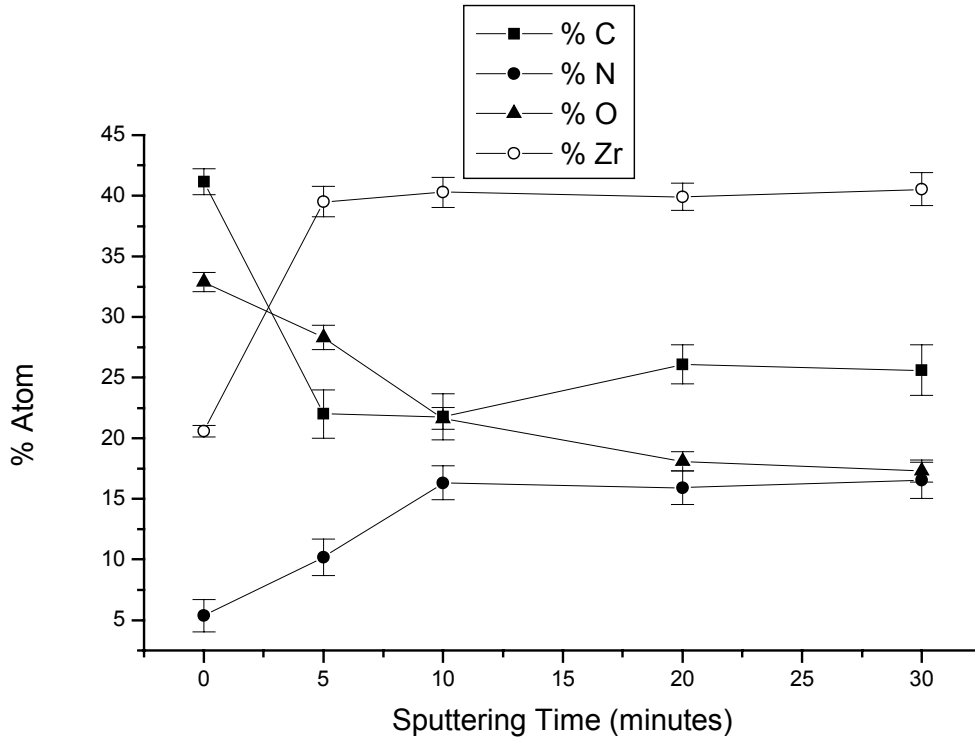


**Figure 5.5** Composition as a function of sputtering time for the parameter set A.

We have performed a peak deconvolution of the signals obtained at different sputtering depths. The Zr 3d signal has been fitted considering the contribution of ZrN, Zr(N,O), ZrC and ZrO<sub>2</sub> peaks taken from the literature<sup>[6, 7]</sup>. Each of these signals is a doublet (3/2 and 5/2 component) separated by 2.34 eV. The ratio between the d<sub>5/2</sub> and d<sub>3/2</sub> component area was fixed to 3:2. The binding energy values, full width at half maximum (FWHM), were also taken from the literature<sup>[6]</sup> and are displayed in Table 2:

**Table 2: Constrained parameters used in the fitting procedure.**

	<b>Peak</b>	<b>Binding energy (eV)</b>	<b>FWHM (eV)</b>
ZrN	Zr 3d <sub>5/2</sub>	180.1	1.8
Zr(N,O)	Zr 3d <sub>5/2</sub>	182.2 ± 0.3	1.5
ZrO <sub>2</sub>	Zr 3d <sub>5/2</sub>	183.1	1.5
ZrC	Zr 3d <sub>5/2</sub>	180.6	1.5 ± 0.2

In all the fitting procedures, the BE and FWHM of the ZrO<sub>2</sub> and ZrN were constrained to the above-listed values, thereby only allowing the height of the components to be varied during the least square fitting. Additional constraints are, of course, the Zr<sub>5/2</sub>/Zr<sub>3/2</sub> ratios, and the BE difference  $\Delta = Zr_{5/2} - Zr_{3/2} = 2.34$  eV.

In Figure 5.6 the Zr 3d spectrum is displayed for the as-deposited film, at 550 °C, fitted using the data contained in Table 2. The fitting is performed assuming the presence of a surface oxide layer and an oxynitride. If only the ZrO<sub>2</sub> components listed in Table 1 was used, the fitting failed to reproduce the experimental signal. As already observed for PVD-produced coatings, an oxynitride phase is necessary to describe an intermediate oxidation stage<sup>[6, 7]</sup>. The binding energy value of the oxide component was kept fixed, according to the literature value and that of the oxynitride was allowed to change by ± 0.3 eV from the value reported in Table 2. The binding energy value of the Zr3d<sub>5/2</sub> component of the oxynitride calculated from the fitting is in good agreement with that reported in the literature<sup>[6]</sup>. The oxide portion is slightly higher, being about 60 % of the whole peak.



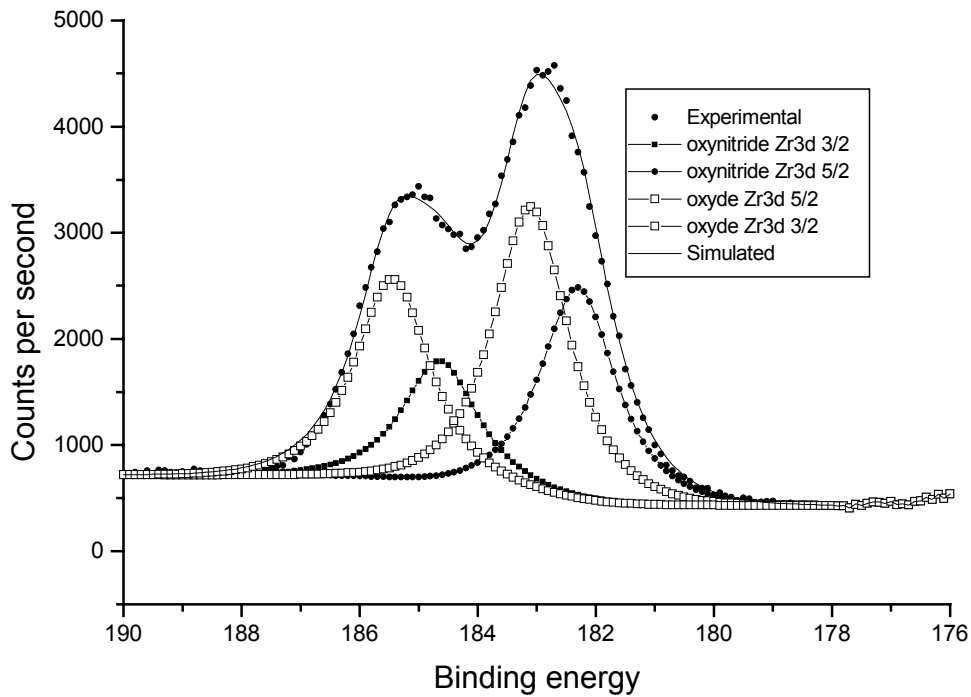


**Figure 5.6 Zr 3d peak fitting, as-deposited film. Temperature = 550°C. Parameter set A.**

In the following picture (Figure 5.7), the Zr3d signal is displayed after 5 minutes of  $\text{Ar}^+$  sputtering, in order to analyse the underlying layer. The reproduction of the signal is only good if we include the oxynitride component coming from the surface oxidized layer and the carbide and nitride Zr components of the bulk film. The fitting is well reproduced also including the oxide component along with the former ones, but in the picture, for simplicity, only the oxynitride one is considered. If both are included in the fitting, the area of the oxide component is very small. It must be noted that in this fitting, the inclusion of this oxynitride component seems to be necessary to obtain a satisfactory reproduction of the experimental Zr 3d signal. The exclusion of the oxide component doesn't seem to affect the good reproduction of the signal whilst the inclusion of only the oxide component, excluding the oxynitride one, fails to give a good simulation of the experimental signal. For the component assigned to ZrC, a binding energy value of 181.1 eV is found, slightly different from what is found in the literature (180.6 eV)<sup>[10]</sup>.

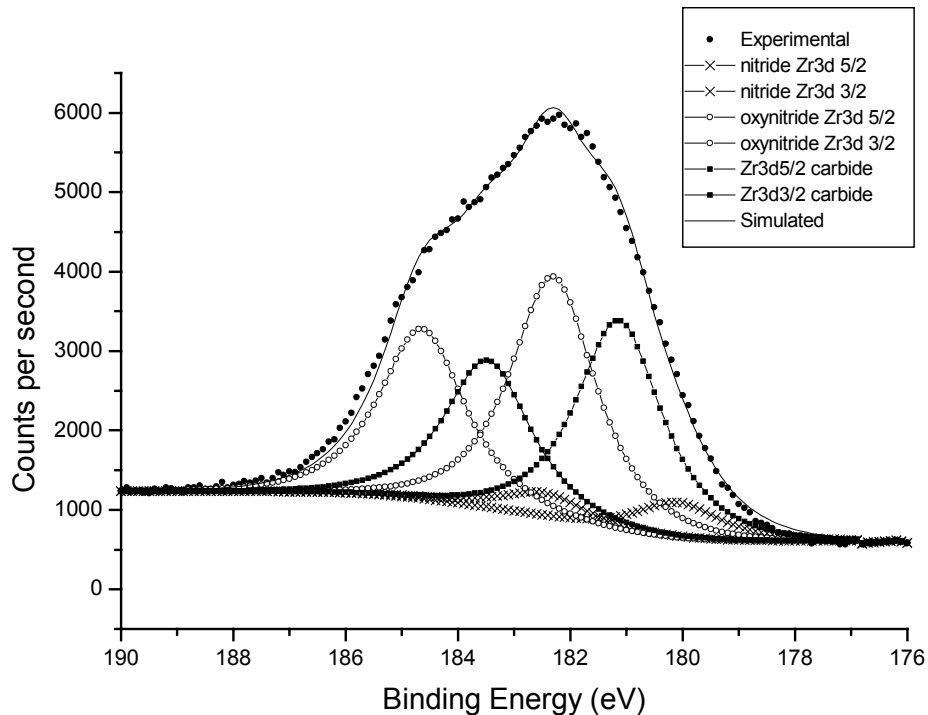


**Figure 5.7 Fitting of the Zr signal after 5 minutes sputtering. Parameter set A.**

It is noteworthy that, despite the large number of peaks used for the fitting, the number of constraints placed is quite strict; nevertheless the reproduction of the peaks is very good.

Continuing this kind of analysis for the Zr3d peaks obtained after 10, 20 and 30 minutes of sputtering, given the same starting values and constraint for the components, we obtained the graphs shown in Figure 5.8-5.10. The relative amount of the nitride component has increased after 30 minutes of sputtering, whereas the oxynitride becomes smaller. As observed for the signal in Figure 5.7, a good fit is also obtained excluding the oxide component, whereas the oxynitride has to be included. This is in agreement with a model in which a carbonitride film

is covered by a layer of oxide and oxynitride. Whether this overlayer is composed of two distinct thin films or of a continuous film with the two mixed phases, is difficult to judge from these data.

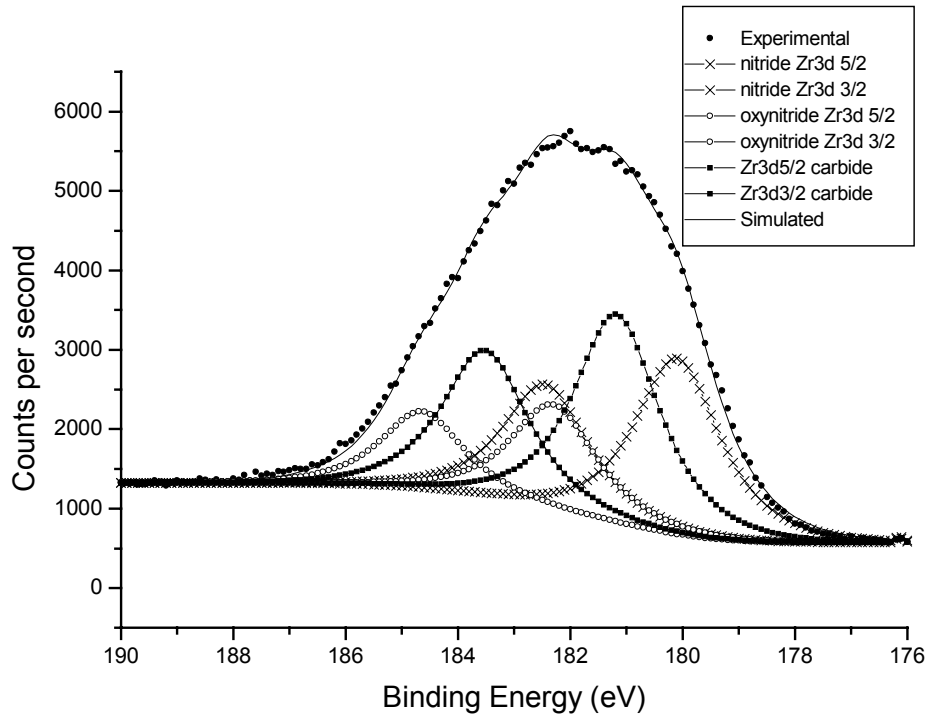


Figure 5.8 Fitting of the Zr signal after 10 minutes sputtering. Parameter set A.

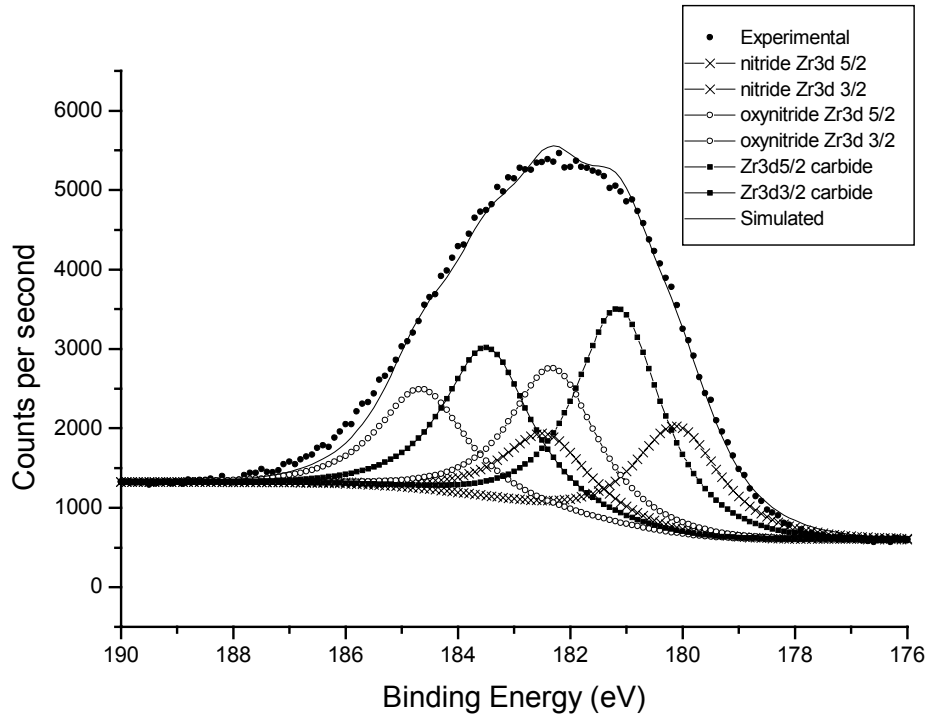


Figure 5.9 Fitting of the Zr signal after 20 minutes sputtering. Parameter set A.

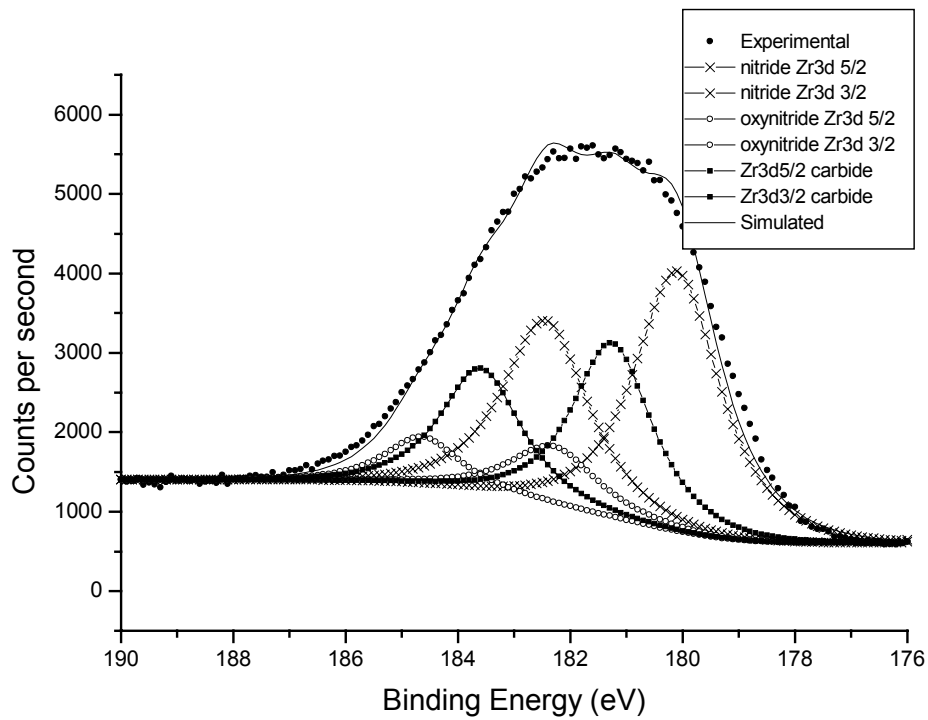


Figure 5.10 Fitting of the Zr signal after 30 minutes sputtering. Parameter set A.

These results concerning the Zr peaks can be summarized by the graph displayed in Figure 5.11, where the percent contribution of each component in the total Zr3d integral area (including in this case also the contribution from the oxide) is plotted against the sputtering time: already after 5 minutes the ZrO<sub>2</sub> contribution drops to a low value, whereas the nitride contribution increases; the carbidic component reaches a more-or-less constant value and the nitride steadily increases. This is another way to look at the data obtained in Figure 5.5, where the signal from the different elements was considered without referencing to the different contributions.

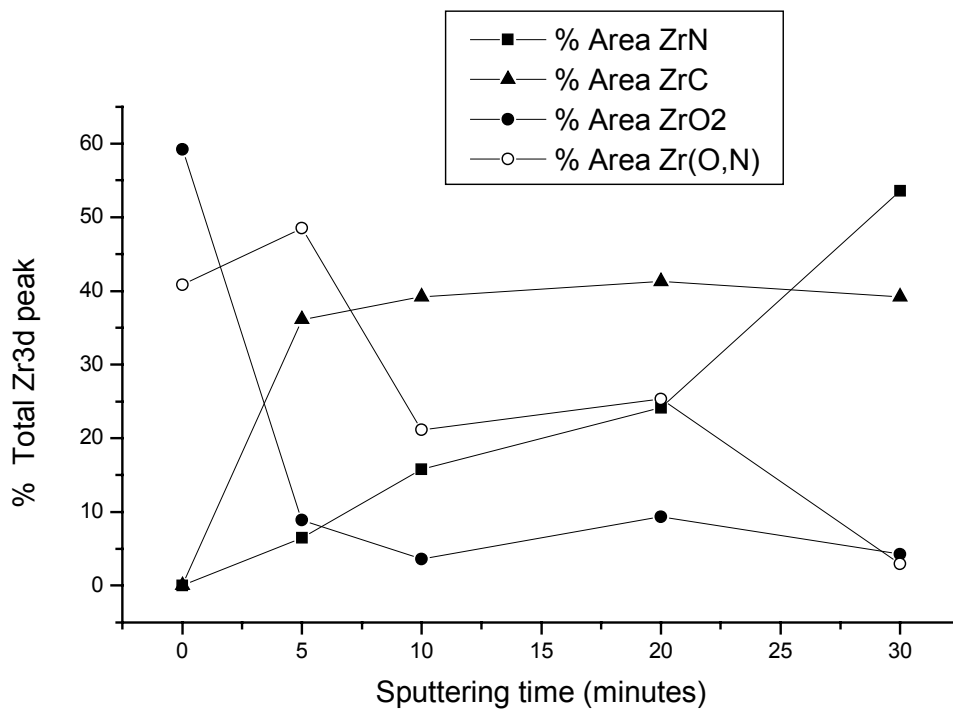
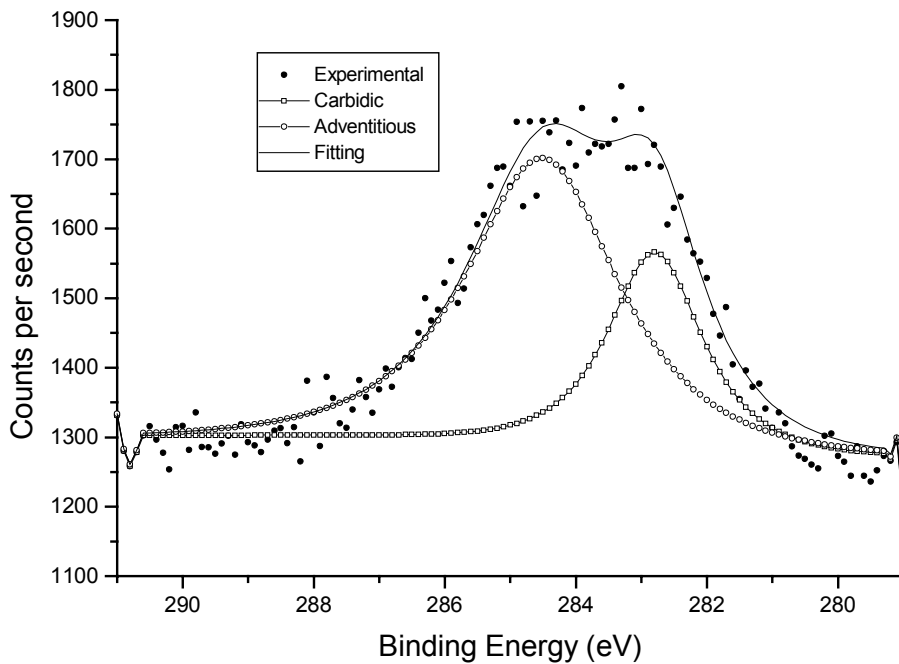
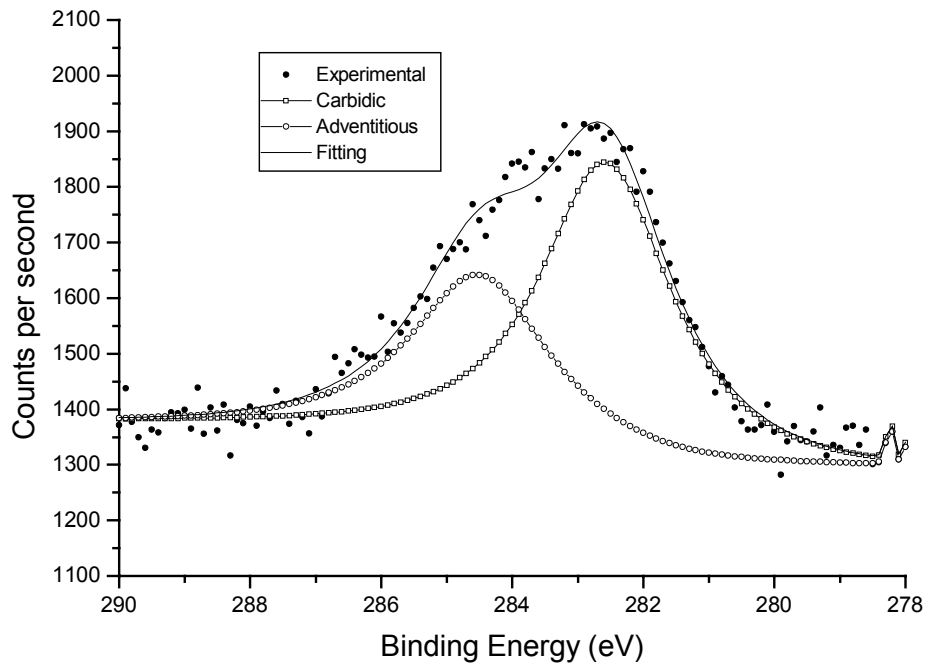


Figure 5.11 Percentage of the total Zr3d component

A similar can be taken with the XPS peaks for the C1s, O1s, and N1s. The C1s signal depicted in Figure 5.4 shows that the as-deposited film presents a large amount of carbon, mainly resulting from partial decomposition of the precursor. This thin layer is readily removed by Ar<sup>+</sup> etching. The signal found after sputtering presents two components assigned to carbidic carbon and adventitious carbon: the relative amount of the two components with respect to the total C1s changes after sputtering is displayed in Figure 5.12 and 5.13.



**Figure 5.12 C1s signal after 5 minutes of sputtering. Process condition A, Table 1.**



**Figure 5.13 C1s signal after 30 minutes of sputtering. Process condition A, Table 1.**

The N1s signal, with the corresponding fit, is shown in Figure 5.13 and 5.14, for films subjected to 5 and 30 minutes of sputtering, respectively. The as-deposited film (shown in Figure 5.3) presents a broad, weakly intense peak shifted towards higher binding energies (about 401 eV). The change in intensity and position upon sputtering is quite drastic. The N1s peak of oxidized ZrN surface reported by Milošev *et al.* has been fitted with three peaks: one corresponding to  $N^{3-}$  (at 397.3 eV), and two additional peaks assigned to two different types of oxynitride (396.3 and 400.05 eV), similarly as observed for the Ti(O,N) system<sup>[11]</sup>. In our case as well, the signal is well fitted with three peaks (Figure 5.13 and 5.14), but the binding energy positions are slightly different, being for the peaks A 395.8 eV, B at 396.7 eV and C at 398.8 eV. This might be due to the substantial difference of the system that we are studying compared to those already studied in the literature, where, for instance, no ZrC was present.

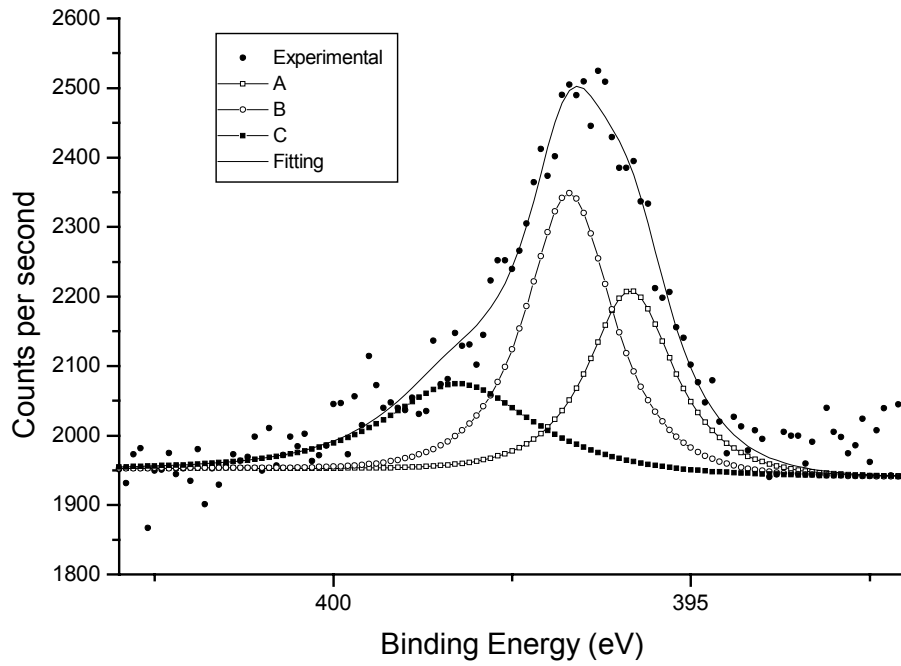


Figure 5.13 N1s signal after 5 minutes of sputtering. Process condition A, Table 1.

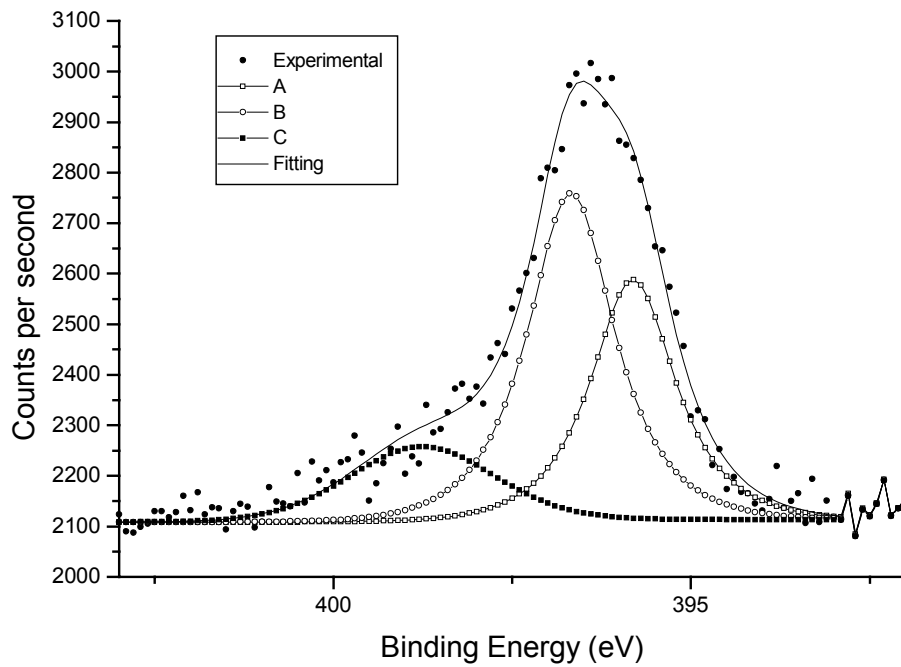


Figure 5.14 N1s signal after 30 minutes of sputtering. Process condition A, Table 1.



The O1s signal observed after sputtering is well described using a single component, being the FWHM after sputtering, always in the range of 1.6-1.8 eV. It is not possible from the binding energy value to distinguish the oxide and the oxynitride contribution.

### **5.2.5 Influence of the gas mixtures.**

Most of the CVD experiments were performed using a mixture of ammonia and nitrogen in a 1:9 ratio as reactant gas. The presence of ammonia is expected to help the reduction of the amount of carbon contamination in the film and to increase the nitrogen content. Two experiments (entry M and N) have been carried out to probe the influence of the change in the gas mixture used. To make a comparison, the temperature was fixed at 550 °C and the flow conditions were the same in both cases. As can be observed in Table 1, entry M, the entire amount of nitrogen found is coming from the precursor, but the absolute amount is lower, compared with the conditions in entry A. For entry N, without hydrogen, we find a higher amount of carbon in the film even after sputtering, and also the nitrogen content decreases to values between 4.7 and 6 %. This finding is in good agreement with what was observed in CVD experiments using  $Zr(NR_2)_4$  precursors.<sup>[3-5]</sup>

### **5.2.6 Morphology.**

The morphology of the film was analysed by scanning electron microscopy (SEM), both in plan view and afterwards in cross section.

All films appear very uniform and compact over an area of several microns, as can be seen in Figure 5.15 and 5.16, where some selected examples of films deposited at 500 and 650 °C are displayed, corresponding to the experimental condition F and H, Table 1.

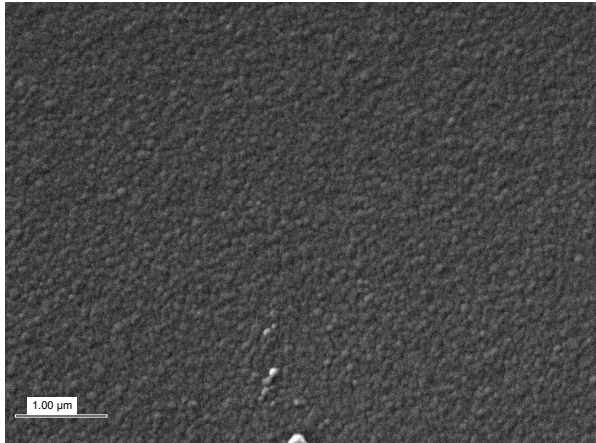


**Figure 5.15 SEM micrograph of the film deposited at 500 °C, entry F Table 1.**

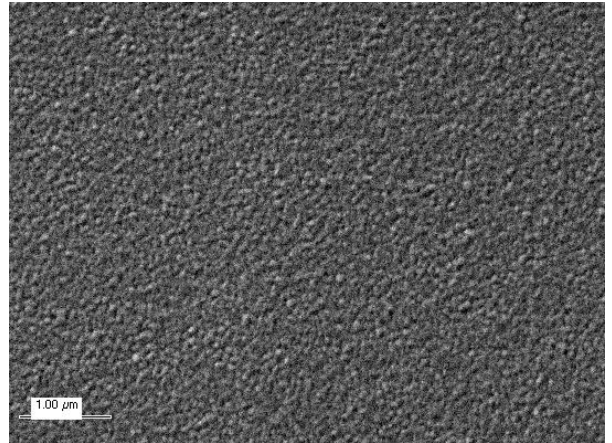


**Figure 5.16 SEM micrograph of the film deposited at 650 °C, entry H Table 1.**

In Figure 5.17 and 5.18, two additional example of micrograph collected at higher magnification are shown. It is possible to distinguish the contours of the grains composing the film, having sizes ranging from about 80 to 180 nm. Films obtained at different temperatures did not display special trends in the grain size: only slight changes can be observed, for example, comparing film grown at 550 and 450, with the film obtained at lower temperature having smaller grain size. Selected cross-sectional images of the fractured films deposited at 550 °C (A, Table 1) and 650 °C (H, Table 1), are shown in Figure 5.19 and 5.20: the films look quite compact and no columnar growth appears to be present. Täschner *et al.*,<sup>[5]</sup> obtained in plasma-assisted conditions films displaying columnar growth, although these coatings are much thicker than ours, therefore the comparison is not completely appropriate.

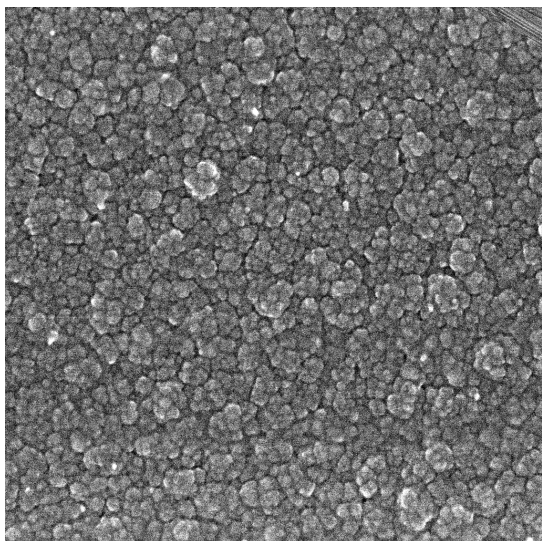


**Figure 5.17** 1  $\mu\text{m}$  x 1  $\mu\text{m}$  SEM micrograph of the film deposited at 550  $^{\circ}\text{C}$ , entry A Table 1.

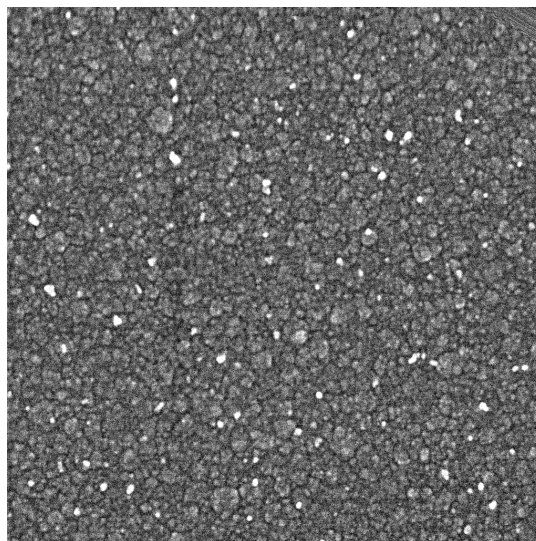


**Figure 5.18** 1  $\mu\text{m}$  x 1  $\mu\text{m}$  SEM micrograph of the film deposited at 450  $^{\circ}\text{C}$ , entry G Table 1.

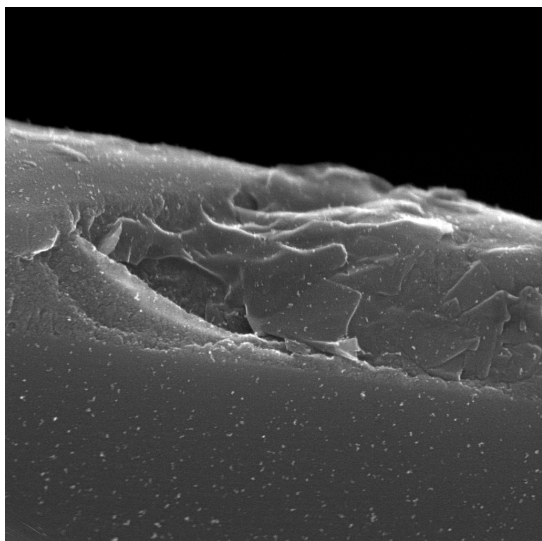


**Figure 5.19** 2  $\mu\text{m}$  x 2  $\mu\text{m}$  SEM cross-sectional micrograph of the film deposited at 550  $^{\circ}\text{C}$ , entry A Table 1.

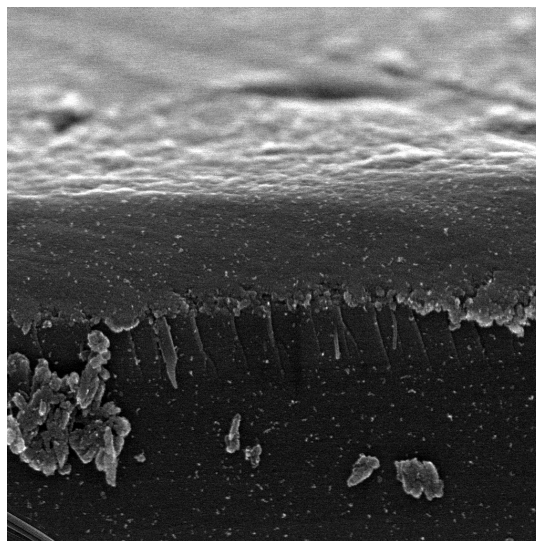


**Figure 5.20** 2  $\mu\text{m}$  x 2  $\mu\text{m}$  SEM cross-sectional micrograph of the film deposited at 650  $^{\circ}\text{C}$ , entry H Table 1.

## References

- [1] S. Zurcher, M. Morstein, N. D. Spencer, M. Lemberger, A. Bauer, *Chem. Vapor Depos.* **2002**, *8*, 171.
- [2] M. Morstein, I. Pozsgai, N. D. Spencer, *Chem. Vap. Deposition* **1999**, *5*, 151.
- [3] C. P. Allenbach, ETH Zürich, Laboratory for Surface Science and Technology (Zürich), **2000**. <http://e-collection.ethbib.ethz.ch/show?type=diss&nr=13832>
- [4] H. Berndt, A. Q. Zeng, H. R. Stock, P. Mayr, *Surf. Coat. Technol.* **1995**, *74-5*, 369.
- [5] C. Taschner, K. Bartsch, A. Leonhardt, *Surf. Coat. Technol.* **1993**, *61*, 158.
- [6] I. Milosev, H. H. Strehblow, M. Gaberscek, B. Navinsek, *Surf. Interface Anal.* **1996**, *24*, 448.
- [7] P. Prieto, L. Galan, J. M. Sanz, *Surf. Interface Anal.* **1994**, *21*, 395.
- [8] S. Horii, T. Toda, S. Horita, *Jpn. J. Appl. Phys. Part 2 - Lett.* **2001**, *40*, L976.
- [9] Values taken from *TAPP Version 2.2*, ES Microwave, Inc., Hamilton (OH), 1995.
- [10] P. C. Wong, Y. S. Li, K. A. R. Mitchell, *Surf. Rev. Lett.* **1995**, *2*, 297.
- [11] J. S. Colligon, H. Kheyrandish, L. N. Lesnevsky, A. Naumkin, A. Rogozin, Shkarban, II, L. Vasilyev, V. E. Yurasova, *Surf. Coat. Technol.* **1994**, *70*, 9.

## 6. EXPERIMENTAL SECTION

### 6.1 Routine analysis instrumentation

NMR spectra were recorded on a Varian Gemini-200 spectrometer,  $^1\text{H}$  at 199.98 MHz,  $^{13}\text{C}$  at 50.29 MHz, and on a Varian Gemini-300 instrument,  $^1\text{H}$  at 300.08 MHz,  $^{13}\text{C}$  at 125.23 MHz. All NMR spectra were recorded at room temperature, unless otherwise stated.

Elemental analyses: Leco CHN(S)-932 instrument.

Thermogravimetry: Perkin Elmer TGA7 thermobalance, operating under an atmosphere of purified nitrogen at 30 mL/min. Mass spectra: Finnigan-MAT-8400 spectrometer; the sample was placed in an open platinum pan.

Differential Scanning Calorimetry: Perkin Elmer DSC7 instrument, sample placed in a sealed aluminum pan.

### 6.2 Syntheses.

**General considerations.** All reactions and manipulations were performed under an atmosphere of dry nitrogen using standard Schlenk techniques or a glove box. All solvents were dried using conventional methods and freshly distilled before use. All chemicals, except for  $\text{ZrCl}_4$  (99.9%, Aldrich Chemicals), were obtained from Fluka Chemicals Switzerland, and dried and distilled before use when necessary.

$\text{ZrCl}_4(\text{thf})_2$ ,<sup>[1]</sup>  $\text{Zr}(\text{NMe}_2)_4$ ,<sup>[2]</sup> and  $\text{Zr}(\text{NEt}_2)_4$ <sup>[3]</sup> were prepared according to published methods. The  $\beta$ -ketoimines<sup>[4, 5]</sup> and  $\beta$ -diketimines<sup>[6]</sup> were also prepared according to literature procedures.  $\text{Cp}_2\text{TiMe}_2$  was prepared as reported in the literature.

**Synthesis of HMeNacac**<sup>[4]</sup>. 20 mL of freshly distilled Hacac (19.5 g, 0.20 moles) were placed in a 250 mL round bottom flask. A 40 % solution of methylamine in water

(0.21 moles) was added dropwise to the Hacac cooled in an ice bath. At the beginning a white precipitate was formed, followed by the formation of a pale yellow solution, which was stirred for 2 hours. The reaction mixture was extracted with 4x50 mL of diethylether and dried over MgSO<sub>4</sub>. After filtration the solvent was removed *in vacuo*, to leave a pale yellow-brownish solid that can be purified either by crystallization or better by sublimation at 50 °C bath temperature, cold finger temperature -10 °C, at 0.1 mbar. In this last case the yield is 26.2 g, 58%. The identity of the product compared to that reported in the literature has been confirmed by NMR <sup>1</sup>H NMR (C<sub>6</sub>D<sub>6</sub>) δ 1.28, 2.02, 4.86, 10.90.

**Synthesis of HMeNacNac** <sup>[6]</sup>. Et<sub>3</sub>OBF<sub>4</sub> (7.30 g, 38.4 mmoles) is dissolved in 25 mL of CH<sub>2</sub>Cl<sub>2</sub> and this solution is added dropwise over 20 minutes to a solution of HMeNacac (4.34 g, 38.4 mmoles) in CH<sub>2</sub>Cl<sub>2</sub> (10 mL). After allowing the pale yellow solution to stir for 20 minutes, an 8 M solution of methylamine in ethanol was added over 30 minutes while keeping the reacting mixture at 0 °C. The solution was stirred for an additional 2 hours, during which a white precipitate of NHMeBF<sub>4</sub> was sometimes observed to form. The solvent was removed to leave a yellow solid that was dried in *vacuo* for 1h. The mixture was subsequently dissolved in 15 mL of dry methanol, and the solution cooled in an ice bath. NaOCH<sub>3</sub> was added as a solid and the bath removed. The solution was stirred for an additional hour at the end of which, the solvent was vacuum removed. The yellow-brownish solid obtained can be sublimed at a bath temperature of 80 °C, 0.1 mbar. Yield 3.83 g 79 %. The identity of the product compared to that reported in the literature has been confirmed by NMR. <sup>1</sup>H NMR (C<sub>6</sub>D<sub>6</sub>) δ 1.64, 2.78, 4.63, 11.05. <sup>13</sup>C NMR {<sup>1</sup>H} δ 18.72, 30.03, 94.72, 161.44.

**Synthesis of HNacac.** The most convenient way to synthesize this starting material was by the condensation of acetylacetone with aqueous ammonia as described by Braibante *et al*, <sup>[5]</sup> catalysed by montmorillonite K-10. The procedure

was slightly modified using  $\text{CH}_2\text{Cl}_2$  as a solvent. 30 mL of freshly distilled Hacac (29.2 g, 0.3 moles) were placed in a 250 mL round-bottom-flask and 100 mL of  $\text{CH}_2\text{Cl}_2$  were added. 20 g of Montomorillonite K-10 were carefully added (the mixing is slightly exothermic) and the slurry was stirred. A 25 % solution of ammonia in water (40.8 g, 0.6 moles) was carefully added (exothermic reaction) and the mixture stirred for 48 hours. The slurry was filtered on a paper filter and the solid washed with 2x30 mL of  $\text{CH}_2\text{Cl}_2$ . The filtrate was collected and NaCl added to improve the separation between the organic and water phases. The organic phase was washed with 2x40 mL of brine and subsequently dried over  $\text{Mg}_2\text{SO}_4$ . The solvent was removed *in vacuo*, and the brown solid obtained is transferred into a sublimator. When sublimation was performed at 0.1 mbar, 55 °C bath temperature, -10 °C cold finger temperature, a white crystalline solid was obtained. Yield: 20.4 g (68 %).  $^1\text{H}$  NMR ( $\text{C}_6\text{D}_6$ )  $\delta$  1.21, 1.97, 4.02 (very broad), 4.82, 9.83 (very broad).  $^{13}\text{C}$  NMR  $\{^1\text{H}\}$   $\delta$  21.41, 229.27, 95.67, 159.78.

**Synthesis of HNacNac<sup>[6]</sup>.** The following procedure presents some minor modifications with respect to the reported protocol.  $\text{Et}_3\text{OBF}_4$  (14.42 g, 75.90  $\mu\text{moles}$ ) was dissolved in 30 mL of dichloromethane and added dropwise over 20 minutes to a solution of HNacac in 50 mL of dichloromethane. The solution was stirred for additional 30 minutes. A 2.0 M solution of ammonia in dry ethanol (38 mL, 76  $\mu\text{moles}$ ) was added dropwise over 40 minutes, while keeping the solution at 0 °C. After 2 hours stirring, the mixture was filtered to remove a white precipitate of  $\text{NH}_4\text{BF}_4$ . The filtrate was collected and the solvent removed *in vacuo* to give a yellow viscous residue (weight 13 g, 90 % yield of  $\text{H}_2\text{NacNac}^+\text{BF}_4^-$ ), which was dried for an additional 2 hours. This residue was redissolved in dry methanol (100 mL) and cooled in an ice bath: to this solution, sodium methoxyde (3.86 g, 70.07  $\mu\text{moles}$ ) was added as a solid and the resulting suspension was stirred for 1 hour. The suspension was cooled with an ice bath and dried *in vacuo*. The yellow solid was extracted with 100 mL of ether, filtered, and the filtrate subsequently vacuum dried while keeping the solution at 0 °C. The residue was distilled at 0.1 mbar, 50 °C bath temperature, to

give a colorless air- and moisture-sensitive liquid. Yield 2.31 g (31%).  $^1\text{H NMR}$  ( $\text{C}_6\text{D}_6$ )  $\delta$  1.57, 4.48 (very broad), 10.1 (very broad).

**Synthesis of HPrNacac<sup>[4]</sup>.** Hacac (20 mL, 19.46 g, 0.20 moles) was placed in a 250 mL round bottom flask. 10 grams of  $\text{Na}_2\text{SO}_4$ , as a water scavenger, were added, then followed by ethanol (100 mL). To this suspension, isopropylamine (26 mL, 17.7g, 0.3 moles) was added with a syringe (slowly, the reaction is exothermic) and the solution refluxed for 6 hours. The mixture was filtered on a paper filter and subsequently, the solvent was removed *in vacuo*. The pale yellow residue was dissolved in 50 mL of pentane and an additional 10 grams of  $\text{Na}_2\text{SO}_4$  were added, after which the product was allowed to stand overnight. The solution was filtered on a paper filter, the filtrate dried under vacuum and the residue distilled at 35 °C, 0.1 mbar. A pale yellow distillate was recovered. Yield 5.67 g, (20%). By NMR we established the identity of the desired product.  $^1\text{H NMR}$  ( $\text{C}_6\text{D}_6$ )  $\delta$  0.75, 0.78, 1.41, 2.037, 3.06, 4.85.

**Synthesis of HPrNacNac<sup>[6]</sup>.** HPrNacac (5.67 g, 40.2 mmoles ) was dissolved in 100 mL of  $\text{CH}_2\text{Cl}_2$ .  $\text{Et}_3\text{OBF}_4$  was weighed in the glove box, and dissolved in 80 mL of  $\text{CH}_2\text{Cl}_2$ . The clear, colorless solution was poured into a dropping funnel and added to the former HPrnacac solution over a period of 15 minutes. The mixture was stirred for 2 ½ hours at room temperature. Isopropylamine dissolved in 20 mL of  $\text{CH}_2\text{Cl}_2$  was added dropwise over 5 minutes to the former solution. This yellow mixture was stirred for an additional hour, at the end of which all volatiles were removed *in vacuo* to recover the protonated immonium tetrafluoroborate salt of the  $\beta$ -diketimine in a quantitative yield. This yellow solid was subsequently purified by dissolving it in hot ethyl acetate and placing it at 0 °C overnight, to recover 9.15 g of yellow needle-like crystals (88 % yield). This compound was deprotonated dissolving it in 76 mL of 0.5 M sodium methoxide in methanol. The suspension was stirred for one hour, at the



end of which all volatiles were removed under vacuum. The product was extracted with 100 mL of dry toluene. After filtration, the filtrate was collected and the solvent removed *in vacuo*, to leave a pale-yellow liquid. Yield 4.59 g (63 %).  $^1\text{H}$  NMR ( $\text{C}_6\text{D}_6$ )  $\delta$  1.10, 1.13, 1.72, 3.46, 4.48, 11.35.  $^{13}\text{C}$  NMR  $\{^1\text{H}\}$   $\delta$  18.54, 24.83, 46.77, 94.50, 157.99.

**Synthesis of  $\text{Zr}(\text{MeNacNac})_2(\text{NMe}_2)_2$  (1):**  $\text{Zr}(\text{NMe}_2)_4$  (0.636 g, 2.38 mmol) was dissolved in 20 mL of toluene and stirred. The N-methyl-4-(methylimino)pent-2-en-2-amine (0.600g, 4.75 mmol) was dissolved in 10 mL of toluene and added to the previous solution. The pale yellow solution was stirred for 19 h at room temperature allowing the gaseous  $\text{HNMe}_2$  to escape from the reaction vessel. The toluene was removed *in vacuo* to a volume of 20 mL and the resulting solution passed through celite. The solution was then further concentrated to about 5 mL and 5 mL of pentane were layered: upon standing overnight at  $-30^\circ\text{C}$  the crystalline pale yellow precipitate that was formed, was filtered and dried *in vacuo* for 6 hours. Yield 0.684 g (67%). As an alternative purification procedure, the solvent was removed *in vacuo* and the solid obtained sublimed at  $125\text{-}130^\circ\text{C}$  bath temperature and  $10^{-1}$  mbar, recovering the product in 80% yield.  $^1\text{H}$  NMR ( $\text{CD}_2\text{Cl}_2$ ) at  $-40^\circ\text{C}$   $\delta$  4.63 (s,  $\text{CH}_3\text{NC}(\text{CH}_3)\text{CHC}(\text{CH}_3)\text{NCH}_3$ , 2H), 3.24 (s,  $\text{CH}_3\text{NC}(\text{CH}_3)\text{CHC}(\text{CH}_3)\text{NCH}_3$ , 6H), 2.93 (s,  $\text{N}(\text{CH}_3)_2$ , 12H), 2.47 (s,  $\text{CH}_3\text{NC}(\text{CH}_3)\text{CHC}(\text{CH}_3)\text{NCH}_3$ , 6H), 1.89 (s,  $\text{CH}_3\text{NC}(\text{CH}_3)\text{CHC}(\text{CH}_3)\text{NCH}_3$ , 6H), 1.68 (s,  $\text{CH}_3\text{C}(\text{CH}_3\text{N})\text{CHC}(\text{CH}_3\text{N})\text{CH}_3$ , 6H);  $^{13}\text{C}$  NMR  $\{^1\text{H}\}$  at  $-40^\circ\text{C}$   $\delta$  166.70, 162.56, 99.52, 46.19, 37.65, 36.83, 22.34, 22.14. Elemental anal. Calcd. for  $\text{C}_{18}\text{H}_{38}\text{N}_6\text{Zr}$ : C, 50.31; H, 8.77; N, 19.56. Found: C, 50.45; H, 8.88; N, 19.09. MS (EI+, 70 eV): 428 ( $\text{M}^+$ , 17), 384 ( $\text{M}^+ - \text{NMe}_2$ , 100), 340 ( $\text{M}^+ - 2\text{xNMe}_2$ , 38).

**Synthesis of  $\text{Zr}(\text{MeNacNac})_2(\text{Net}_2)_2$  (2):**  $\text{Zr}(\text{NEt}_2)_4$  (0.914, 2.41 mmol) was dissolved in 15 mL of toluene. To this solution the N-methyl-4-(methylimino)pent-2-

en-2-amine (0.608 g, 4.82 mmol) was added as a solid. The yellow solution was stirred at 90 °C for 25 h. The resulting deep red-brown solution was vacuum dried and the remaining solid dissolved in 25 mL of pentane. This solution was passed through a layer of celite, the filtrate was reduced to a volume of 10 mL and cooled to -30 °C. The crystalline solid of **2** was filtered and washed with 3 mL of cold pentane. Yield 0.526 g (45%). <sup>1</sup>H NMR (C<sub>6</sub>D<sub>6</sub>) δ 4.71 (s, CH<sub>3</sub>C(CH<sub>3</sub>N)CHC(CH<sub>3</sub>N)CH<sub>3</sub>, 2H), 4.01 (m, J = 6.9 Hz, N(CH<sub>2</sub>CH<sub>3</sub>)<sub>2</sub>, 8H), 3.66 (m, J = 6.9 Hz, N(CH<sub>2</sub>CH<sub>3</sub>)<sub>2</sub>, 8H), 3.38 (s, CH<sub>3</sub>C(CH<sub>3</sub>N)CHC(CH<sub>3</sub>N)CH<sub>3</sub>, 6H), 2.63 (s, CH<sub>3</sub>C(CH<sub>3</sub>N)CHC(CH<sub>3</sub>N)CH<sub>3</sub>, 6H), 1.76 (s, CH<sub>3</sub>C(CH<sub>3</sub>N)CHC(CH<sub>3</sub>N)CH<sub>3</sub>, 6H), 1.67 (s, CH<sub>3</sub>C(CH<sub>3</sub>N)CHC(CH<sub>3</sub>N)CH<sub>3</sub>, 6H), 1.18 (t, J = 7.0 Hz, N(CH<sub>2</sub>CH<sub>3</sub>)<sub>2</sub>). <sup>13</sup>C NMR {<sup>1</sup>H} δ 166.42, 162.3, 100.3, 42.85, 38.02, 37.37, 21.86, 21.64, 14.02. Elemental anal. calculated for C<sub>22</sub>H<sub>46</sub>N<sub>6</sub>Zr: C, 54.39; H, 9.54; N, 17.30; found: C, 54.72; H, 9.90; N, 16.94. MS (EI+, 70 eV): 412 (M<sup>+</sup> - NEt<sub>2</sub>, 15), 340 (M<sup>+</sup> - 2xNEt<sub>2</sub>, 25).

**Synthesis of Zr(MeNacac)<sub>2</sub>(NEt<sub>2</sub>)<sub>2</sub> (3).** Zr(NEt<sub>2</sub>)<sub>4</sub> (0.684g, 1.80 mmol) was dissolved in 20 mL of toluene. To this solution the ligand 4-(methylamino)pent-3-en-2-one (0.408g, 3.60 mmol) was added as a solid and the obtained yellow solution was stirred for 6h at room temperature. The solvent was removed under vacuum to obtain an oily residue: this was dissolved in 20 mL of pentane and filtered through celite. The filtrate was reduced to a volume of about 10mL and kept overnight at -30°C; the yellow crystalline product was filtered and dried under vacuum for 3 h. Yield 0.467g (57%). <sup>1</sup>H NMR (C<sub>6</sub>D<sub>6</sub>), δ 5.00 (s, CH<sub>3</sub>C(CH<sub>3</sub>N)CHC(CO)CH<sub>3</sub>, 2H), 3.58 (broad, N(CH<sub>2</sub>CH<sub>3</sub>)<sub>2</sub>, 8H), 2.86 (s, CH<sub>3</sub>C(CH<sub>3</sub>N)CHC(CO)CH<sub>3</sub>, 6H), 1.92 (s, CH<sub>3</sub>C(CH<sub>3</sub>N)CHC(CO)CH<sub>3</sub>, 6H), 1.42 (s, CH<sub>3</sub>C(CH<sub>3</sub>N)CHC(CO)CH<sub>3</sub>, 6H), 1.31 (t, J = 6.7 Hz), CH<sub>3</sub>C(CH<sub>3</sub>N)CHC(CO)CH<sub>3</sub>, 12H). <sup>13</sup>C NMR {<sup>1</sup>H} δ 170.65, 169.85, 103.53, 44.61, 37.41, 24.64, 21.12, 15.44. Elemental anal. calculated for C<sub>20</sub>H<sub>36</sub>O<sub>2</sub>N<sub>4</sub>Zr: C, 52.71; H, 7.96; N, 12.29; found: C, 52.64; H, 7.91; N, 11.92. MS (EI+, 70 eV): 429 (M<sup>+</sup> - Et, 65), 329 (M<sup>+</sup> - Et - MeC(MeN)CHC(O)Me), 25).

**Synthesis of Zr(<sup>i</sup>PrNacNac)(NMe<sub>2</sub>)<sub>3</sub> (4).** Zr(NMe<sub>2</sub>)<sub>4</sub> (1.428g, 5.34 mmol) was dissolved in 35 mL of toluene and to this the liquid ligand N-isopropyl-4-(isopropylimino)pent-2-en-2-amine was added. The stirred solution was warmed up to 90 °C for 22 h with the reaction vessel connected to an oil bubbler. The solvent was evaporated, leaving behind an oily residue that became a waxy solid after drying under vacuum for 5h. The <sup>1</sup>H NMR confirmed the quantitative conversion to the desired product. An analytically pure sample was obtained by sublimation at 5x10<sup>-4</sup> mbar, T = 130°C, cold finger at -20 °C. <sup>1</sup>H NMR (C<sub>6</sub>D<sub>6</sub>), δ 4.58 (s, CH<sub>3</sub>C(<sup>i</sup>PrN)CHC(<sup>i</sup>PrN)CH<sub>3</sub>, 1H), 3.62 (septet, J = 6.5 Hz, CH<sub>3</sub>C(CH(CH<sub>3</sub>)<sub>2</sub>N)CHC(CH(CH<sub>3</sub>)<sub>2</sub>N)CH<sub>3</sub>, 2H), 3.08 (s, N(CH<sub>3</sub>)<sub>2</sub>, 18H), 1.79 (s, CH<sub>3</sub>C(<sup>i</sup>PrN)CHC(<sup>i</sup>PrN)CH<sub>3</sub>, 6H), 1.13 (d, J= 6.4 Hz CH<sub>3</sub>C(CH(CH<sub>3</sub>)<sub>2</sub>N)CHC(CH(CH<sub>3</sub>)<sub>2</sub>N)CH<sub>3</sub>, 12H). <sup>13</sup>C {<sup>1</sup>H} NMR δ 160.05, 92.53, 51.50, 44.56, 24.01, 21.57. Elemental anal. calculated for C<sub>17</sub>H<sub>39</sub>N<sub>5</sub>Zr: C, 50.45; H, 9.71; N, 17.30; found C, 50.22; H, 10.01; N, 16.96. MS (EI+, 70 eV): 359 (M<sup>+</sup> - NMe<sub>2</sub>, 17), 315 (M<sup>+</sup> - 2xNMe<sub>2</sub>, 100), 271 (M<sup>+</sup> - 3xNMe<sub>2</sub>, 40), 228 (M<sup>+</sup> - 3xNMe<sub>2</sub> - <sup>i</sup>Pr, 16)

**Synthesis of Zr(MeNacnac)(NMeEt)<sub>3</sub> (5)** Zr(NMeEt)<sub>4</sub> (0.652 g, 1.90 mmoles) was dissolved in 10 ml of toluene, and the solution was stirred. The Menacnac ligand (0.240 g, 1.90 mmoles ) was dissolved in 10 ml of toluene and slowly added to the previous solution. The mixture was allowed to stir for 9 h, and the solvent was removed *in vacuo*. The residue was dried under vacuum for 3 hours. After that, it was redissolved in 15 ml of pentane, filtered over a 1 cm celite pad and dried under vacuum to leave a pale yellow liquid. Yield 0.730 g (98%). <sup>1</sup>H NMR (C<sub>6</sub>D<sub>6</sub>) δ 4.86 (s, CH<sub>3</sub>NC(CH<sub>3</sub>)CHC(CH<sub>3</sub>)NCH<sub>3</sub>, 1H), 1.17 (s, CH<sub>3</sub>NC(CH<sub>3</sub>)CHC(CH<sub>3</sub>)NCH<sub>3</sub>, 6H), 2.98 (s, CH<sub>3</sub>NC(CH<sub>3</sub>)CHC(CH<sub>3</sub>)NCH<sub>3</sub>, 6H), 3.03 (s, NEtCH<sub>3</sub>, 9H), 1.19 (t, J = 7.0 Hz NCH<sub>2</sub>CH<sub>3</sub>Me, 6H), 3.35 (t, J = 7.0 Hz NCH<sub>2</sub>CH<sub>3</sub>Me, 9H); <sup>13</sup>C NMR {<sup>1</sup>H} δ 164.84, 99.66, 49.75, 38.55, 38.05, 21.67, 15.54. Anal. Calcd. for C<sub>16</sub>H<sub>37</sub>N<sub>5</sub>Zr: C, 49.18; H, 9.54; N, 17.92. Found: C, 49.40; H, 9.73; N, 18.03. MS (EI+, 70 eV): 343 (M<sup>+</sup>-NMeEt, 15), 285 (M<sup>+</sup> -2xNMeEt, 100).

**Synthesis of Zr(NacNac)<sub>4</sub> (Method a) (6).** The Hnacnac ligand (0.243g, 2.55 mmol) was dissolved in 5 mL of toluene; Zr(NMe<sub>2</sub>)<sub>4</sub> (0.163g, 0.612 mmol) was dissolved in 20 mL of toluene and was slowly added to the above solution. The mixture was stirred at room temperature for 4 h while the gaseous products were allowed to escape from the reaction flask. The solvent was subsequently removed *in vacuo*, leaving behind an oily residue that was treated with 5 mL of pentane: upon drying a bright yellow fluffy solid was left behind. The solid was re-dissolved in 10 mL of pentane and passed through celite. The yellow solution was concentrated to a volume of about 5 mL and kept at -25 °C overnight. The yellow crystalline precipitate was collected and dried *in vacuo*. Yield 0.139g (47%). <sup>1</sup>H NMR (C<sub>6</sub>D<sub>6</sub>), δ 6.79 (s, CH<sub>3</sub>C(NH)CHC(NH)CH<sub>3</sub>, 8H), 4.60 (s, CH<sub>3</sub>C(NH)CHC(NH)CH<sub>3</sub>, 4H), 1.80 (s, CH<sub>3</sub>C(NH)CHC(NH)CH<sub>3</sub>, 24H). <sup>13</sup>C NMR{<sup>1</sup>H} δ 163.78, 92.52, 27.73. Elemental analysis calculated for C<sub>20</sub>H<sub>36</sub>N<sub>8</sub>Zr: C, 50.07; H, 7.56; N, 23.36; found: C, 50.01; H, 7.82; N, 22.99. MS (EI+, 70 eV): 478 (M<sup>+</sup>, 20), 381 (M<sup>+</sup> - MeC(NH)CHC(NH)Me, 100), 284 (M<sup>+</sup> - 2xMeC(NH)CHC(NH)Me, 28).

**Synthesis of Zr(NacNac)<sub>4</sub> (Method b) (6), (Method b).** The ligand 4-iminopent-2-en-2-amine (0.858g, 8.76 mmol) was dissolved in 10 mL of diethylether and to this stirred solution, 5.4 mL of 1.6 M butyl lithium in Et<sub>2</sub>O (8.64 mmol) were added. The resulting solution was stirred for an hour, and the ZrCl<sub>4</sub>(thf)<sub>2</sub> (0.819g, 2.19 mmol) added as a solid. The yellow solution was allowed to stir for 4 h. The solvent was removed *in vacuo* and the solid thus obtained extracted with 3 x 10 mL of pentane, filtered and reduced to a volume of about 10 mL. After standing in the fridge for one night, bright yellow crystals were recovered. Yield 0.694 g (66%). The compound was identified by NMR spectroscopy.

**Synthesis of Zr(Nacac)<sub>4</sub> (7).** The 4-aminopent-3-en-2-one ligand (0.391g, 3.94 mmol) was dissolved in 5 mL of toluene and to this solution, a solution of Zr(NEt<sub>2</sub>)<sub>4</sub>

(0.374g, 0.984 mmol) dissolved in 10 mL of toluene, was slowly added. The pale yellow solution was stirred for 7 h and was then reduced to about 5 mL. After standing at  $-25\text{ }^{\circ}\text{C}$  overnight, the precipitate was filtered and the white solid washed with 5 mL of pentane and dried *in vacuo* for 4 h. Yield 0.450 g (94%). Elemental analysis calculated for  $\text{C}_{20}\text{H}_{32}\text{O}_4\text{N}_4\text{Zr}$  C, 49.66; H, 6.67; N, 11.58; found: C, 49.58; H, 6.73; N, 11.45;  $^1\text{H}$  NMR ( $\text{C}_6\text{D}_6$ ),  $\delta$  7.78 (s,  $\text{CH}_3\text{C}(\text{NH})\text{CHC}(\text{O})\text{CH}_3$ , 4H), 4.91 (s,  $\text{CH}_3\text{C}(\text{NH})\text{CHC}(\text{O})\text{CH}_3$ , 4H), 2.06 (s,  $\text{CH}_3\text{C}(\text{NH})\text{CHC}(\text{O})\text{CH}_3$ , 12H), 1.53 (s,  $\text{CH}_3\text{C}(\text{NH})\text{CHC}(\text{O})\text{CH}_3$ , 12H).  $^{13}\text{C}$  NMR $\{^1\text{H}\}$   $\delta$  178.16, 168.09, 97.49, 26.93, 26.72. MS (EI+, 70 eV): 384 ( $\text{M}^+$  -  $\text{MeC}(\text{NH})\text{CHC}(\text{O})\text{Me}$ , 100), 98 ( $(\text{MeC}(\text{NH})\text{CHC}(\text{O})\text{Me})^+$ , 55).

**Synthesis of (3Z)-5-imino-2,2,6,6-tetramethylhept-3-en-3-amine (HNThd, 8).** Freshly crystallized  $\text{Cp}_2\text{TiMe}_2$  (3.69 g, 17.7 mmoles) was dissolved in 100 ml of dry benzene. Tert-butylacetonitrile (1.47 g, 17.7 mmoles) was added with a syringe and the solution was warmed to  $60\text{ }^{\circ}\text{C}$ : the color changed from orange to deep red and to brown in about 1 hour. The solution was stirred for at least 4 days at  $60\text{ }^{\circ}\text{C}$ . At the end of this period the solution was dried *in vacuo*, and the remaining product extracted with pentane (2x40 ml), and filtered. The filtrate was collected and dried *in vacuo*. The brown solid was subsequently dissolved in diethyl ether and 1M HCl in  $\text{Et}_2\text{O}$  (5.4 ml, 5.4 mmoles) was added with a syringe, causing the suspension to turn to a deep green color. After 1 h of stirring the solvent was removed *in vacuo*, the residue transferred into a sublimator and sublimed at  $55\text{ }^{\circ}\text{C}$ , 0.1 mbar. A very small amount of pure white crystalline compound was obtained Yield 0.0197 g (0.3 %).  $^1\text{H}$  NMR ( $\text{C}_6\text{D}_6$ ),  $\delta$  1.02 (s,  $(\text{CH}_3)_2\text{C}$ , 18 H), 5.04 (s,  $\text{CH}$ , 1 H).  $^{13}\text{C}$  NMR $\{^1\text{H}\}$   $\delta$  28.54, 37.56, 85.39, 175.00.

**Synthesis of (4Z)-5-amino-2,2,6,6-tetramethylhept-4-en-3-one (9).** Freshly prepared  $\text{Cp}_2\text{TiMe}_2$  (3.82g, 18.4 mmoles) was dissolved in 100 ml of dry benzene. Tert-butylacetonitrile (1.52g, 18.35 mmoles) was added with a syringe and the solution warmed to  $60\text{ }^{\circ}\text{C}$ : the color changed from orange to deep red and to brown in

about 1 hour. The solution was stirred for at least 4 days at 60 °C. At the end of this period, the solution was cooled to room temperature and an excess of Na<sub>2</sub>SO<sub>4</sub>·10H<sub>2</sub>O (8.0 g, 18 mmoles) was added. The suspension was stirred for an additional 12 hours, after which the solvent was removed to leave a deep green solid. This was dissolved in 40 ml of dichlorometane, passed over a celite pad, and the filtrate was again vacuum-dried. The solid obtained was subjected to sublimation at 70 °C, 0.1 mbar to give a white crystalline solid. Yield 1.075 g (65%). <sup>1</sup>H NMR (C<sub>6</sub>D<sub>6</sub>), δ 0.82 (s, (CH<sub>3</sub>)<sub>2</sub>C, 9 H), 1.80 (s, (CH<sub>3</sub>)<sub>2</sub>C, 9 H), 5.42 (s, CH, 1 H). <sup>13</sup>C NMR{<sup>1</sup>H} (CDCl<sub>3</sub>) δ 27.45, 28.4, 57.27, 125.03, 205.81. Elemental analysis calculated for C<sub>22</sub>H<sub>52</sub>N<sub>8</sub>Zr C, 72.08; H, 11.55; N, 7.64; found: C, 71.98; H, 10.98; N, 7.68

**Synthesis of Zr(Nthd)<sub>4</sub> (10).** The very small amount of compound **8** synthesized (0.0197g, 0.11 mmoles), was dissolved in 2 ml of Et<sub>2</sub>O in the glove box. To this solution 0.07 ml of 1.6 M BuLi (0.11 mmoles) was added. After stirring for 15 minutes, ZrCl<sub>4</sub>thf<sub>2</sub> (0.0102 g, 0.027 mmoles) was added as a solid to obtain a yellow suspension, which was stirred for 12 h. After this period, the solvent was removed *in vacuo*, and the product extracted with 5 ml of toluene, filtered through a 0.5 cm celite pad, and dried under vacuum. Upon drying, a yellow oil forms which becomes fluffy as soon as it is dry. The product is dissolved in a minimum amount of pentane and stored in the fridge at -30 °C. The small crystallites recovered were just enough for an NMR and for X-ray crystallography. <sup>1</sup>H NMR (C<sub>6</sub>D<sub>6</sub>), δ 1.19 (s, (CH<sub>3</sub>)<sub>2</sub>C, 64 H), 4.98 (s, CH, 8 H), 6.99 (s, NH, 8 H). For further characterization, see the X-ray crystallography section.

**Synthesis of Zr(ONthd)<sub>4</sub> (11).** Compound **9** (0.440 g, 2.43 mmoles) was dissolved in 15 ml of Et<sub>2</sub>O in the glove box. To this solution, 1.55 mL of 1.6 M BuLi (2.20 mmoles) was slowly added. After stirring for 40 minutes, ZrCl<sub>4</sub>thf<sub>2</sub> (0.229 g, 0.606 mmoles) dissolved in 10 ml of Et<sub>2</sub>O, was added, to obtain a yellow suspension,

which was stirred for 1 and ½ hours. After this period, the solvent was removed *in vacuo*, and the product was extracted with 2x10 mL of toluene, filtered through a 0.5 cm celite pad, and concentrated to 8 mL. After 1 day standing in the freezer at -30 °C, a white microcrystalline precipitate was collected, washed with 5 ml of pentane, and dried *in vacuo*. Yield 0.312 g (63%). <sup>1</sup>H NMR (C<sub>6</sub>D<sub>6</sub>), δ 1.10 (s, (CH<sub>3</sub>)<sub>2</sub>C, 36 H), δ 1.37 (s, (CH<sub>3</sub>)<sub>2</sub>C, 38 H), δ 5.34 (s, CH<sub>3</sub>, 8 H), δ 8.09 (s, NH, 8 H). <sup>13</sup>C NMR{<sup>1</sup>H} δ 28.77, 29.27, 38.39, 39.11, 88.37, 177.85186.02. Elemental analysis calculated for C<sub>44</sub>H<sub>80</sub>N<sub>4</sub>O<sub>4</sub>Zr C, 64.42; H, 9.83; N, 6.95; found: C, 65.31; H, 10.86; N, 6.95

**Synthesis of compound Zr(<sup>i</sup>Pr-guanidinato)<sub>2</sub>(NMe<sub>2</sub>)<sub>2</sub> (12).** The reaction was carried out in the glove-box. To a solution of Zr(NMe<sub>2</sub>)<sub>4</sub> (0.140 g, 0.525 mmoles) in 10 ml of toluene, diisopropylcarbodiimide (0.138 g, 1.10 mmoles) was added slowly as a liquid. The clear, colorless reaction mixture was stirred at room temperature for 2 hours. The solvent was removed *in vacuo* to leave a white crystalline solid that was dried for 2 hours. The solid was dissolved in 5 mL of ether, passed through a 1cm thick celite plug and the solution collected reduced to a volume of about 3 mL. After overnight standing in the fridge, a white crystalline precipitate was collected and dried under vacuum. Yield 0.267 g (98%). <sup>1</sup>H NMR (C<sub>6</sub>D<sub>6</sub>), δ 1.27 (d, (CH<sub>3</sub>)<sub>2</sub>CH, J= 6.15 Hz, 24 Hz), δ 2.52 (s, N(CH<sub>3</sub>)<sub>2</sub>, 12 H), δ 3.33 (s, N(CH<sub>3</sub>)<sub>2</sub>, 12 H), δ 3.63 (sept, (CH<sub>3</sub>)<sub>2</sub>CH, 4 H). <sup>13</sup>C NMR{<sup>1</sup>H} δ 25.05, 39.80, 46.88, 47.15, 172.26. Elemental analysis calculated for C<sub>22</sub>H<sub>52</sub>N<sub>8</sub>Zr C, 50.82; H, 10.08; N, 21.55; found: C, 51.02; H, 10.84; N, 21.73. MS (EI+, 70 eV): 519 (M<sup>+</sup>, 27), 474.3 (M<sup>+</sup> - NMe<sub>2</sub>, 100), 348.1 (M<sup>+</sup> - <sup>i</sup>PrNC(NMe<sub>2</sub>)N<sup>i</sup>Pr).

**Synthesis of compound Zr(<sup>i</sup>Pr-guanidinato)<sub>2</sub>(NEt<sub>2</sub>)<sub>2</sub> (13).** The reaction was carried out in the glove-box. To a solution of Zr(NEt<sub>2</sub>)<sub>4</sub> (0.198 g, 0.521 mmoles) in 10 mL of toluene, diisopropylcarbodiimide (0.132 g, 1.04 mmoles) was added slowly as a neat liquid. The clear colorless reaction mixture was stirred at room temperature for 17 hours. The solvent was removed *in vacuo* to leave a white crystalline solid that was dried for 3 hours. The solid was dissolved in 5 mL of pentane, and stored in the

fridge at  $-20\text{ }^{\circ}\text{C}$ . After overnight standing in the fridge a white crystalline precipitate was collected and dried under vacuum. Yield 0.204 g (78%).  $^1\text{H}$  NMR ( $\text{C}_6\text{D}_6$ ),  $\delta$  0.97 (t,  $\text{CH}_3\text{CH}_2\text{N}$ ,  $J = 7.09$  Hz),  $\delta$  2.52 (s,  $\text{N}(\text{CH}_3)_2$ , 12 H),  $\delta$  3.33 (s,  $\text{N}(\text{CH}_3)_2$ , 12 H),  $\delta$  3.63 (sept,  $(\text{CH}_3)_2\text{CH}$ , 4 H).  $^{13}\text{C}$  NMR $\{^1\text{H}\}$   $\delta$  13.61, 15.50, 24.31, 24.95, 25.77, 25.85, 26.13, 42.37, 43.15, 44.48, 47.32, 47.75, 171.76. Elemental analysis calculated for  $\text{C}_{30}\text{H}_{68}\text{N}_8\text{Zr}$  C, 57.00; H, 10.84; N, 17.73; found: C, 56.62; H, 10.62; N, 17.35. MS (EI+, 70 eV): 630.9 ( $\text{M}^+$ , 3), 558.2 ( $\text{M}^+ - \text{NMe}_2$ , 70), 432.1 ( $\text{M}^+ - \text{iPrNC}(\text{NEt}_2)\text{N}^i\text{Pr}$ ).

**Synthesis of compound  $\text{Zr}(\text{SiMe}_3\text{guanidinato})(\text{NMe}_2)_3$  (14).**  $\text{Zr}(\text{NMe}_2)_4$  (0.491 g, 1.83 mmoles) was dissolved in 10 mL of pentane in the glove-box. Bis-trimethylsilylcarbodiimide (0.342 g, 1.83 mmoles) dissolved in 5 ml of pentane was added and the mixture was stirred for 22 hours at room temperature. The mixture was filtered over 2 cm of celite and the solvent removed *in vacuo* to leave a yellow oil, dried under vacuum for 3 hours. Yield 0.800 g (96%).  $^1\text{H}$  NMR ( $\text{C}_6\text{D}_6$ ),  $\delta$  0.22 (s,  $\text{Si}(\text{CH}_3)_3$ , 6 H),  $\delta$  2.53 (s,  $\text{N}(\text{CH}_3)_2$ , 18 H),  $\delta$  3.09 (s,  $\text{N}(\text{CH}_3)_2$ , 6 H).  $^{13}\text{C}$  NMR $\{^1\text{H}\}$   $\delta$  2.95, 39.71, 43.23, 167.86. Elemental analysis calculated for  $\text{C}_{15}\text{H}_{42}\text{N}_6\text{Si}_2\text{Zr}$  C, 39.69; H, 9.33; N, 18.51; found: C, 39.90; H, 9.98; N, 18.12.

**Synthesis of compound  $(^i\text{Pr}\text{guanidinato})_2\text{Zr}(\mu\text{-N}^i\text{Bu})_2\text{Zr}(\text{HN}^i\text{Bu})_2$  (15).** Bis( $\mu$ -*tert*-butylamido)tetrakis(*tert*-butylamido)dirirconium (0.155 g, 0.252 mmoles) was dissolved in 15 mL of toluene. Isopropylcarbodiimide (0.127g, 1.01 mmoles) was added as a liquid and the yellow solution was stirred for 20 h at room temperature. The solvent was removed *in vacuo* leaving behind a pale-yellow solid that was crystallized in pentane at  $-30\text{ }^{\circ}\text{C}$ . Yield: 0.213 g (98 %).  $^1\text{H}$  NMR ( $\text{C}_6\text{D}_6$ ),  $\delta$  1.81, 1.55, 1.34, 1.26, (doublets,  $(\text{CH}_3)_2\text{CH}$ ,  $J = 6.46$  Hz, 3H each),  $\delta$  1.25 (s,  $\text{C}(\text{CH}_3)_2$ , 9 H),  $\delta$  1.50 (s,  $\text{C}(\text{CH}_3)_2$ , 9 H),  $\delta$  1.64 (s,  $\text{C}(\text{CH}_3)_2$ , 9 H),  $\delta$  3.96 (m,  $\text{CH}(\text{CH}_3)_2$ ,  $J = 6.46$  Hz, 1



H),  $\delta$  3.36 (m,  $CH(CH_3)_2$ ,  $J = 6.46$  Hz, 1 H),  $\delta$  3.54 (s,  $NH$ , 1 H),  $\delta$  3.88 (s,  $NH$ , 1 H).  $^{13}C$  NMR{ $^1H$ }  $\delta$  24.08, 24.40, 24.57, 25.79, 26.01, 26.98, 31.23, 32.60, 35.50, 35.63, 45.88, 46.52, 47.37, 54.00, 60.29, 166.75. Elemental analysis calculated for  $C_{38}H_{86}N_{10}Zr_2$  C, 52.13; H, 10.01; N, 16.18; found: C, 51.89; H, 10.13; N, 16.57.

## 6.3 CVD experiments

### 6.3.1 CVD reactor.

The custom-built CVD reactor is depicted in Figure 6.1. It consists of a hydrogen carrier-gas-delivery assembly, an ammonia/nitrogen reactant gas delivery system, a helium/argon backfill line (not drawn), a precursor handling and evaporation system, and a cold-wall reactor connected to a pump stand and vacuum control unit with a gas-type independent capacitive pressure sensor..

All gas lines were made of 6x4 mm diameter stainless steel AISI 316L (DIN 1.4435) with Swagelock<sup>®</sup> fittings.

The hydrogen carrier used for precursor evaporation was 99.9999% pure. To further purify it, it was passed through a Merck Oxisorb<sup>®</sup> purifying system, specified by the manufacturer to remove oxygen to below 100 ppb. This gas line passed through a mass-flow controller labelled 1 (MFC1), and then to the evaporator. The ammonia/nitrogen reactant gas mixture contained about 9 % of ammonia: nitrogen was 99.999% pure and ammonia was UHP quality. This gas line was connected to the top of the cold-wall reactor. The helium/argon backfill line was connected to the bottom of the reactor, and was used to bring the reactor to atmospheric pressure after the deposition, and to keep it under inert atmosphere during the insertion of the substrate. The argon and helium used were both 99.9999 purity.

The mass-flow controllers (Brooks 5850S) were calibrated for helium flows (MFC 1, MFC 2) and nitrogen (MFC 3) and operated by a Brooks Model 0154 control and read-out unit. Full-scale values in the control-unit were adjusted to take into account of the real gases flowing through the mass-flow controller. This was achieved using gas-conversion factors<sup>[7]</sup> using the following formula for a given gas:

$$FS_2 = \frac{FS_1 CF_1}{CF_1}$$

where:

$FS_1$  full-scale value of calibration gas

$CF_1$  conversion factor of calibration gas vs. N<sub>2</sub>

$FS_2$  full scale value for the gas used

$CF_2$  conversion factor for the gas used

For a mixture of a gas A and B in the molar fraction  $M_A$  and  $M_B$  ( $M_A + M_B = 1$ ), the following formula was used to calculate the conversion factor  $CF_{AB}$  for the mixture:

$$CF_{AB} = \frac{1}{\frac{M_A}{CF_A} + \frac{M_B}{CF_B}}$$

Using the result from the previous formulas, the full-scale value for gas mixture  $FS_{AB}$  can be calculated as:

$$FS_{AB} = \frac{FS_1 CF_{AB}}{CF_1} = \frac{FS_1}{CF_1 \left( \frac{M_A}{CF_A} + \frac{M_B}{CF_B} \right)_1}$$

The conversion factors employed are reported in Table 1. In Table 2 are reported the calibration gases used for the mass-flow controllers, the full scale tested with the calibration gases and the calculated full-scale values for the process gases employed.

**Table 1 Conversion factors for the gases used. For nitrogen the value equals 1.000**

gas	Conversion factor
Ammonia	0.788
Helium	1.389
Hydrogen	1.010
Nitrogen/ammonia 9/1	0.974

**Table 2 Mass-flow controllers employed, respective calibration gases, flow rates, and calculated flow-rates for the real gas passed through during the deposition experiments.**

controller	Calibration gas, full-scale value (sccm)	Gas flowing	Full-scale value (sccm)
MFC 1	He, 25	H <sub>2</sub>	18.18
MFC 2	He, 150	H <sub>2</sub>	109.07
MFC 3	N <sub>2</sub> , 60	N <sub>2</sub> /NH <sub>3</sub> 9:1	58.45

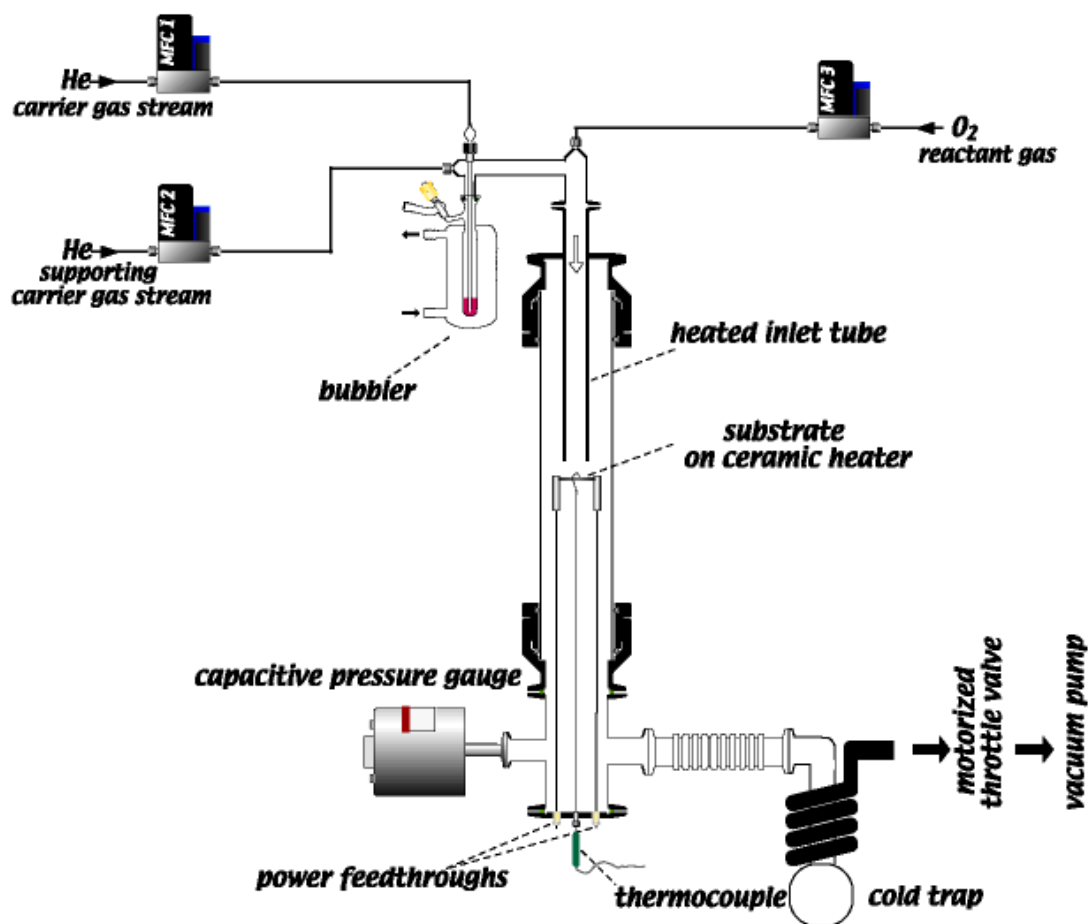


Figure 6.1 Scheme of the CVD reactor.

The solid precursor evaporator employed consisted of a Young-capped double wall glass tube, in a fixed-bed-type arrangement, where the precursor was mixed together with silica or alternatively Pyrex sand. The evaporator was filled in the glove box, sealed and connected to the reactor under a stream of inert gas.

The cold-wall-reactor chamber consisted of a cylindrical tube made out of fused silica with an inner internal diameter of 56 mm. On either side, the tube was connected with stainless-steel fittings and flanges. The substrate was placed on an Advanced Ceramics Boralectric<sup>®</sup> pyrolytic boron nitride coated graphite resistive

heater. A Balzers Prisma quadrupole mass-analyser was connected to the exit of the reactor in order to determine the low-molecular weight species formed during the deposition process.

Prior to all deposition experiments the reactor was baked under vacuum, using heating tapes and a hot-air fan to remove adsorbed water. The loading of the wafer was performed under a helium or argon counter-flow, and subsequently the substrate was warmed to 200-350 °C under vacuum to remove residual moisture.

After the baking procedure, the evaporator and the substrate temperature were set to the desired values, the reactor was brought to the desired pressure choosing the proper value for the throttle valve, and the system was allowed to equilibrate under an inert gas flow through the reactor. Shortly before the desired temperatures for the evaporator, heating tapes and substrate were reached, the MFC 3 was switched on to allow the reactor to saturate with the reactant ammonia/nitrogen mixture. After about 3 minutes it was established with the mass spectrometer that the reactor was filled up with the reactant gas mixture. The flow rate of the reactant gas was set to the desired value, and the deposition process was started by switching on the MFC 1, and opening the Young valve on top of the evaporator. The deposition time was measured with a chronometer and was, in all experiments, about 30 minutes.

At the end of the deposition, the carrier-gas mass-flow controller was switched off, the evaporator Young cap was shut off, and after about 3 minutes the heating of the substrate was stopped: this short period of time allowed the residue of precursor left in the reactor to be completely consumed. At the same time the cooling of the evaporator heating fluid was accelerated by flowing cold water through a serpentine dipped into the heating controller.

### 6.3.2 Experimental details about CVD experiments

**Loading of the precursor.** SiO<sub>2</sub> sand was carefully dried overnight in the oven at 120 °C and subsequently allowed to cool down under dynamic vacuum in a Schlenk tube for 3 h. The precursor was diluted with this in the glove box. The amount of precursor used ranged from 1 g to 1.2 g and the amount of SiO<sub>2</sub> was about 3 g.

**Silicon wafers.** Single-side-polished Si <100> silicon wafers were purchased from Virginia Semiconductors Inc. (Fredericksburg, VA 22401, USA) The thickness was 0.4 mm and the diameter 25.5 mm. They were cleaned by dipping into a piranha solution for 1 minute and were subsequently etched with 3% hydrofluoric acid for 1 minute, rinsed with water and dried with a stream of Argon or helium.

### 6.4 Vapor pressure measurements.

Vapor pressure was measured in a self-built apparatus Figure 6.2. The method employed is called the gas-saturation (also called “flow”) method, which operates at ambient pressure and is especially suited to air-sensitive compounds. In this method, a known amount of carrier gas is saturated by passing it over the substance at a given constant temperature. Later, the substance is re-condensed in a cold zone or trap, and the carrier gas leaves towards the vent. The vapor pressure of the substance is then calculated using the following equation:

$$P = \frac{n_v P_{tot}}{n_v + n_c}$$

where  $P$  = sample vapor pressure,  $P_{tot}$  = total pressure,  $n_v$  = moles of sample transported in time  $t$ ,  $n_c$  = moles of carrier gas transported in time  $t$ . The total pressure and moles of substance are directly measured, whereas the number of carrier gas

moles can be calculated from the measured flow rate  $Q$ , the time  $t$  and the molar volume  $V_m$  according to the following relation:

$$n_c = \frac{Q \cdot t}{V_m}$$

Usually, simple weight gain or weight loss is used to determine the amount of evaporated material and thus  $n_v$ . We have enhanced the method by using ICP-AES (inductively coupled-atomic emission spectroscopy) for quantification. Thereby, only metal-containing species are detected, which not only eliminates the problem with volatile ligands cleaved by thermal or hydrolysis decomposition during the measurements, but also greatly enhances sensitivity, thus allowing one to measure vapor pressures down to the  $10^{-3}$  mbar range within a reasonable time scale. The total absolute pressure is measured with a MKS Baratron with a capacitive pressure gauge linked to LabVIEW computer software, and the pressure is averaged over the time of measurement. The nitrogen flow was maintained at 7 sccm (standard cubic centimetres/minute) by a Brooks 5850S mass flow controller. The exact evaporation temperature was recorded by a Pt 100 (4-wire) element placed in the equilibrium zone of the evaporator



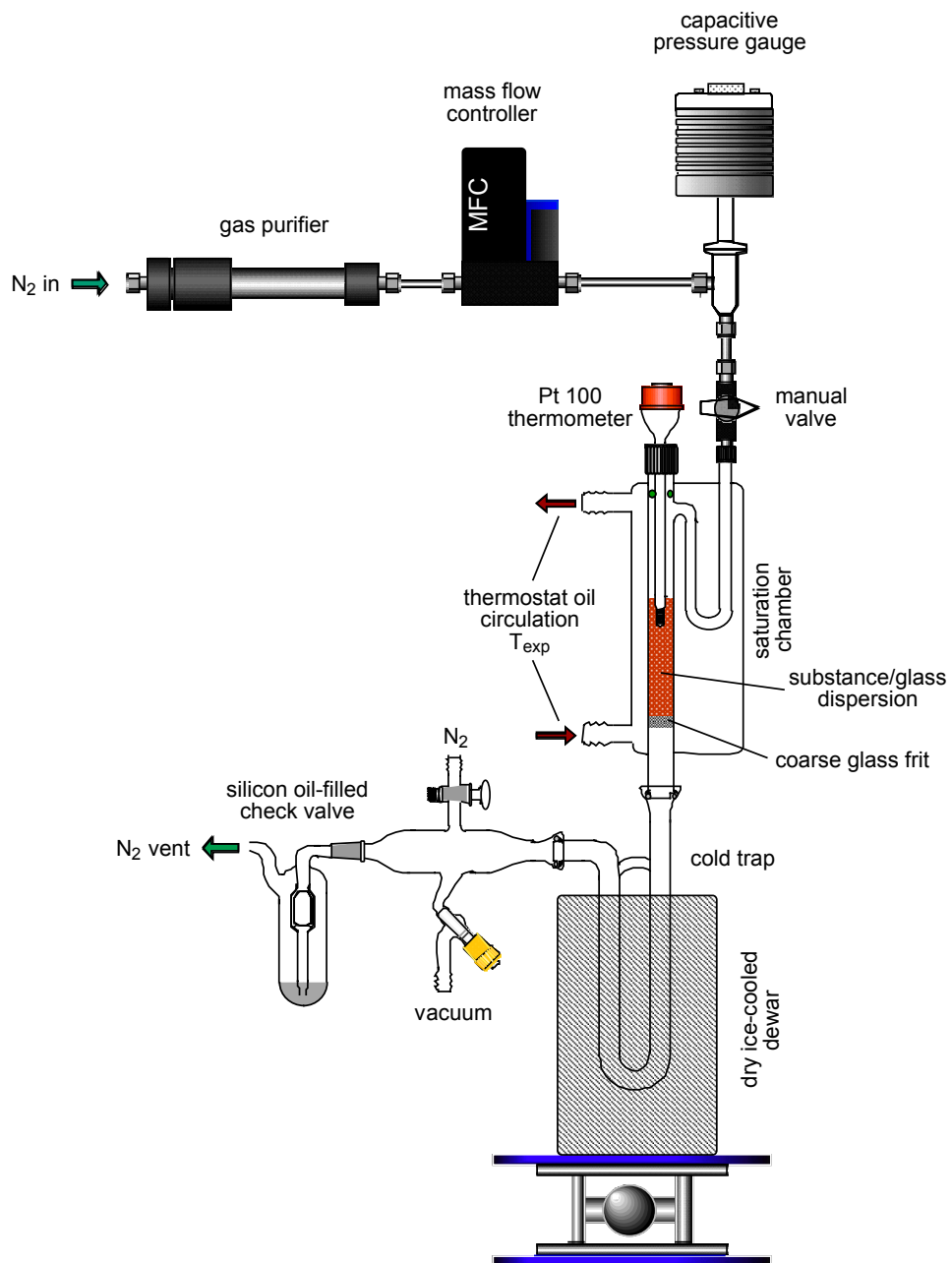


Figure 6.2: Experimental set up for vapor pressure measurements.

## 6.5 Film Characterization

### 6.5.1 XPS analysis.

XPS spectra were recorded using a Physical Electronics PHI 5400 XPS instrument using Al K $\alpha$  irradiation and a pass energy of 17.9 eV. A rastered, differentially pumped, ion gun (Ar<sup>+</sup>) was used for the sputtering.

The quantitative analysis and curve fitting of the signals was performed using the CasaXPS<sup>®</sup> software<sup>[8]</sup>. The spectra were fitted with mixed Gaussian-Lorentzian product functions (Gaussian contribution 85%). In the Zr 3d fittings, the difference between the 3d<sub>5/2</sub> and 3d<sub>3/2</sub> was kept constant at 2.34 eV, and the ratio between the areas 3:2. The atomic concentration of the element  $j$  was calculated with the following formula:

$$X_j = \frac{I_{ij} / S_{ij}}{\sum_j I_{ij} / S_{ij}}$$

where  $I_{ij}$  is the area of the peak  $i$  of the element  $j$ , and  $S_{ij}$  is the relative sensitivity factor

The relative sensitivity factors were calculated using a first principle method, therefore the  $S_{ij}$  is given by:

$$S_{ij} = \sigma_{ij} \times \Lambda_{ij}(KE, \vartheta) \times T(KE)$$

where  $\sigma_{ij}$  is the calculated Scofield ionisation cross <sup>[9]</sup>,  $\Lambda_{ij}$  is the attenuation length (measured in nm) corrected for the emission angle ( $\theta = 45^\circ$ , unless otherwise stated), and is given by:

$$\Lambda_{ij} = \frac{A}{KE} + B \times \sqrt{KE} \times \cos \vartheta$$

where the values  $A$  and  $B$  for inorganic substances are 641 and 0.096, respectively.

$T(KE)$  is the transmission function of the analyser, which is a function of  $KE$ , the kinetic energy of the emitted photoelectrons and has the following functional form:

$$T(KE) = \left( \frac{a^2}{a^2 + R^2} \right)^b$$

where  $a$  and  $b$  are constants determined by reference measurements, and  $R$  (called retard ratio) is defined as  $KE/E_p$ , where  $E_p$  is the pass energy. The measured value of  $a$  and  $b$  are 18.376 and 0.49948. All the parameters discussed above are summarized in Table 3.

**Table 3: Transmission function, Scofield cross-section, attenuation factor and relative sensitivity factors used for the quantitative XPS analysis.**

Element	T(KE)	$\sigma$	$\Lambda$ (nm)	S
C1s	0.264	1	3.33054973	0.62185137
N1s	0.2892	1.8	3.17042957	1.16702736
O1s	0.3257	2.93	2.96894933	2.00361941
Zr3d	0.2449	7.04	3.46755865	4.22693711

## 6.6 X-ray Crystal Structure Analyses.

The experimental procedures described here apply for all the structures analysed, although some special comments are introduced regarding compound **1,2,3** and **6**. The X-ray diffraction data were collected at 183(1) K for compounds **2**, **3**, **6** and at 153(1) K for **1** using an imaging plate detector system (Stoe IPDS) with graphite monochromated Mo K $\alpha$  radiation. A total of 182, 200, 167, and 180 images were exposed at constant times of 1.50, 6.00, 2.00, and 3.00 min/image for the structures of **1**, **2**, **3**, and **6**, respectively. The crystal-to-image distances were set to 50 mm for compounds **1**, **2**, and **3** and to 60 mm for **6**. ( $\theta$ -max = 28.01° to 30.34°).  $\phi$ -rotation (**1**, and **4**) or oscillation modes (**2** and **6**) were used for the increments of 1.1, 1.0, 1.2, and 0.9° per exposure in each case. Total exposure times were 17, 34, 17, and 24 h.

The intensities were integrated after using a dynamic peak-profile analysis, and an estimated mosaic spread (EMS) check was performed to prevent overlapping intensities. A total of 8000 (7998 for **2**) reflections were selected out of the whole limiting sphere with intensities  $I > 6\sigma(I)$  for the cell-parameter refinement.

A total of 25106, 30158, 12051, and 34685 reflections were collected, of which 6455, 7723, 3747, and 11545 were unique ( $R_{\text{int}} = 3.93\%$ , 9.00%, 3.63%, and 12.13%) after data reduction. For the numerical absorption correction, 16, 15, 18, and 9 indexed crystal faces were used.

In general, the structures were solved with an incomplete data set while the measurement was still being performed, just to confirm the proposed chemical formula, or otherwise to find potential additional solvent molecules that had co-crystallised with the compound under investigation. The corrected formula was then used for the final numerical absorption correction. All these procedures were calculated by using the Stoe IPDS software, Version No. 2.92 (1999).

The structures of **1**, **2**, and **4** were solved with the merged unique data set after checking for correct space groups. The structure of **6** appeared to be more difficult to solve. Two steps were necessary to determine the correct space group  $P2_1/n$

because weak reflections of a  $\lambda/2$ -effect have been misinterpreted as belonging to a possible superstructure. The initial triclinic unit cell parameters were  $a=16.5519(11)$ ,  $b=22.3940(18)$ ,  $c=30.1835(22)$  Å,  $\alpha=69.656(8)$ ,  $\beta=89.998(8)$ ,  $\gamma=68.350(8)^\circ$ . The structure could be solved in space group P-1 having 232 non-H atoms in the refinement, representing eight independent molecules in the asymmetric unit of the cell. Higher symmetry between molecules were observed. Thus the cell had to be transformed to a monoclinic C-lattice with cell parameters  $a=41.628(4)$ ,  $b=16.5519(11)$ ,  $c=30.184(2)$  Å,  $\beta=111.96(8)^\circ$ , by using the matrix  $(-1, 1, 0; -1, 0, 0; 1, -1, 1)$ .

As the space group was expected to be centrosymmetric, C2/c and C2/m were initially used to solve the structure, albeit with no success. Thus the non-centrosymmetric space groups C2, Cc and Cm have also been checked, but the refinement of the resulting models failed. Then the structure was correctly solved in space group C-1, with eight independent complexes in the asymmetric unit, which was the same situation as with the triclinic space group P-1. Inspection of the crystal packing for the C-lattice showed that molecules along the b-axis were translationally equivalent. This was the evidence that a  $\lambda/2$  effect has been overlooked. The procedure was then repeated using  $b=8.276$  Å, a P-lattice and the transformation matrix  $(-0, 5, 1, 0; -0.5, 0, 0; 0.5, -1, 1)$ . This lattice was examined for higher symmetry with the program LePAGE, and another transformation was necessary for the finally used monoclinic unit cell, resulting in space group P2<sub>1</sub>/n. The structure was solved again and only two independent complexes remained for the refinement. This information was used to repeat the integration of the data and the absorption correction resulting in a reduced number of reflections. It should be noted that only 36% of the 11545 unique reflections represent significant data with  $I > 2s(I)$ , i.e., with the consequence that the measurement errors of the weak reflections, which are much larger than those for the observed data, may be responsible for the relatively bad  $R_{\text{int}}$  and  $R_{1\text{alldata}}$ -values of 0.1213 and 0.1788, respectively.

The Patterson method was used to solve the crystal structures by applying the software options of the program SHELXS-97. All structure refinements were

performed with the program SHELXL-97. Further programs used: PLATON, PLUTON (Spek, 1990, 1997).

**Table 4. Crystallographic data for 1 and 2**

$$R1 = \sum (F_o - F_c) / \sum F_o; I > 2\sigma(I) \quad wR2 = \left\{ \sum w(F_o^2 - F_c^2)^2 / \sum w(F_o^2)^2 \right\}^{1/2}$$

	<b>1</b>	<b>2</b>
formula	C <sub>18</sub> H <sub>38</sub> N <sub>6</sub> Zr	C <sub>22</sub> H <sub>46</sub> N <sub>6</sub> Zr
color	Colorless	colorless
crystal dimensions (mm)	0.46x0.36x0.24	0.27x0.23x0.16
crystal system	monoclinic	monoclinic
space group (No.)	P2 <sub>1</sub> /n (14)	P2 <sub>1</sub> /n (14)
<i>a</i> (Å)	9.9555(6)	9.3361(5)
<i>b</i> (Å)	13.3024(8)	14.3615(7)
<i>c</i> (Å)	16.7272(11)	19.6856(13)
$\alpha, \beta, \gamma$ (deg)	90.0, 100.539(7), 90.0	90, 99.084(7), 90
<i>V</i> (Å <sup>3</sup> )	2177.8(2)	2606.3(3)
<i>Z</i>	4	4
Fw	429.76	485.87
<i>d</i> (calcd) (g cm <sup>-3</sup> )	1.311	1.238
absorption coefficient (mm <sup>-1</sup> )	0.518	0.440
<i>F</i> (000)	912	1040
2 $\theta$ scan range (deg)	5.82 < 2 $\theta$ < 60.54	6.04 < 2 $\theta$ < 60.52
No. of unique data	6455	7723
No. of data obsd [ <i>I</i> > 2 $\sigma$ ( <i>I</i> )]	5225	5966
absorption correction	numerical, 16 crystal faces	numerical, 15 crystal faces
solution method	Patterson	Patterson
no. of parameters refined	238	275
<i>R</i> 1, <i>wR</i> 2 (%) all data	3.22, 7.43	7.47, 19.78
<i>R</i> 1, (obsd) (%) <sup>a</sup> )	2.44	6.36
goodness-of-fit	1.098	1.142

**Table 5. Crystallographic data for 3 and 6**

	<b>3</b>	<b>6</b>
Formula	C <sub>20</sub> H <sub>40</sub> N <sub>4</sub> O <sub>2</sub> Zr	C <sub>20</sub> H <sub>36</sub> N <sub>8</sub> Zr
Color	Pale-yellow	light-yellow
crystal dimensions (mm)	0.33×0.29×0.19	0.22×0.20×0.07
crystal system	monoclinic	Monoclinic
space group (No.)	C2/c (15)	P2 <sub>1</sub> /n (14)
a (Å)	9.5357(6)	20.8142(17)
b (Å)	15.7375(9)	8.2760(5)
c (Å)	16.7795(11)	29.569(2)
α,β,γ (deg)	90, 91.661(7), 90	90, 108.790(8), 90
V(Å <sup>3</sup> )	2517.0(3)	4822.1(6)
Z	4	8
Fw	459.78	479.79
d(calcd) (g cm <sup>-3</sup> )	1.213	1.322
absorption coefficient (mm <sup>-1</sup> )	0.456	0.478
F(000)	976	2016
2θ scan range (deg)	5.60 < 2θ < 60.68	5.14 < 2θ < 56.02
no. of unique data	3747	11545
no. of data obsd [ I  > 2σ(I)]	3046	4170
absorption correction	numerical, 18 crystal faces	numerical, 9 cryst. Faces
solution method	Patterson	Patterson
No. of parameters refined	128	539
R1, wR2 (%) all data	4.26, 6.82	17.88, 8.43
R1, (obsd) (%) <sup>a</sup>	2.98	6.90
goodness-of-fit	1.008	0.818



**Table 6. Crystallographic data for 10.**

	<b>10</b>
Color	Colorless
Empirical formula	C <sub>44</sub> H <sub>84</sub> N <sub>8</sub> Zr
Formula weight	852.49
Temperature	153(2) K
Wavelength	0.71073 Å
Crystal system, space group	Monoclinic, C2/c
a (Å)	48.710(3)
b (Å)	12.1164(11)
c (Å)	18.9227(10)
α (deg)	90.00
β (deg)	111.0004(6)
γ (deg)	90.00
Volume (Å <sup>3</sup> )	10425.8(13)
Z, Calculated density (mg/m <sup>3</sup> )	8, 1.086
Absorption coefficient (mm <sup>-1</sup> )	0.247
F(000)	3720
Crystal size	0.20 x 0.12 x 0.08 mm
Theta range for data collection	2.76 to 30.27 deg.
Limiting indices	-64 < h < 60, 0 < k < 16, 0 < l < 23
Reflections collected / unique	11931 / 1554 [R(int) = 0.0555]
Completeness to theta = 30.40	90.9%
Absorption correction	Numerical
Max. and min. transmission	0.966 and 0.983
Refinement method	Full-matrix least-squares on F <sup>2</sup>
Data / restraints / parameters	11931 / 17 / 519
Goodness-of-fit on F <sup>2</sup>	0.385
Final R indices [ >2σ (I)]	R1 = 0.0503, wR2 = 0.0864
R indices (all data)	R1 = 0.2723, wR2 = 0.1422

**Table 7. Crystallographic data for 12.**

<b>12</b>	
Color	Colorless
Empirical formula	C <sub>23.67</sub> H <sub>56</sub> N <sub>8</sub> Zr
Formula weight	543.98
Temperature	183(2) K
Wavelength	0.71073 Å
Crystal system, space group	Monoclinic, C2/c
a (Å)	19.9540(15)
b (Å)	29.7881(16)
c (Å)	17.6629(14)
α (deg)	90
β (deg)	116.575(8) deg.
γ (deg)	90 deg.
Volume (Å <sup>3</sup> )	9389.5(11)
Z, Calculated density (mg/m <sup>3</sup> )	12, 1.154
Absorption coefficient (mm <sup>-1</sup> )	0.375
F(000)	3528
Crystal size	0.65 x 0.65 x 0.42 mm
Theta range for data collection	2.91 to 30.40 deg.
Limiting indices	-28 < h < 25, 0 < k < 42, 0 < l < 25
Reflections collected / unique	14068 / 14068 [R(int) = 0.0890]
Completeness to theta = 30.40	99.1 %
Absorption correction	Numerical
Max. and min. transmission	0.820 and 0.697
Refinement method	Full-matrix least-squares on F <sup>2</sup>
Data / restraints / parameters	14068 / 0 / 463
Goodness-of-fit on F <sup>2</sup>	0.931
Final R indices [ $I > 2\sigma(I)$ ]	R1 = 0.0522, wR2 = 0.1473
R indices (all data)	R1 = 0.0717, wR2 = 0.1574
Extinction coefficient	0.00083(16)

**Table 8. Crystallographic data for 13.**

<b>13</b>	
Color	Colorless
Empirical formula	C <sub>30</sub> H <sub>68</sub> N <sub>8</sub> Zr
Formula weight	632.14
Temperature	183(2) K
Wavelength	0.71073 Å
Crystal system, space group	Monoclinic, P 21/c
a (Å)	10.5715(5)
b (Å)	39.0592(17)
c (Å)	18.4391(9)
α (deg)	90 deg.
β (deg)	94.408(5) deg.
γ (deg)	90 deg.
Volume (Å <sup>3</sup> )	7591.2(6)
Z, Calculated density (mg/m <sup>3</sup> )	8, 1.106
Absorption coefficient (mm <sup>-1</sup> )	0.318
F(000)	2752
Crystal size	0.35 x 0.33 x 0.25 mm
Theta range for data collection	1.92 to 24.06 deg.
Limiting indices	-12 < h < 12, 0 < k < 44, 0 < l < 21
Reflections collected / unique	46498 / 11651 [R(int) = 0.0600]
Completeness to theta = 30.40	95.5%
Absorption correction	Numerical
Max. and min. transmission	0.9248 and 0.8969
Refinement method	Full-matrix least-squares on F <sup>2</sup>
Data / restraints / parameters	11651 / 9 / 703
Goodness-of-fit on F <sup>2</sup>	1.114
Final R indices [I > 2σ(I)]	R1 = 0.0607, wR2 = 0.1672
R indices (all data)	R1 = 0.0840, wR2 = 0.1758
Extinction coefficient	0.0008(4)

**Table 9. Crystallographic data for 15.**

<b>15</b>	
Color	Colorless
Empirical formula	C <sub>43</sub> H <sub>98</sub> N <sub>10</sub> Zr <sub>2</sub>
Formula weight	937.75
Temperature	183(2) K
Wavelength	0.71073 Å
Crystal system, space group	Triclinic, P -1
a (Å)	11.2748(10)
b (Å)	13.4399(11)
c (Å)	19.2228(16)
α (deg)	74.330(10)
β (deg)	86.837(11)
γ (deg)	73.917(10)
Volume (Å <sup>3</sup> )	2694.2(4)
Z, Calculated density (mg/m <sup>3</sup> )	2, 1.156
Absorption coefficient (mm <sup>-1</sup> )	0.423 mm
F(000)	1012
Crystal size	0.42 x 0.31 x 0.28 mm
Theta range for data collection	2.76 to 30.27 deg.
Limiting indices	-15 < h < 15, -17 < k < 18, 0 < l < 27
Reflections collected / unique	38165 / 14627 [R(int) = 0.0555]
Completeness to theta = 30.40	90.9%
Absorption correction	Numerical
Max. and min. transmission	0.9181 and 0.8795
Refinement method	Full-matrix least-squares on F <sup>2</sup>
Data / restraints / parameters	14627 / 0 / 497
Goodness-of-fit on F <sup>2</sup>	1.001
Final R indices [ >2σ (I)]	R1 = 0.0437, wR2 = 0.1042
R indices (all data)	R1 = 0.0783, wR2 = 0.1134

## Refecences

- [1] L. E. Manzer, *Inorg. Synth.* **1982**, 21, 135.
- [2] G. M. Diamond, S. Rodewald, R. F. Jordan, *Organometallics* **1995**, 14, 5.
- [3] G. M. Diamond, R. F. Jordan, J. L. Petersen, *Organometallics* **1996**, 15, 4030.
- [4] H. F. Holtzclaw, J. P. Collman, R. M. Alire, *J. Am. Chem. Soc.* **1958**, 80.
- [5] M. E. F. Braibante, H. S. Braibante, L. Missio, Y. Andricopulo, *Synthesis* **1994**, 898.
- [6] S. G. McGeachin, *Can. J. Chem.* **1968**, 46, 1903.
- [7] Brooks, Instrument, document, J-836-D508.
- [8] CasaXPS Version 2.0.73. N. Fairley, 1999-2002.
- [9] J. H. Scofield, *J. Electron Spectrosc. Relat. Phenom.* **1976**, 8, 129.

## 7. CONCLUSIONS AND OUTLOOK

The focus of the first part of this thesis was the possibility of obtaining zirconium-based metal-organic complexes, designed to be suitable as MOCVD precursors. A first step in this direction was the development of the chemistry of alkyl-substituted  $\beta$ -diketimines. It was found that amide substitution reactions are convenient routes to obtain heteroleptic five- and six-coordinate complexes with  $\beta$ -ketoiminate and  $\beta$ -diketimate ligands bearing alkyl substituents on the imino-nitrogen. The steric bulk of both the N-substituent of the  $\beta$ -diketamine molecule, and of the alkyl group R in the  $Zr(NR_2)_4$  complex, is the key to understanding the reactivity of these systems. If the imino substituent is a methyl (HMeNacNac ligand), the reaction proceeded smoothly to yield compound  $Zr(MeNacNac)_2(NMe_2)_2$  (**1**) in high yields. When  $Zr(NEt_2)_4$  is used, the reaction to produce  $Zr(MeNacNac)_2(NEt_2)_2$  (**2**) is slower and requires higher temperature as a result of the higher steric bulk of the educt. The six-coordinate compound  $Zr(MeNacac)_2(NEt_2)_2$  (**3**) was isolated, but appeared to be too thermally unstable for any of the applications under consideration.

Steric effects are again the key factors determining the possibility of obtaining five-coordinate compounds of the type  $Zr(iPrNacNac)(NMeEt)_3$  (**4**) and  $Zr(MeNacNac)(NMeEt)_3$  (**5**).

Six-coordinated complexes cannot be obtained using  $\beta$ -diketimines bearing hydrogen on the imido nitrogen. If HNacac or HNacNac are employed, homoleptic eight-coordinate compounds of the type  $Zr(HNacNac)_4$  (**6**) or  $Zr(HNacac)_4$  (**7**), can be synthesized. It was attempted to extend the series of eight-coordinate compounds using <sup>t</sup>Butyl-substituted ligands such as HNthd (**8**). This ligand and the corresponding eight-coordinate complex  $Zr(Nthd)_4$ , seemed particularly appropriate, since the coordination sphere around the zirconium is completely saturated by nitrogen, and there is a sort of “hydrophilic barrier” around the molecule, formed by the peripheral <sup>t</sup>Butyl groups, which could prevent side reaction with water or oxygen. Unfortunately,

all efforts to obtain the ligand H<sub>2</sub>Nthd in reasonable quantities were unsuccessful. Only very small amounts of **8** could be used, at least enough to ascertain the possibility of obtaining the desired complex Zr(Nthd)<sub>4</sub> (**10**), and maybe motivate future efforts to investigate more thoroughly other routes to the synthesis of this ligand.

Among the  $\beta$ -diketiminato-based complexes, **1** and **2** display sufficient volatility and thermal stability to be considered as precursors for chemical vapor deposition, but the most convenient one, considering the yield of the reaction, is certainly **1**. All five-coordinate compounds were insufficiently volatile. The eight-coordinate homoleptic compound **6** is also worthy of consideration: it is certainly attractive as a CVD precursor due to its structural characteristics, although its volatility is at the limit for being interesting for these applications. In addition to that, problems were encountered in the scaling-up of the synthesis of the starting ligand H<sub>2</sub>NacNac, which is extremely moisture sensitive and malodorous. These were some additional reasons leading to search for alternatives, such as compound **10** (see above).

Investigations into the chemistry of guanidinato-based complexes were also carried out. They present some attractive characteristics. For instance, the starting material requires no preparation, and all complexes were obtained in very high yields. Six-coordinate compounds such as Zr(<sup>i</sup>Prguanidinato)<sub>2</sub>(NMe<sub>2</sub>)<sub>2</sub> (**12**) and Zr(<sup>i</sup>Prguanidinato)<sub>2</sub>(NEt<sub>2</sub>)<sub>2</sub> (**13**) can be obtained in good yields. As in the case of diketiminates, the possibility of tuning the coordination geometry around the metal center depends on the steric bulk of the incoming carbodiimide and of the four-coordinate Zr(NR<sub>2</sub>)<sub>4</sub> complex. Therefore, the five-coordinate compound Zr(SiMe<sub>3</sub>guanidinato)(NMe<sub>2</sub>)<sub>3</sub> (**14**) was synthesized in quantitative yield. Also in this case the five-coordinate compounds were found to be non-volatile. It is not easy to provide a simple explanation for this observation. One could think of higher dipolar interaction arising from the different electronic distribution between the three dialkylamido groups and the fourth guanidinato ligand, this speculation also being valid in the case of the five-coordinate  $\beta$ -diketiminato compounds.

The six-coordinate guanidinato-based compounds **12** and **13** are less volatile than the corresponding diketiminato-substituted **1** and **2**, the reason being probably due to the difference in molecular weight.

In principle **12** and **13** could be used as CVD precursors, although evaporation temperature as high as 150-153 °C would need to be used.

These findings make clear that there is no simple structure-volatility and structure-thermal stability correlation, and that there is a need for a deeper insight into the understanding of the intermolecular forces in these systems.

This work provides interesting hints as to which direction ligand tuning could take place to further improve the properties of the precursors, for example using trifluoromethyl substituted  $\beta$ -diketiminates, some of which are already described in the literature, and also commercially available, although very expensive. Finally, considering the latest development in the field of hard nanocomposite PVD coatings of the type TiN/Si<sub>3</sub>N<sub>4</sub> (a material that is also attractive in microelectronic applications), our silicon-containing guanidinato-based precursor could open a possible door to the development of single-source MOCVD for this kind of films.

The compound Zr(MeNacNac)<sub>2</sub>(NMe<sub>2</sub>)<sub>2</sub> (**1**), was tested in CVD experiments. It proved to be suitable as a MOCVD precursor. XPS spectroscopy reveals that the as-deposited films displayed a surface oxidation in accordance with what was observed in the literature for PVD coatings<sup>[1, 2]</sup>. Our films can be described as composed of a Zr(C,N) layer covered by an oxynitride/oxide layer. Incorporation of oxygen into the carbonitride film is also likely to occur during the deposition process, as was ascertained by XPS analysis after Ar<sup>+</sup> sputtering. The conditions corresponding to the lowest amount of oxygen are achieved when the growth rate is at the maximum value.

On the one hand, the presence of ZrO<sub>2</sub> in the bulk is probably detrimental to physical properties of the films, such as the hardness<sup>[3]</sup>. On the other hand, it has been reported that the surface oxide layer seems to improve the corrosion resistance of the film compared to TiN coatings, where the formation of a surface oxide has not



been observed <sup>[4, 5]</sup>. Oxygen incorporation into the film was found also for PACVD carbonitrides coatings obtained using  $Zr(NR_2)_4$  precursors, at atomic percent amounts ranging from 8 to 12 %.<sup>[6]</sup> Comparison with other literature results, such as the one from Täschner *et al.*<sup>[7]</sup>, is more difficult, since no XPS data are reported. As can be seen, even under the kinetic conditions typical of plasma-assisted processes, pure ZrN or Zr(C,N) are challenging to obtain. The work performed in our laboratories by Allenbach, using several four-coordinate compounds, yielded films with oxygen contents ranging from 7 to 49 % atomic percent, depending on the type of substituent on the precursor. <sup>[3]</sup>

Precursor **1** appears to be advantageous, as far as handling and storage are concerned, and provides a useful perspective on how to further tune these molecules.

## References

- [1] I. Milosev, H. H. Strehblow, M. Gaberscek, B. Navinsek, *Surf. Interface Anal.* **1996**, *24*, 448.
- [2] P. Prieto, L. Galan, J. M. Sanz, *Surf. Interface Anal.* **1994**, *21*, 395.
- [3] C. P. Allenbach, ETH Zürich, Laboratory for Surface Science and Technology (Zürich), **2000**.  
<http://e-collection.ethbib.ethz.ch/show?type=diss&nr=13832>
- [4] L. Vanleaven, M. N. Alias, R. Brown, *Surf. Coat. Technol.* **1992**, *53*, 25.
- [5] R. Brown, M. N. Alias, R. Fontana, *Surf. Coat. Technol.* **1993**, *62*, 467.
- [6] H. Berndt, A. Q. Zeng, H. R. Stock, P. Mayr, *Surf. Coat. Technol.* **1995**, *74-5*, 369.
- [7] C. Taschner, K. Bartsch, A. Leonhardt, *Surf. Coat. Technol.* **1993**, *61*, 158.

# CURRICULUM VITAE

## Personal

**Name:** Pier Luigi

**Surname:** Franceschini

**Place & date of birth:** Rome, on 25 November 1972

**Nationality:** Italian

**Residence:** Schürgstrasse 69 8051 Zürich

**Civil status:** single

**Phone:** +41 01-3213028 (home), +41 01-632 3572 (work), +41 76 349 2511 (mobile)

**E-mails:** pier-luigi.franceschini@ mat.ethz.ch or, ziprete72@hotmail.com

## Education

- 8/1999-date: PhD student/Assistant, Laboratory for Surface Science and Technology, ETH Zürich.
- 1992-2/1998: *Laurea* in Industrial Chemistry, University of Rome "La Sapienza". Final Grade 110/110. Thesis title: "*Synthesis and Characterization of Organometallic Polymers Containing Group 10 Elements, and related model molecules.*"
- Pre-university higher education: *Maturità* obtained at the institute "*Toscanelli*", Rome. Final grade 56/60.

## Work Experiences

- 8/1999-date: Laboratory for Surface Science and Technology, Swiss Federal Institute of Technology, Zürich. PhD project in collaboration with the University of Zürich, Department of Inorganic Chemistry.  
**Thesis title:** "*Design and Applications of New MOCVD Precursors for Nitrogen-Containing Zirconium-Based Thin Films*"  
**Tasks & achievements:** Development of volatile metal-organic zirconium compounds, characterization of chemical and physical properties, tests in CVD experiments and characterization of the films. I was also responsible for the Raman spectroscopy service at the University of Zürich and I assisted undergraduate students in the laboratory.
- 3/1999-7/1999: Full-time employment at Engelhard Italiana S.p.A, Rome, Catalyst Technology Division.  
**Tasks & achievements:** Development of custom-designed laboratory-scale heterogeneous catalysts containing precious metals. I was also involved in a project aimed at the development of a pilot-scale reactor for the production of a vinyl acetate catalyst.
- 9/1998-2/1999: Part-time employment at Engelhard Italiana S.p.A, Rome, Catalyst Technology Division.  
**Tasks & achievements:** See the entry above.
- 4/1998-1/1999: Fellowship at "*Centro Sviluppo Materiali S.p.A.*" Rome, in collaboration with the *University Roma III*.  
**Research Topic:** "*Thin polymeric Films on Metallic Surfaces*".  
**Tasks & achievements:** Studies on the composition and properties of films of epoxy resins on stainless-steel substrates, mainly using XPS and FT-IR (ATR) techniques.
- 96 & 97: Short Collaborations with volunteers association in France and Wales.

## Technical Skills

- Experience in the surface characterization of thin films. Experience in synthetic organic- and organometallic chemistry, including handling of air-sensitive compounds.
- Instrumental techniques: X-ray Photoelectron Spectroscopy (XPS), Atomic Force Microscopy (AFM); very little experience with SEM. FTIR and RAMAN, UV-vis, NMR, Gel Permeation Chromatography, X-ray diffraction (WAXD), Thermal analysis (DSC and TG).

## Languages

- **Italian.** Mother tongue
- **English.** Fluent
- **German:** Goethe Institute's "*Erste Zertifikat auf Deutsch*" exam passed with the highest grade.
- **French:** Fluent